MICRO-ELASTOHYDRODYNAMIC LUBRICATION IN CONCENTRATED SLIDING CONTACTS

Jan-Willem Sloetjes

Micro-elastohydrodynamic lubrication in concentrated sliding contacts

Jan-Willem Sloetjes

MICRO-ELASTOHYDRODYNAMIC LUBRICATION IN CONCENTRATED SLIDING CONTACTS

Jan-Willem Sloetjes

This research was supported by SKF Engineering & Research Centre, Nieuwegein, The Netherlands.

De promotiecommisie is als volgt samengesteld:

prof.dr. F. Eising, Universiteit Twente, voorzitter en secretaris
prof.dr.ir. D.J. Schipper, Universiteit Twente, promotor
prof.dr.ir. A. de Boer, Universiteit Twente
prof.dr. M.C. Elwenspoek, Universiteit Twente
prof.dr.ir. P.M. Lugt, Luleå University of Technology, Luleå, Sweden
prof.dr.ir. J.B. Jonker, Universiteit Twente
prof.dr. J.H. Tripp, Case Western Reserve University, Cleveland, USA

MICRO-ELASTOHYDRODYNAMIC LUBRICATION IN CONCENTRATED SLIDING CONTACTS
Sloetjes, Jan Willem
Ph.D. Thesis, University of Twente, Enschede, The Netherlands
November 2006

ISBN 90-365-2419-9

Keywords: roughness, micro-EHL, non-Newtonian lubricants, tribology

Printed by Wöhrmann Printing Service, Zutphen, The Netherlands

MICRO-ELASTOHYDRODYNAMIC LUBRICATION IN CONCENTRATED SLIDING CONTACTS

PROEFSCHRIFT

ter verkrijging van
de graad van doctor aan de Universiteit Twente,
op gezag van de rector magnificus,
prof. dr. W.H.M. Zijm,
volgens besluit van het College voor Promoties
in het openbaar te verdedigen
op 30 november 2006 om 13.15 uur

door

Jan Willem Sloetjes
geboren op 28 december 1972
te Winterswijk-Meddo

Dit proefschrift is goedgekeurd door de promotor:
prof. dr. ir. D.J. Schipper

Samenvatting

De laatste jaren bestaat er een trend om systemen steeds verder te verkleinen. Hierdoor worden de individuele componenten gedwongen om onder extremere condities te functioneren. Dit leidt tot dunnere smeerfilms tussen onderling bewegende componenten die in contact zijn, met als gevolg dat interactie tussen ruwheidstoppen een belangrijke rol gaat spelen. Dit vormde de aanleiding tot een intensivering van het onderzoek op het gebied dat zich bezig houdt met volle film smering op ruwheidsniveau. Dit onderzoeksgebied wordt aangeduid met de term micro-EHL. Vergeleken met grensgesmeerde contacten hebben contacten die volledig gesmeerd zijn op micro niveau als voordeel dat de wrijving daalt en dat de corrosieve en adhesieve slijtage verminderd wordt. Beide effecten hebben een positieve invloed op de levensduur. Het doel van dit proefschrift is om de mechanismen en parameters die een rol spelen bij de vorming van micro-EHL gesmeerde contacten en het effect hiervan op de wrijving verder in kaart te brengen.

De invloed van de ruwheid op gesmeerde contacten onder Newtonse vloeistofcondities en met een relatief gezien wat dikkere smeerfilm is een onderwerp dat vrij uitgebreid besproken is in de literaruur. Het blijkt dat de filmvorm voor een groot deel wordt bepaald door de zogenaamde inlet pressure sweep, die wordt gevormd in het gebied in de inlaat waar de druk wordt opgebouwd. Wanneer de hoogbelaste Hertze zone is bereikt, is door de exponentiële toename van de viscositeit de drukstroming gereduceerd tot een minimum. Hierdoor ligt de filmvorm vast en kan de micro-geometrie in deze zone daar geen invloed op uitoefenen. De invloed van de geometrie beperkt zich tot de variaties in de drukopbouw. Wanneer de filmdikte afneemt zodanig dat er contacten op ruwheidsniveau optreden, gaan andere effecten een rol spelen. Studies naar de invloed van niet-Newtons gedrag laten zien dat de drukstroming toeneemt. Deze wordt verder vergroot door de algehele daling van de hydrodynamische druk (en dus daling van de viscositeit) als gevolg van het dragend vermogen van de micro contacten. De toename van de drukstroming heeft tot gevolg dat de invloed van de micro geometrie op de lokale filmdikte in de hoogbelaste zone toeneemt. Met andere woorden, de lokale filmdikte wordt mede bepaald door de lokale ruwheid. Dit heeft geleid tot de huidige aanpak van het fenomeen micro-EHL, waarin een ruwheidstop als een individueel gesmeerd contact wordt beschouwd.

Om meer inzicht te krijgen in micro-EHL is een model ontwikkeld dat de filmdikte op ruwheidsniveau voorspelt als functie van de lokale condities. Het model is gebaseerd op de aannames zoals gemaakt door Ertel en is geldig voor een Newtonse vloeistof. Als eerste zijn ruwheidstoppen gegeven door een kromtestraal en een amplitude bekeken. Dit is onderverdeeld in een 2D geval (cylindrische geometrie) en een 3D geval (bolvormige

geometrie). De resultaten laten zien dat er een grote overeenkomst bestaat tussen de 2D en de 3D situatie. Afgezien van een constante zijn de vergelijkingen exact gelijk aan elkaar. Dit geeft aan dat dezelfde basisprincipes bepalend zijn voor de filmdikte. Verder blijkt dat de vloeistofparameters een belangrijkere rol spelen dan de lokale geometrie.

Als tweede zijn wigvormige en kegelvormige ruwheidstoppen beschouwd. Deze vormen worden gegeven door een helling en een amplitude. De globale trend is gelijk aan het geval waarbij de toppen gegeven zijn door een kromtestraal en een amplitude: de vloestofparameters zijn voor een belangrijk deel bepalend voor de lokale filmdikte, de lokale geometrie speelt een ondergeschikte rol. Alleen met betrekking tot de amplitude is een ander gedrag waar te nemen. Bij een vaste helling leidt een grotere amplitude tot een dikkere film.

Niet-Newtons gedrag is onderzocht aan de hand van een cylindrisch EHL model, waarbij uitgegaan is van een isoviskeuze vloeistof dat het Eyring gedrag vertoont. De resultaten laten zien dat de invloed van de vloeistofparameters afneemt, terwijl de micro geometrie een belangrijkere rol gaat spelen.

Het verband tussen wrijving en micro-EHL is bekeken door het micro-EHL model te integreren in een bestaand model dat de Stribeck curve voorspelt. Het blijkt dat globaal gezien micro-EHL leidt tot een verlaging van de wrijving in vergelijking met een grensgesmeerd contact. Wanneer de gehele belasting wordt gedragen door de ruwheidstoppen leidt een lagere snelheid tot een lagere wrijving. In de literatuur is dit gedrag ook experimenteel aangetoond. Verder toont een parameterstudie aan dat een verhoging van de inlaatviscositeit of een verlaging van de druk-viscosteits index, de Eyring constante of de amplitude van de ruwheid een verdere verlaging van de wrijving tot gevolg heeft.

In het geval dat de volledige belasting wordt overgedragen door de ruwheden, blijkt dat het model ter plekke van de toppen een filmdikte voorspelt die ligt in de orde van een fractie van een nanometer. Dit vormt één van de begrenzingen van micro-EHL, namelijk de vraag of het daadwerkelijk mogelijk is om een olielaag te vormen van deze afmetingen onder deze extreme condities.

Abstract

Due to the trend of down-sizing, machine elements are forced to operate under increasingly severe conditions. For lubricated systems this means that the lubricating films reduce to a level such that asperity interaction starts to play a role. For this reason, the full film lubrication of concentrated contacts on asperity level gained more attention. This field of research is generally denoted as micro-EHL. Compared to boundary lubricated micro contacts, fully lubricated asperity contacts result into a reduced coefficient of friction and a reduction of the corrosive and adhesive wear. This will have a positive effect on the life of the contacting surfaces. The purpose of this thesis is to determine the mechanisms involved in micro-EHL and in which way the parameters affect the film formation and friction.

The effect of surface roughness under Newtonian conditions at relatively thick films is studied extensively over the years. The literature review shows that under these conditions the film thickness is determined mainly by the inlet pressure sweep, which is generated in the region in the inlet where the pressure build up takes place. Once the Hertzian contact zone is entered, the viscosity increases very fast to values such that pressure induced flow is reduced to a minimum. As a result, the film thickness is not affected by the micro geometry, its influence is limited to the pressure distribution. When the conditions become more severe, i.e. increased asperity contact, the situation changes. Studies involving non-Newtonian behaviour indicate that the reduction in effective viscosity enables pressure driven flow. This is enhanced by the overall reduction in hydrodynamic pressure (and with that the viscosity), caused by the load transfer at the asperity contacts. As a result, the influence of the micro geometry on the local film thickness inside the Hertzian zone increases. In other words, the film thickness is determined for a large part by the local conditions. This has led to the present approach of modelling micro-EHL, in which the asperity contact is considered as a single concentrated contact on microscopic scale.

For a better understanding of the micro-EHL concept, a model is developed to predict the film thickness on asperity level as a function of the local conditions. It is based on the assumptions as made by Ertel and is valid for a Newtonian lubricant. First asperities given by an amplitude and a radius of curvature are considered. This analysis is divided into a 2D case (cylindrical shaped asperity) and a 3D case (spherical shaped asperity). The results of the 2D and 3D situation show large similarities. Apart from a constant, the film thickness formulas are exactly the same, indicating that the same underlying phenomena determine the film thickness. Further, it is shown that the lubricant parameters

have a larger influence on the film thickness than the local geometry.

Secondly, asperities characterized by a slope and an amplitude are analyzed, i.e. a wedge shaped and a conical shaped asperity. The global trend is the same as in the case of an asperity given by a radius of curvature and amplitude: the main parameters influencing the local film thickness are lubricant related. Regarding the amplitude of an asperity a different behaviour is found. Here a larger amplitude leads to a thicker film.

Non-Newtonian effects are studied by means of modelling the cylindrical EHL contact for an Eyring lubricant under isoviscous conditions. The results show that the influence of the lubricant parameters is reduced, whereas the geometry becomes more important.

An existing model to predict the Stribeck curve in which the micro-EHL model is incorporated is used to examine the relation between micro-EHL and friction. In general, it is observed that in case the conditions are such that micro-EHL occurs, the friction decreases, compared to a boundary lubricated contact. Under conditions of full asperity contact it is found that the friction decreases with decreasing velocity. This behaviour was also experimentally observed. Further, a parameter study reveals that an increase in inlet viscosity or a decrease in pressure viscosity index, Eyring constant or roughness amplitude, gives rise to a further decrease in friction.

At full asperity contact it is found that the predicted film at a micro contact can drop to a fraction of a nanometer. This forms one of the limits of micro-EHL, namely the question whether it is possible to create such a thin lubricant layer at these extreme conditions or not.

Contents

Nomenclature

Roman symbols

a	Hertzian half contact length	[m]
$a_{l,s,w,n}$	Hertzian half contact length for cy**l**indrical, **s**pherical, **w**edge or co**n**ical shaped asperity	[m]
A	constant	
A	amplitude	[m]
$\mathcal{A}$	penetration amplitude, $A - h_{sm}$	[m]
b	lubricant parameter, see eq. (3.59)	–
B	constant	
C	constant	
d	sampling interval	[m]
D	Deborah number, $\dfrac{\eta_m u_m}{2aG_m}$	–
E	modulus of elasticity	[Pa]
E'	reduced modulus of elasticity, e.g. $\dfrac{2}{E'} = \dfrac{1-\nu_1^2}{E_1} + \dfrac{1-\nu_2^2}{E_2}$	[Pa]
F	load	[N]
G	shear modulus	[Pa]
G_0	shear modulus at ambient pressure	[Pa]
h	film thickness	[m]
$h_{l,s,w,n}$	Hertzian gap geometry outside the loaded zone for cy**l**indrical, **s**pherical, **w**edge or co**n**ical shaped asperity	[m]
h_0	central film thickness	[m]
h_H	Hertzian deformation at the centre of the contact	[m]
h_{sm}	surrounding film thickness	[m]
H	operational number $H = \dfrac{\eta u_s}{p_m}$	[m]
$\mathcal{L}$	dimensionless number, see eq. (3.25)	–
L	life	[revs]
L	Moes dimensionless lubricant parameter, line contact $L = \alpha E' \left(\dfrac{\eta_0 u_s}{E'R'}\right)^{1/4}$; circular contact $L = \alpha E' \left(\dfrac{\eta_0 u_s}{E'R'_x}\right)^{1/4}$	–

M	Moes dimensionless load parameter, line contact $M = \frac{w}{E'R'}\left(\frac{\eta_0 u_s}{E'R'}\right)^{-1/2}$, circular contact $M = \frac{F}{E'R'^2_x}\left(\frac{\eta_0 u_s}{E'R'_x}\right)^{-3/4}$	–
n	rheological index	–
n	asperity density in the asperity contact model of Greenwood and Williamson [50]	$[\mathrm{m}^{-2}]$
$\mathcal{N}$	dimensionless number, see eq. (4.32)	–
p	pressure	[Pa]
p_0	surrounding pressure	[Pa]
p_c	Roelands reference pressure	$1.98 \cdot 10^8$ Pa
p_g	glass transtion pressure	[Pa]
p_H	maximum Hertzian pressure	[Pa]
p_m	mean pressure	[Pa]
p_x	derivative of the pressure in x-direction, $p_x = dp/dx$	$[\mathrm{Pa\,m}^{-1}]$
$\mathcal{P}$	ratio between pressure flow induced shear stress and non-Newtonian offset, see eq. (5.10)	–
P	Greenwood load parameter, $\mathrm{P} = \alpha p_H$	–
q	coefficient relating the Hertzian contact width and the pressure	–
q	isoviscous pressure	[Pa]
r	radial coordinate	[m]
R	radius of curvature	[m]
R'	reduced radius of curvature or gap curvature, e.g. $\frac{1}{R'} = \frac{1}{R_1} + \frac{1}{R_2}$	[m]
R_a	centre line average roughness	[m]
R_q	root mean square roughness	[m]
$s_{w,n}$	slope of a **w**edge shaped or co**n**ical shaped asperity	–
$\mathcal{S}$	dimensionless number, see eq. (3.103) and eq. (3.108)	–
S	Greenwood speed parameter, $\mathrm{S} = L$	–
S_0	Roelands temparature viscosity index	–
S	slip or slide-to-roll ratio, $S = u_d/u_m$	–
t	time	[s]
T	temperature	[°C]
T_0	reference temperature	[°C]
T_g	glass transition temperature	[°C]
u	surface velocity	$[\mathrm{m\,s}^{-1}]$
u_{asp}	velocity of surface with asperity	$[\mathrm{m\,s}^{-1}]$
u_d	sliding velocity, $u_d = u_1 - u_2$ ('smooth surface' - 'rough surface')	$[\mathrm{m\,s}^{-1}]$
u_m	mean surface velocity, $u_d = \frac{1}{2}(u_1 + u_2)$	$[\mathrm{m\,s}^{-1}]$
u_r	radial surface velocity	$[\mathrm{m\,s}^{-1}]$
u_s	sum surface velocity, $u_s = u_1 + u_2$	$[\mathrm{m\,s}^{-1}]$
$\mathcal{U}$	ratio between shear flow induced shear stress and non-Newtonian offset, see eq. (5.10)	–
v	elastic deformation	[m]
w	load per unit of length	$[\mathrm{N\,m}^{-1}]$

$\mathcal{W}$	dimensionless number, see eq. (4.12)	–
x	spacial coordinate	[m]
y	spacial coordinate	[m]
z	spacial coordinate	[m]
z	height	[m]
z	dummy variable	–
z	Roelands pressure viscosity index	[m]

Greek symbols

α	Barus pressure viscosity index	[Pa^{-1}]
α_g	pressure viscosity index in the glassy state	[Pa^{-1}]
α^*	Blok [17] pressure viscosity index, see eq. (3.53)	[Pa^{-1}]
β	average radius of curvature in the asperity contact model of Greenwood and Williamson [50]	[m]
$\beta_{l,s}$	radius of curvature for a **cyl**indrical or **s**pherical shaped asperity	[m]
$\dot{\gamma}$	shear rate	[s^{-1}]
ζ	pressure limiting shear stress coefficient	–
η	dynamic viscosity	[Pa s]
η_0	dynamic viscosity at ambient pressure and reference temperature	[Pa s]
η_e	effective viscosity	[Pa s]
η_∞	Roelands reference dynamic viscosity	$6.315 \cdot 10^{-5}$ Pa s
η_g	dynamic viscosity at glass transition	[Pa s]
θ	slope angle of a wedge shaped or conical shaped asperity, $s = \tan\theta$	–
Θ	dimensionless number, see eq. (5.21)	–
ϑ	pressure shear modulus coefficient	–
λ	wavelength of roughness	[m]
λ	ratio film thicknes over roughness	–
λ	dimensionless number, see eq. (5.21)	–
μ	coefficient of friction	–
μ_{BL}	coefficient of friction in the BL regime	–
μ_{τ_L}	coefficient of friction in case the lubricant behaves as a solid	–
μ_{asp}	coefficient of friction at the asperities	–
ν	Poisson ratio	–
ξ	temperature Eyring stress coefficient	–
ρ	density	[$\mathrm{kg\,m}^{-3}$]
ρ	curvature	[m^{-1}]
σ	lubricant parameter, see eq. (3.55)	–
σ^*	root mean square asperity summit distribution in the asperity contact model of Greenwood and Williamson [50]	[m]
τ	shear stress	[Pa]
$\dot{\tau}$	time derivative of the shear stress	[$\mathrm{Pa\,s}^{-1}$]
τ_0	Eyring stress	[Pa]
$\tau_{0,0}$	Eyring stress at reference temperature	[Pa]

τ_L	limiting shear stress	[Pa]
$\tau_{L,0}$	limiting shear stress at ambient pressure	[Pa]
τ_m	mean limiting shear stress	[Pa]
τ_{pr}	fatigue stress criterion	[Pa]
ϕ	angular coodinate	[rad]
Φ	mass flow per unit of length	$[\mathrm{kg\,m^{-1}s^{-1}}]$
ω	angular velocity	$[\mathrm{rad\,s^{-1}}]$

Abbrevations

BL	Boundary Lubrication
EHL	ElastoHydrodynamic Lubrication
ML	Mixed Lubrication
HL	Hydrodynamic Lubrication
ML	Stribeck curve prediction based on boundary lubricated asperity contacts.
mEHL	Stribeck curve prediction based on micro-EHL lubricated asperity contacts.
RI	rigid isoviscous
RP	rigid piezoviscous
EI	elastic isoviscous
EP	elastic piezoviscous

Subscripts

$1,2$	body 1,2 or sequence number
x	x-direction
y	y-direction
st	start point of pressure build up due to asperity deformation, in the starved approach, see section 3.2.7
i,j	gridpoint i,j

Accents

$\hat{}$	scaling parameter
$\bar{}$	dimensionless variable
$\tilde{}$	dimensionless variable

Chapter 1

Introduction

Tribological phenomena like friction and wear have a large influence on everyday life. Although wear is generally considered as unfavourable, in many cases it is essential. Take for instance writing with a pencil. One would see hardly anything if the graphite did not wear off. The same goes for friction. Many cases can be found in which friction should be as low as possible, for example the contact between ice and a speed skate, an important issue in The Netherlands. But one can think of just as many applications which demand for a high level of friction, for instance everything which is related to braking. In general it can be said that for each situation there is an optimized level of friction and wear. In many industrial applications this comes down to minimizing both friction and wear.

One of the fields in which a minimum of friction and wear plays an important role is the rolling bearing industry. Both friction and wear levels should be as low as possible to keep the energy loss limited and to last a sufficient large lifetime. The usual way of creating a low friction and wear is to lubricate the rolling elements of the bearing, i.e. create a small film of lubricant between the rolling elements and the inner and outer ring. To prevent (adhesive) wear this film should be sufficiently large to fully separate the surfaces from the rolling element and the ring. At the same time the low shear stress of the lubricant film gives the desired low friction. By means of producing very smooth surfaces the lubricant film easily reaches a level sufficient to achieve full separation.

In the last decade down-sizing became an important issue in industry. As a consequence, the conditions under which bearings must operate became increasingly severe, i.e. the lubricant films were getting smaller and smaller. Eventually even the very smooth surfaces will be too rough, resulting into too much metal-to-metal contact and accompanying high levels of wear and friction. This has led to a different view towards surface topography. Instead of producing smoother surfaces to prevent metal-to-metal contact, the development is shifting in the direction of “sophisticated” surface topographies which enhance the film build up. This means that, next to the global shape of the contact, the shape on asperity level becomes important.

1.1 Lubrication

Bearing life, or the life of the contacting surfaces, is the most important parameter which determines the performance of a bearing. For a good understanding of the prediction and optimization of surface life, three states of operating conditions must be considered: full film lubrication, mixed lubrication and boundary lubrication. If the surfaces are fully separated by a lubricant film and no asperity interaction takes place, surface life is solely governed by fatigue (sub-surface stresses). This state is denoted as full film lubrication or Hydrodynamic Lubrication (HL). When the operational conditions become more severe or surface roughness increases, the amount of asperity interaction increases too and the lubricated contact enters the Mixed Lubrication regime (ML). Then surface life is no longer controlled by fatigue only, but also by the boundary films between the asperities (corrosive wear) and the occurrence of metallic contact (adhesive wear). The latter two phenomena will lead to an increased level of wear. Finally, when the film becomes that small that the load is completely carried by the micro contacts, surface life is determined by asperity interaction only. This is called Boundary Lubrication (BL). Generally, this state is not desirable during operation of bearings because of the high level of friction and wear. However, it is inevitable at the very beginning of the running-in period and at start-up or stop-down of a bearing. The three main states of lubrication are illustrated schematically in Figure 1.1.

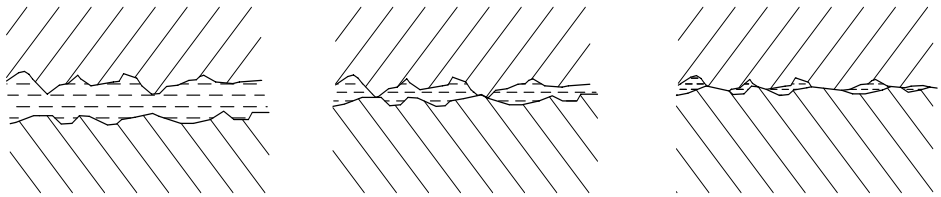

Figure 1.1: Lubrication modes

The generalized friction behaviour of each of the lubrication modes is shown in Figure 1.2. This curve is denoted as the generalized Stribeck curve [93], where μ is the coefficient of friction and H is defined as $\eta u_s / p_m$, in which η is the lubricant dynamic viscosity, u_s is the sum velocity of the contacting surfaces and p_m is the mean contact pressure. This curve is essentially a Stribeck curve as introduced by Stribeck [97] with, instead of the speed, the parameter H on the x-axis. This parameter H is built up very similar to the well-known Hersey number $\eta n / p_{\text{proj}}$ [57], where n is the number of revolutions and p_{proj} is the load per unit projected area. In fact H is strongly related to the film thickness.

In bearings, particularly the contact between the inner ring and the rolling element, the pressure easily reaches values in the order of 2 GPa or higher. This has a large effect

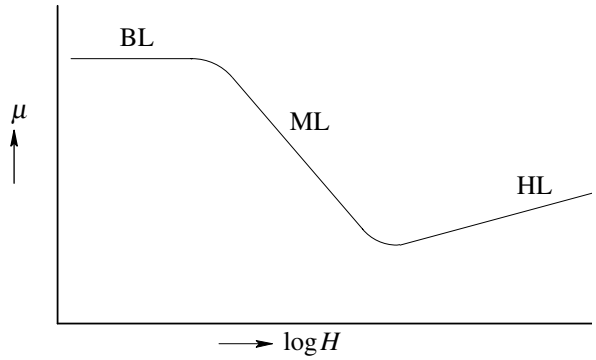

Figure 1.2: Generalized Stribeck curve

on the lubrication capabilities. Firstly, at these pressures the surfaces can no longer be considered as rigid. In general the deformation of the surfaces is many times larger than the film thickness, and therefore it can not be neglected. This lubrication mode is generally denoted as *elasto*hydrodynamic lubrication (EHL). Secondly, the lubricant viscosity changes dramatically. In section 2.2 the consequences of this behaviour will be discussed in more detail.

1.2 Surface life and micro-EHL

With respect to surface life it is clear that metallic contact and boundary lubricated asperity contacts should be avoided. One way to achieve this, is by means of producing a surface which promotes the occurrence of micro-EHL, or in other words the presence of

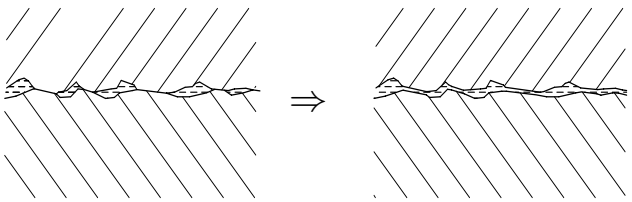

Figure 1.3: From asperity contact to micro-EHL

a (small) lubricant film between interacting asperities, as illustrated in Figure 1.3. If such a (small) film is present, the adhesive and corrosive wear will be highly reduced. This will lead to an increased surface life of a rough surface.

Micro-EHL has not only an effect on surface life, but also on other bearing design criteria such as lift-off, running-in and friction:

- Micro-EHL leads to asperity separation, thereby decreasing the lift-off velocity. Note that this is true if lift-off is defined as zero electrical conductivity between the two surfaces. Micro-EHL does not affect the transition from full film lubrication to mixed lubrication.

- Due to the reduction of adhesive and corrosive wear, running-in will be reduced.

- In micro-EHL the traction due to asperity interaction is controlled by shear in the liquid or solidified film, which leads to a lower coefficient of friction compared to the normal boundary lubricated asperities. Far into the mixed regime, i.e. when the normal force is almost fully carried by the asperities, this reduction in friction can be considerable. A reduction from 0.12 to 0.09 (25%) in friction coefficient in the BL regime is very common [93]. This will have a positive effect on the life of the bearing. However, quantification of this effect is not straightforward. It is generally assumed that for the fatigue life $L \propto 1/\tau_{pr}^9$, where L is the fatigue life and τ_{pr} is the fatigue stress criterion. How the fatigue stress criterion is affected by the friction at the surface is still a subject of investigation. It largely depend on the choice of τ_{pr}, Ioannides et al. [65]. For instance, based on the work of Bayer and Ku [16], which state that $\tau_{pr} \propto \sqrt{0.25+\mu^2}$, the reduction in friction can lead to an increase in fatigue life of 10%. On the other hand, Harris and Yu [56] show that a surface shear stress has almost no effect on the life if it is calculated according to the well-known model by Lundberg and Palmgren [82]. However, it is widely accepted that reduction of the surface shear stress leads to a longer life.

Summarizing, it can be concluded that micro-EHL can be of great importance for the functioning of a rough surface operating in the BL and ML regime. This not only regarding as the primary point of interest the surface life, but also with respect to the performance of rough surfaces in general.

1.3 Micro-EHL parameters

In order to produce a surface promoting micro-EHL, the parameters which influence this phenomenon must be known. Therefore, a closer look is given at the effect of micro-EHL on the extended generalized Stribeck curve. This extended curve is illustrated schematically in Figure 1.4. Apart from the three regimes as described above and depicted by the upper curve, in the ML and BL regime two main curves are added:

- The lower curve indicates the occurrence of micro-EHL at the interacting asperities. Since the shear stress in an asperity contact operating under micro-EHL conditions is less than the shear stress in boundary lubricated micro contacts, the coefficient of friction increases at a smaller rate with decreasing H. In case the load is fully carried by the asperities and the lubricant behaves like a liquid, the coefficient of friction can even decrease with decreasing H.

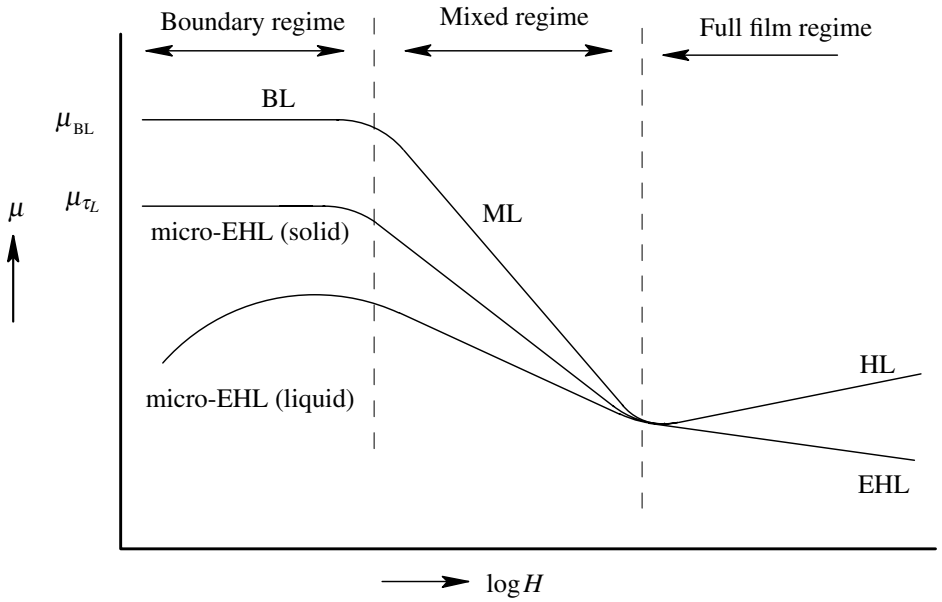

Figure 1.4: Extended generalized Stribeck curve, after results presented by [93, 94].

- The most frequently observed curve is the one indicated by μ_{τ_L}. If the load is completely carried by the asperities, it can be seen that the coefficient of friction does not depend on the H, similar to the curve indicated in Figure 1.4 by the BL regime. This can be explained as follows. Similar to EHL conditions, usually very high pressures are present in the micro contacts. As a result, the lubricant may act as a solid. If this is the case, the shear stress does no longer depend on the shear rate and is equal to the limiting shear stress, indicated by τ_L. As a result, the coefficient of friction will be constant.
  The solid-like behaviour, or the limiting shear stress behaviour, is also responsible for the higher slope of the coefficient of friction in the ML regime. Since the limiting shear stress is higher than the shear stress related to liquid behaviour, the contribution of the micro contacts to the friction will be relatively larger.

In practise the distinction made between solid and liquid micro-EHL is not that sharp. Often the system switches from one curve to the other by means of small changes in the lubricating conditions [93, 94]. For the same reason, a contact can switch from micro-EHL to boundary lubricated asperity contacts, which is obviously less desirable.

From the Stribeck curve it can be concluded that two aspects from a lubricated system determine the occurrence of micro-EHL:

- lubricant parameters
- asperity dimensions, i.e. micro geometry

Another way to look at the micro-EHL parameters and their influence is illustrated schematically in Figure 1.5. Micro-EHL can be promoted by choosing the right com-

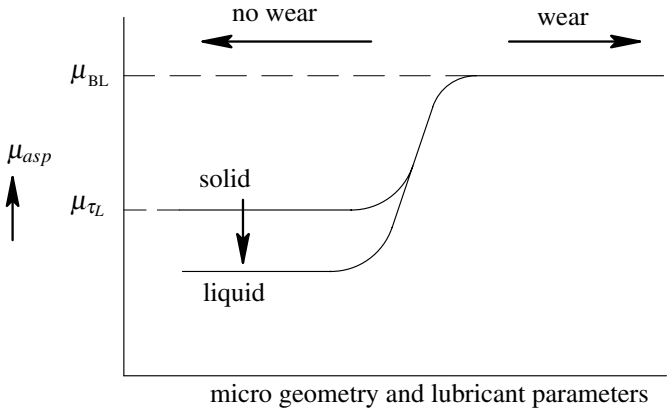

Figure 1.5: Schematic illustration of the relation between coefficient of friction and micro geometry/lubricant parameters in asperity contacts.

bination of micro geometry and lubricant. If micro-EHL is realized, i.e. the left hand side of the curve, adhesive and corrosive wear can be neglected. Fine tuning of the parameters can lead to lower friction due to the switch from solid to liquid behaviour of the lubricant.

1.4 Objective of this work

From the previous sections it is clear that micro-EHL can be of great importance for the functioning of bearing surfaces in general. To study this type of local lubrication in more detail, a new approach to the description of the asperity interaction under micro-EHL conditions will be presented. One of the goals is to avoid cumbersome numerical analysis in order to provide a tool which can be applied directly in an engineering environment. In the end the following fundamental question should be answered:

- **What are the characteristics of a surface topography and lubricant which promote the occurrence of micro-EHL?**

To answer this question, first of all a closer look at the existing work will be given. Here the focus will be on the two main parameters influencing micro-EHL. The review will be followed by the presentation of the model developed. Comparison with numerical work will be given as well. The next chapter will discuss an extension of the model with respect to the geometry of the asperity. A first step towards the inclusion of non-linear lubricant behaviour will be made in chapter 5, whereas chapter 6 deals with the effect of micro-EHL on the Stribeck curve. Finally, in chapter 7 the conclusions and recommendations for further work will be given.

Chapter 2

Background

The review on existing work concerning micro-EHL involves micro geometry and lubricant behaviour, from a theoretical as well as from an experimental point of view. First the lubricant properties will be discussed, followed by a brief introduction to film thickness calculation in general. This is done with respect to the discussion of the micro geometry, in which many concepts of the macroscopic behaviour are used.

2.1 Lubricant rheology

Rheology is a very important subject with respect to lubricated concentrated contacts. The properties of the lubricant are the main factors which determine the film thickness and the friction. The general behaviour of a lubricant can be represented by plotting the shear stress against the shear rate, as shown in Figure 2.1. The parameter D is called the Deborah number and is used to distinguish between elastic and viscous behaviour in a lubricated concentrated contact. It is defined as:

$$D = \frac{\eta_m u_m}{2aG_m} \tag{2.1}$$

where η_m is the average viscosity, G_m is the average shear modulus, a is the half contact width in running direction and u_m is the mean surface velocity. It can be seen as the ratio between the relaxation time of the lubricant, η_m/G_m, and the time that the fluid needs to pass through the contact, $2a/u_m$. For $D \ll 1$ viscous behaviour prevails and for $D \gg 1$ elastic behaviour is dominant.

Initially, in the viscous region the shear stress increases linearly with increasing shear rate. This behaviour is denoted as Newtonian behaviour. The limit of this behaviour is indicated by τ_0. Above this stress level the stress increases less than proportionally with the shear rate, which is called non-Newtonian behaviour.

Like all materials, lubricants have an ultimate strength, indicated in Figure 2.1 by the limiting shear stress τ_L. At this level of shear stress, the lubricant behaves in a plastic way, the stress is no longer depending on the shear rate.

If the shear rate reaches a very high level, thermal effects become significant. In this

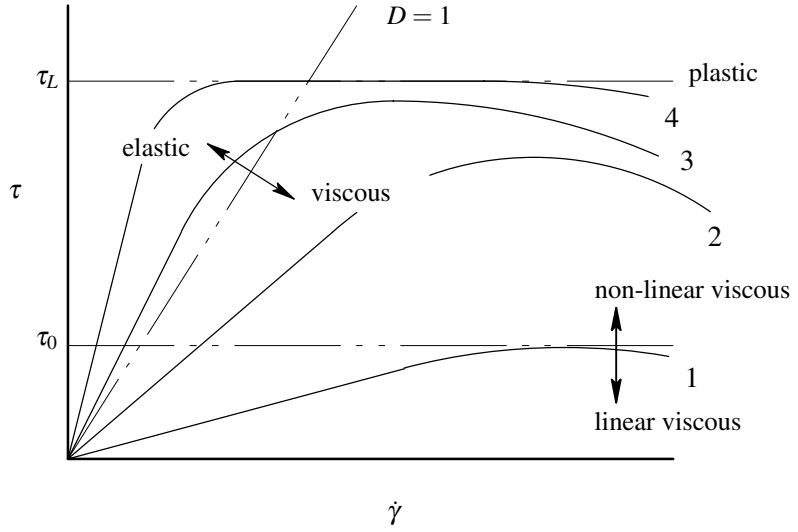

Figure 2.1: Shear stress versus shear rate, schematically. Reproduced from [36].

1 : linear viscous or Newtonian behaviour
2 : non-linear viscous or Eyring behaviour
3 : elastic - non-linear viscous behaviour
4 : elastic - plastic behaviour

region the shear stress generally decreases with the shear rate, as indicated towards the end of the four curves.

2.1.1 Shear models

In the past, several (successful) attempts were made to model the shear behaviour of a lubricant, all based on a non-linear Maxwell model. These models can be divided roughly into two groups. First, the models in which the viscous part is based on non-Newtonian Eyring behaviour, as proposed by Johnson and Tevaarwerk [72]:

$$\dot{\gamma} = \frac{\dot{\tau}}{G} + \frac{\tau_0}{\eta} \sinh\left(\frac{\tau}{\tau_0}\right) \tag{2.2}$$

This model contains three parameters: the limit of Newtonian behaviour τ_0, the shear modulus G and the viscosity at low shear rate η. The advantage of the Eyring model is that it has a physical meaning based on the thermal activation theory of viscous flow [37]. On the other hand, the main drawback is that it is not able to simulate limiting shear stress in a continuous way. In other words, to simulate Eyring and limiting shear stress behaviour two equations are needed. Johnson and Tevaarwerk [72] proposed to replace the part representing the viscous behaviour by the Prandtl-Reuss equation whenever the

limiting shear stress is reached. This way of incorporating limiting shear stress behaviour is followed by Evans and Johnson [35, 36].

The second group of models are based on limiting shear stress behaviour and are to a certain extent similar to the model as proposed by Bair and Winer in [6]:

$$\dot{\gamma} = \frac{\dot{\tau}}{G} - \frac{\tau_L}{\eta} \ln\left(1 - \frac{\tau}{\tau_L}\right) \tag{2.3}$$

This model does not distinguish between Newtonian and non-Newtonian behaviour in a way as the Eyring model does, but the transition is more or less included in the model by choosing a proper fit to data which are obtained experimentally. The advantage of this model is that the limiting shear stress is incorporated in an elegant way.

A more general model for the second term in eq. (2.3) was introduced by Elsharkawy and Hamrock [32]:

$$\dot{\gamma} = \frac{\tau}{\eta}\left[1 - \left(\frac{\tau}{\tau_L}\right)^n\right]^{-1/n} \tag{2.4}$$

By varying n, Elsharkawy and Hamrock are able to simulate various other models, such as the linear model of Iivonen and Hamrock [64] ($n = 1$), the *ln*-model of Bair and Winer [6] ($n \approx 1.8$), the circular model of Lee and Hamrock [78] ($n = 2$), the $\tanh^{-1}$-model of Gecim and Winer [44] ($n \approx 2.8$) and a viscous-plastic model ($n > 10$). All models are summarized schematically in Figure 2.2.

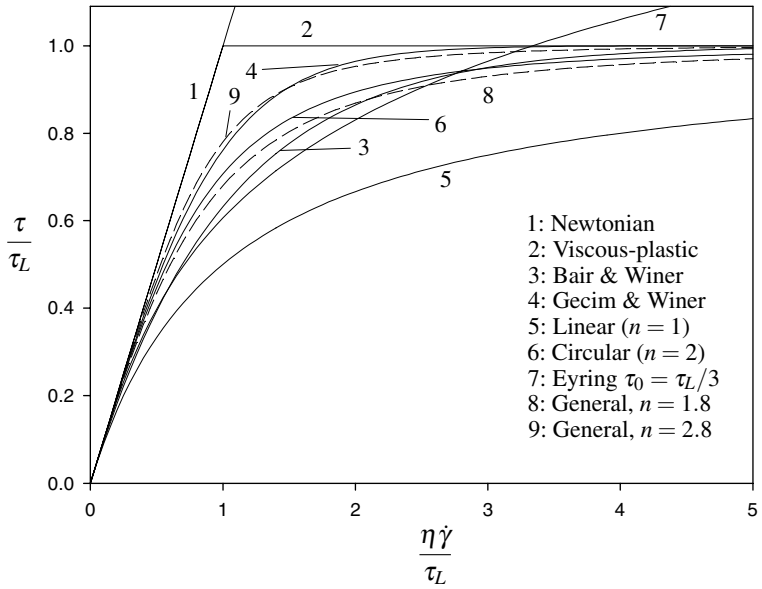

Figure 2.2: Non-Newtonian shear models. Reproduced from [32].

2.1.2 Lubricant parameters

The parameters used in the shear models are studied extensively. From the majority of the work follows that basically the parameters can be described best as linear functions of either the pressure or the temperature. The constants in the models obviously depend on the type of lubricant, but they may also depend slightly on pressure or temperature.

Estimation of the value of the parameters in the rheology models is done mostly by means of experiments. The parameter itself is determinant which method is the most suitable. For measuring the limiting shear stress, both static experiments like translating or rotating concentric cylinder devices and high shear viscometers [6, 8, 10, 12] and two disc experiments can be used [36]. Both methods show good agreement and lead to the following expression.

$$\tau_L = \tau_{L,0} + \zeta p \tag{2.5}$$

Two disc experiments are also very suitable for the determination of the limit of Newtonian behaviour. The most extensive study is performed by Evans and Johnson [36]. In contrary to τ_L, it appeared that τ_0 is depending mainly on the temperature:

$$\tau_0 = \tau_{0,0} + \xi T \tag{2.6}$$

For measuring the shear modulus, two disc experiments can not be used. Both Johnson and Tevaarwerk [72] and Evans and Johnson [36] conclude that the elastic response of the lubricants is overwhelmed by the elastic compliance of the discs. Oscillating shear methods [13], Barlow et al. [14] and shear cell experiments [6, 7, 9] are more appropriate. Generally the shear modulus is found to be proportional to the pressure with a small offset at the origin:

$$G = G_0 + \vartheta p \tag{2.7}$$

Tabor [98] proposed the following approximation for G:

$$G \approx 30\tau_L \tag{2.8}$$

The low shear rate viscosity is likely to be the parameter investigated most. Various models to describe the dependence of this parameter on pressure and temperature have been proposed. Probably the best-known model is the one published by Barus in 1893 [15]:

$$\eta(p) = \eta_0 \mathrm{e}^{\alpha p} \tag{2.9}$$

where η_0 is the dynamic viscosity at ambient pressure and reference temperature and α is the pressure viscosity index.

Temperature effects are incorporated by means of the temperature dependence of η_0. Due to its simplicity it is widely used, particularly in analytical analysis. However, at elevated pressures the viscosity can be overestimated. An alternative is the Roelands relation [92]:

$$\eta = \eta_0 \exp\left\{ \ln\left(\frac{\eta_0}{\eta_\infty}\right) \left[\left(\frac{135+T_0}{135+T}\right)^{S_0} \left(1+\frac{p}{p_c}\right)^{z} - 1 \right] \right\} \tag{2.10}$$

with z pressure viscosity index, typically $0.5 \leq z \leq 0.7$ for mineral oils
S_0 temperature viscosity index
η_0 dynamic viscosity at T_0 (T_0 in °C)
η_∞ a constant, $6.315 \cdot 10^{-5}$ Pa s
p_c a constant, 198 MPa

In this equation both the pressure and temperature effects are described more accurately. For this reason it is used extensively in various (mainly numerical) studies of EHL contacts. However, under more severe conditions ($p > 1$ GPa), Roelands can fail as well. Yasutomi et al. [113] proposed a model which gives improved results at these conditions. It is based on the free volume theory and reads:

$$\eta(T,p) = \eta_g \exp\left\{-2.3\frac{C_1(T-T_g(p))F(p)}{C_2+(T-T_g(p))F(p)}\right\} \tag{2.11}$$

where:

$$T_g(p) = T_g(0) + A_1 \ln(1+A_2 p) \tag{2.12}$$
$$F(p) = 1 - B_1 \ln(1+B_2 p) \tag{2.13}$$

In the latter two expressions T_g is the glass transition temperature and η_g the viscosity at the glass transition. The constants A_1 to C_2 depend upon the lubricant. Based on additional experimental observations, Bair and Winer [10] proposed a slight modification to this model to allow for the different behaviour of the lubricant above the glass transition pressure:

$$\begin{aligned}\eta(T,p) &= \eta_g \exp\left\{-2.3\frac{C_1(T-T_g(p))F(p)}{C_2+(T-T_g(p))F(p)}\right\}, \; p \leq p_g \\ \eta(T,p) &= \eta_g \exp\left\{\alpha_g(p-p_g)\right\} \qquad\qquad , \; p > p_g\end{aligned} \tag{2.14}$$

where p_g and α_g are the glass transition pressure and the viscosity-pressure coefficient in the glassy state respectively.

Comparison between the Yasutomi model and the Roelands model give varying results. For instance, for the mineral oil LVI 260 Roelands starts to deviate already at 0.5 GPa, see [12], whereas for the naphthenic mineral oil 36G [5] Roelands performs surprisingly well up to 1 GPa and in a temperature range of 0 to 218 °C [11].

2.2 Film thickness calculation in general

When designing bearings, generally the design is focussed on the most important parameter, the separation of the surfaces. In case of hydrodynamic lubrication, the lubricant flow between the surfaces is governed by the Reynolds equation [91]. This equation describes the conservation of mass for a fluid with negligible inertia and no flow across the fluid film (narrow gap assumption). Eq. (2.15) shows the general formulation:

$$\frac{\partial}{\partial x}\left(\frac{\rho h^3}{\eta}\frac{\partial p}{\partial x}\right)+\frac{\partial}{\partial y}\left(\frac{\rho h^3}{\eta}\frac{\partial p}{\partial y}\right)=12u_m\frac{\partial(\rho h)}{\partial x}+12\rho h\frac{\partial u_m}{\partial x}+12\frac{\partial(\rho h)}{\partial t} \tag{2.15}$$

where x spacial coordinate in the direction of motion of the surfaces
y spacial coordinate perpendicular to the direction of motion of the surfaces
ρ density of the lubricant
h lubricant film thickness
η dynamic viscosity of the lubricant
p hydrodynamic pressure across the film thickness
u_m average surface velocity in the direction of motion
t time

For steady state line contact with constant surface velocity and incompressible lubricant eq. (2.15) reduces to:

$$\underbrace{\frac{d}{dx}\left(\frac{h^3}{\eta}\frac{dp}{dx}\right)}_{\text{pressure}} = \underbrace{12u_m\frac{dh}{dx}}_{\text{shear}} \tag{2.16}$$

In this form it consists of only two components: a pressure induced flow component and a shear driven flow component (Poiseuille flow and Couette flow respectively).

As mentioned in section 1.1, in case of EHL the pressures become very high, resulting into relatively large elastic deformation of the surfaces and an enormous increase of the lubricant viscosity. At pressures larger than 0.5 GPa the viscosity can increase to values such that the lubricant behaves almost like a solid. As a consequence, the pressure induced flow decreases to a minimum. The Reynolds equation then reduces to:

$$0 \approx u_m\frac{dh}{dx} \tag{2.17}$$

It is easy to see that the film thickness must be almost constant along the high pressure region.

2.2.1 Solution of the Reynolds equation

Solution of the Reynolds equation under EHL conditions started with the Ertel solution [33], published by Grubin in 1949 [51]. The theory is based on two assumptions which follow from the the two characteristic features of EHL conditions (large deformation and high viscosity). First, it is assumed that the contact geometry in the inlet is very close to the deformed surfaces according to the Hertzian dry contact model [58] plus a constant film thickness representing the near constant film thickness in high pressure zone. The second assumption concerns the reduced pressure, which is based on the Barus viscosity-pressure relation and the Weibull-transformation [110]. Following from the large increase in viscosity, it is assumed that the reduced pressure rises to its maximum value already at the end of the inlet zone of the EHL contact. In the years after, when powerful numerical solutions became available and novel experimental methods

were developed, it appeared that the Ertel solution is quite accurate. A more detailed discussion on the Ertel solution can be found in section 3.1.1.

Greenwood [47] was able to calculate the constriction near the outlet and its accompanying pressure spike, so that an analytical solution of the minimum film thickness was available too.

Ertel's method of solution can also easily be applied to circular contacts. This solution is for instance used as an elastic-piezo asymptote in the Nijenbanning-diagram for elliptical contacts [88].

Numerical solutions started with the work of Petrusevich in 1951 [90], after whom the pressure spike is named. Dowson and Higginson published extensive numerical results on line contacts in 1966 [29]. The fact that their expression for film thickness is still widely used today, emphasizes the importance of this paper. For elliptical contacts the work of Hamrock and Dowson [54] was the first landmark. Others (Archard and Cowking [4], Hamrock and Jacobson [55], Chittenden et al. [21]) also developed general predictive film thickness formulas, each having its own region of validity.

An important step toward a complete film thickness map was initiated by the work of Lubrecht [80] and Venner [101]. By using multigrid techniques, they were able to build a very efficient and robust solver. Moes [85, 86] combined their numerical work with four asymptotic solutions to a general film thickness map for line contact, whereas Nijenbanning et al. [88] did the same for elliptical contacts.

2.3 Film thickness calculation for micro-EHL

2.3.1 Statistical approach

Once the determination of the central film thickness was established, the focus shifted towards surface roughness. The importance of surface topography on film thickness was recognized early. Initially, a statistic approach was followed to incorporate the roughness, since this method did not require sophisticated numerical algorithms which were not available yet. Essentially, the method involves the derivation of a so-called averaged Reynolds equation, based on the characterization of the roughness by statistical numbers like the R_q (the root mean square value of the roughness), the average orientation or the auto-correlation length of the roughness. Some examples are the work of Tzeng and Saibel [100], Christensen and co-workers [23, 24, 25, 26] and Elrod [31]. Probably the most well-known and widely used method is the flow factor method as introduced by Patir and Cheng in 1978 [89].

With respect to rough surfaces, the statistic approach has some limitations. First, this model is based on statistical averages of the surface topography described by only three parameters (the RMS roughness of both surfaces and the orientation of the composite roughness). Many surfaces have the same numbers in terms of these parameters, but a completely different behaviour with respect to film thickness. Another limitation is the neglect of the deformation of the asperities. Particularly in line contact, the change in asperity shape due to the locally high pressures has a large influence on the film thickness and thus on the wear and friction characteristics.

2.3.2 One-sided features and waviness

In the years following, slowly more and improved numerical methods became available. This made a full deterministic transient analysis of surface roughness possible, which basically solved all the problems with the flow factor model. At first, a considerable part of the research was concerned with the passage of single features through the complete contact, such as bumps and dents, shortly followed by waviness. Venner [101] studied the overrolling of a bump in line contact at conditions typical for bearings, more specific $M = 100$ and $L = 11$, where M and L are the two dimensionless parameters governing the operating conditions as proposed by Moes [85]. A bump with an amplitude of about 9 times the smooth surface central film thickness and a width of about a quarter of the Hertzian contact zone was used. For these dimensions it is found that at the center of the contact, the passage of such a bump leads to a significant increase in the pressure and, surprisingly, also to an increase in film thickness (max 20%). Compared to the case in which the bump is fixed somewhere in the contact, i.e. a steady state condition, an important difference can be observed. In the transient case the influence of the bump on the film thickness is clearly visible, whereas in the stationary case the change in film thickness can hardly be noticed. This is explained by the large reduction of the Poiseuille flow due to an extreme increase in viscosity. Mass conservation combined with Couette flow dominance leads to the fact that the film thickness is not able to vary much, despite the presence of a surface irregularity.

Very interesting are the results when sliding is introduced. Venner [101] shows that the change in film thickness in the inlet induced by a dent, travels through the contact at the average surface velocity, whereas the location of the change in pressure is stuck to the location of the feature, see Figure 2.3. The same effect was observed by Venner and Lubrecht [106] in case of sinusoidal waviness. Again mass conservation combined with

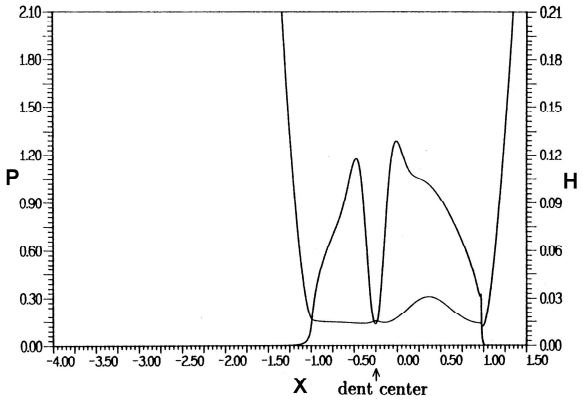

Figure 2.3: Case $M = 100$ and $L = 11$. Dimensionless pressure $\mathsf{P} = p/p_H$ and film thickness $\mathsf{H} = h/h_H$ as a function of dimensionless x-coordinate $\mathsf{X} = x/a$. Transient solution of passing of a dent in the case of $S = 1$ (smooth surface is moving faster) when dent is at $\mathsf{X} = -0.25$. Reproduced from [101].

the lack of Poiseuille flow are responsible for the film thickness variation. This behaviour is experimentally observed by, for instance, Wedeven and Cusano [109] and Kaneta et al. [75].

Ai and Zheng [3] used a similar contact situation, i.e. a bump located on one side. Compared to Venner [101] a lightly loaded system was investigated: $M = 3.7$ and $L = 10.8$, which corresponds to a maximum Hertzian pressure of 0.33 GPa. However, they included non-Newtonian Eyring behaviour in their calculations, where Eyring parameter τ_0 was set to 5 MPa. First, they studied the case of simple sliding with the smooth surface moving. From the results they conclude that the change in film thickness is mainly influenced by the asperity width, whereas the change in pressure is mainly influenced by the height of the asperity. Furthermore, it is found that for a wider asperity with small height (length more than an eighth of the Hertzian contact length and height less than the smooth film thickness) it is possible to generate a full lubricant film.

Secondly, Ai and Zheng [3] let the asperity move through the contact. They considered three cases: when the asperity moves slower than the smooth surface, pure rolling and the case when the asperity moves faster than the smooth surface. Figure 2.4 shows the film thickness of the asperity tip as a function of its location. All curves have been

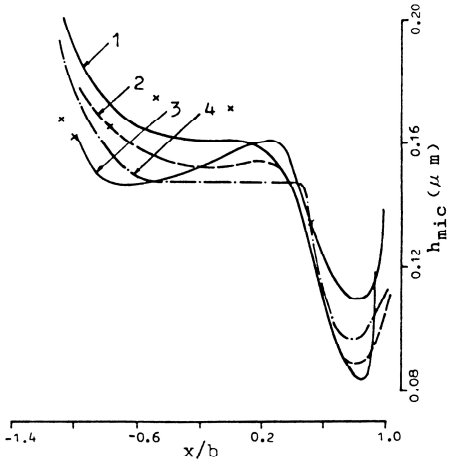

Figure 2.4: Variation of the minimum micro-EHL film thickness under the asperity tip h_{mic} as a function of its location, given by the dimensionless coordinate x/b, where b is half the Hertzian contact width. Reproduced from [3].

Curve 1	:	$u_{asp} = 0.7$ m/s,	$u_{smth} = 0.0$ m/s,	$S = -2$
Curve 2	:	$u_{asp} = 0.5$ m/s,	$u_{smth} = 0.2$ m/s,	$S = -0.86$
Curve 3	:	$u_{asp} = 0.2$ m/s,	$u_{smth} = 0.5$ m/s,	$S = 0.86$
Curve 4	:	$u_{asp} = 0.35$ m/s,	$u_{smth} = 0.35$ m/s,	$S = 0$

calculated using the same sum velocity, only the slip was varied. They conclude that the deformation pattern of the asperity is strongly dependent upon the velocity of the asperity relative to the opposite surface. When the asperity moves faster, the deformation

is completed in the inlet, whereas in case the asperity moves at a lower velocity, it deforms gradually in the middle region of the macro contact. Further, it is observed that the minimum film thickness occurs in the macro constriction region. The faster the asperity moves relative to the opposite surface, the smaller the minimum film thickness.

Chang et al. [18] investigated a slightly higher loaded EHL line contact ($M = 9$ and $L = 11$) under isothermal Newtonian conditions as well as isothermal non-Newtonian (Eyring model) conditions. The height of the sinusoidal shaped asperity was chosen equal to the smooth central film thickness. The width of the asperity was a quarter of the total Hertzian contact width, still relatively large for practical use.

For the film thickness as well as for the pressure distribution it was observed that in case of pure rolling the difference between the Newtonian and Eyring results was not large. For simple sliding with a stationary asperity however, the asperity was less flattened out and the pressure variations were smaller if the Eyring model was used instead of the Newtonian model. For a moving asperity (smooth surface stationary) the same observation was made.

When the asperity was located in the center of the macro contact, the difference in results between the two simple sliding cases was not large, particularly when the Newtonian model was used. In the Eyring model the results for the two sliding cases seem to be more or less opposite to each other, indicating the importance of the velocity of the smooth surface relative to the ridge. For a centrally located asperity, pure rolling gave quite different results from sliding. The asperity was less flattened out and the pressure variations were smaller. The difference between the rolling results and the sliding results are less for the Eyring model than for the Newtonian model. This can be attributed to non-Newtonian effects in sliding, which cause less asperity flattening and pressure variation in case of sliding.

Chang et al. [18] also studied a stationary asperity located in the inlet. In case of a stationary asperity, they observe a reduction of the overall film thickness (Newtonian: 15%; Eyring 30%). It seems that the asperity is simply blocking the inlet. In case of a stationary smooth surface or pure rolling the overall film thickness is nearly unaffected. For a moving asperity and Newtonian fluid, they observed an extreme pressure peak, about 2.5 times the maximum Hertzian pressure. If the Eyring model is used, this pressure peak is much smaller, approximately equal to the maximum Hertzian pressure.

Venner and Lubrecht [105] investigated the passage of a transverse ridge in an isothermal Newtonian EHL point contact under rolling/sliding. The load was relative light, maximum Hertzian pressure 0.54 GPa, but already high enough to limit the Poiseuille flow considerably. The dimensions of the ridge are: height 0.2 μm (1.3 times the smooth central film thickness) and width 0.07 mm (0.2 times the Hertzian contact diameter). These dimensions and load match with the experiments of Kaneta et al. [75]. Thus, both a qualitative and quantitative comparison could be made.

In the simple sliding case with the rough surface stationary, it appears that the ridge is almost completely flattened out, only near the edges the film thickness is affected. The results of the pure sliding case agree very well with the experimental results from [75], see Figure 2.5.

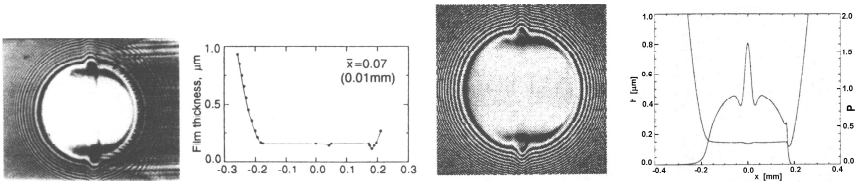

(a) Measured (b) Calculated

Figure 2.5: Interferograms and midplane film profiles at pure sliding (stationary rough surface). Reproduced from (a) [75] and (b) [105].

When a rolling component is introduced, the behaviour observed is similar to the behaviour as found for the line contact situation in [101]. In particular, this applies to the center line in the running direction of the contact. Due to absence of pressure induced flow, a film thickness variation generated in the inlet travels through the contact at half the sum velocity. The width of the variation depends on the ratio between half the sum velocity and the velocity of the ridge. Towards the edge however, the Poiseuille flow becomes more significant. Hence, the film thickness propagation does not occur and the main changes in film thickness occur during the passage of the ridge. This results into a "moon shaped" film thickness variation. This characteristic film shape is confirmed experimentally by Kaneta et al. [75], as illustrated in Figure 2.6. Similar behaviour is observed by for instance Glovnea et al. [46].

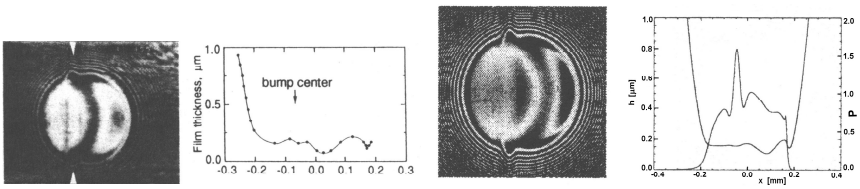

(a) Measured (b) Calculated

Figure 2.6: Interferograms and midplane film profiles at $S = 1$. Reproduced from (a) [75] and (b) [105].

Under pure rolling conditions, as expected, no difference between the velocity of the pressure variation and the film thickness variation is observed. However, the film thickness before the leading edge increased more than the film thickness at the trailing edge. Once more the experimental results agree well with the numerical simulations (Figure 2.7).

In the second simple sliding case, i.e. a moving rough surface, again a film thickness modulation is introduced which moves at half the sum velocity which depends on the level of the pressure induced flow. However, in contrast to the case in which the asperity is moving slower than the smooth surface, the film thickness modulation is replaced by an area of increased film. This can be explained by the modulations caused by the

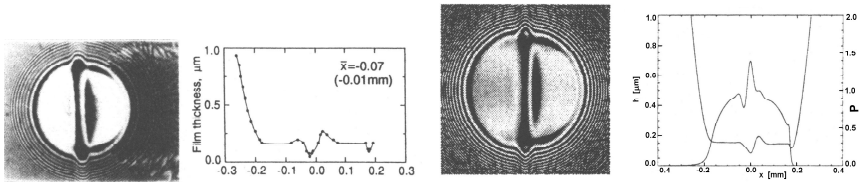

(a) Measured (b) Calculated

Figure 2.7: Interferograms and midplane film profiles pure rolling. Reproduced from (a) [75] and (b) [105].

ridge geometry as chosen by the authors. The film thickness increase due to the leading shoulder of the ridge interacts with the ridge itself as it overtakes the film thickness increase while entering the high pressure regime. Hence, the film thickness decrease caused by the "real" ridge is canceled out by the film thickness increase caused by the leading shoulder.

In case of multiple transverse ridges, Kaneta et al. [76] found that the shear flow dominance effects are still present, however on a smaller scale. In later experimental work, Kaneta and Nishikawa [74] found that particularly in the case when the rough surface moves faster than the smooth one, shear flow dominance could be hardly recognized. Therefore, they conclude that multiple irregularities (roughness of short wavelength) seem to reduce the shear flow effects.

Ai and Cheng [1] investigated the influence of orientation of waviness as well as real random surface roughness under Newtonian conditions and pure sliding with the rough surface stationary. They studied three orientations: transverse, longitudinal and diagonal (45°). It is found that in case the orientation was diagonal, a substantial part of the lubricant did not flow through the valleys. Due to the absence of pressure induced flow, this part cuts through the ridges following the rolling direction. As a result, longitudinal wavy passages are formed.

Provided that the ratio between the waviness amplitude and the smooth surface film thickness was larger than one, the minimum film thickness was found in case the waviness was oriented diagonally. However, the minimum film thickness appeared to be quite sensitive to the position of the waves, particularly in the transverse case. For the calculations, the position of the ridge in the transverse case was such that the waviness decreased the overall film thickness.

Three-dimensional asperities in line contact situation are studied by Ai et al. [2]. To take into account the effect of non-Newtonian behaviour of the lubricant, the Eyring model is applied. The contact is moderately loaded: $M = 37$ and $L = 10$ ($p_H \approx 1.1$ GPa). First a single stationary sinusoidal asperity was investigated. The results showed that an increase of the asperity width in running direction led to a decrease of the asperity tip film thickness and to a decrease of the pressure fluctuation. An increase of the asperity

width perpendicular to the running direction showed a decrease in pressure fluctuation as well. However, the asperity tip film thickness was slightly increased.

Secondly, a moving bump was studied at a slide to roll ratio of ± 0.5. In case the bump is located on the slower moving surface, a pressure fluctuation is formed at the trailing side of the bump. The film thickness variation caused by the pressure fluctuation in the inlet is traveling at the same velocity as the bump.

Although the maximum Hertzian pressure seems to be sufficiently high to reduce the Poiseuille flow to a minimum, they do not mention the occurrence of a film thickness variation traveling at the mean surface velocity caused by the Couette flow dominance and mass conservation.

Experimental results involving three-dimensional asperities are presented by Kaneta and Cameron [73]. They found that under pure rolling conditions the bumps did not deform much. Under pure sliding the bumps were much more flattened, each having a micro-constriction at the leading edge or at the trailing edge of the bump, depending on the velocity of the lubricant relative to the bump. In some cases such a constriction was also found under pure rolling conditions, by Kaneta and Cameron referred to as the micro squeeze effect.

Recently, Choo et al. [22] studied the influence of arrays of semi hemispherical bumps on film formation in point contact. Under thin film and rolling-sliding conditions they observed shear flow dominance effects, as illustrated in Figure 2.8(a). At lower slide-to-roll, i.e. smaller than 30%, this revealed itself as a wedge shape at the asperity contact. At

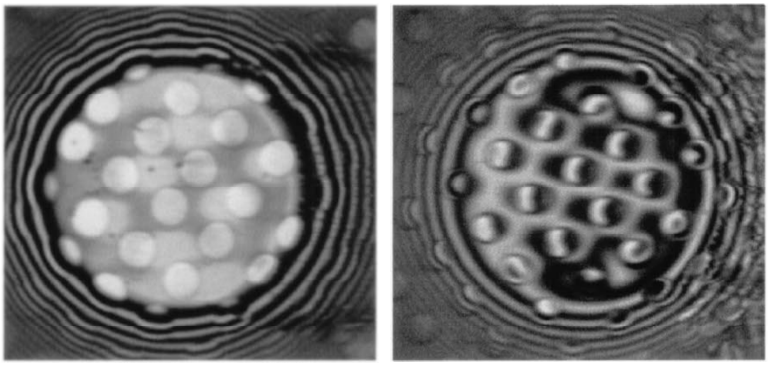

(a) Thin film, $S = 0.7$ (b) Thick film, $S = -0.7$

Figure 2.8: Interferograms showing (a) shear flow dominance and (b) development of steady state micro film. Reproduced from [22].

larger slip the pressure flow perturbation was clearly detached from the asperity and was slightly stretched as it passed the macro contact zone. At thick film however, different behaviour was observed. At slip ratios below 30%, film shapes are very similar to the shapes as found under thick film, pure rolling conditions. At higher slip ratios, once the film perturbation was convected away, the micro film shape evolved to shapes similar to

general steady state EHL contacts. Evidence for flow around the bumps was found as well. From this observation they conclude that under thick film conditions lower shear stresses allow flow in transverse direction. However, an estimation of the shear stress (with Barus $(u_d/h)\eta_0 \exp(\alpha p_H)$) in a smooth contact at the lowest slip ratios gave values of around 200 MPa. This is much larger than the characteristic Eyring stress of about 5-10 MPa. Therefore, shear thinning effects are thought to occur in the smooth contact as well as at the bumps.

For pure rolling, Choo et al. [22] observed the micro squeeze effect as mentioned by Kaneta and Cameron [73] as well, although for a thin film the asperity film shape changed to a more wedge shaped area. Interestingly, they were able to predict the (thin) film thickness under the contact in an elegant way, see Figure 2.9. Basically they modified

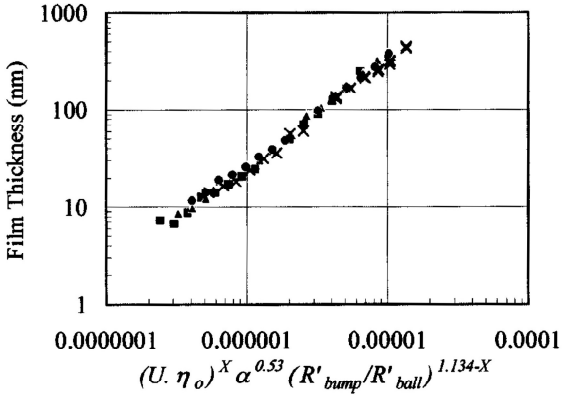

Figure 2.9: Correlation of film thickness at the asperity tip (■, ▲,) with smooth contact predictions ( ). U is the sum velocity, X is a fit parameter, R is the reduced radius of curvature. Pure rolling conditions. Reproduced from [22].

the general film thickness formula as proposed by Hamrock and Dowson [54]. For this purpose they used the work of Guangteng et al. [52], who hypothesized that the film thickness is determined by the local reduced radius of curvature (combined radius of curvature of the macro contact and the local bump).

2.3.3 Asperity collision

Parallel to the work on so-called one-sided features, the interaction between two features, generally denoted as asperity collision, was studied as well. The work of Fowles [40, 41, 42] was the first landmark in this field. He found films as small as 5 nm for low sliding velocities and at the same time pressures larger than 1 GPa. From these results Fowles concluded that it is very questionable that the assumptions like Newtonian fluid and bulk behaviour of the lubricant in the film are still valid. Fowles [43] developed a more macroscopic model, based on statistical averages of the single asperity collision theory. Using this model, he calculated coefficients of friction up to three times too high. Once more this indicates that under micro-EHL conditions the lubricant does not behave in a Newtonian manner.

Ai and Zheng [3] also provide an analysis of asperity collision. They have taken a lightly loaded EHL contact and positioned an asperity on both sides. They found that the local deformation and pressure bump both show an increase with increasing asperity height, asperity length and sliding velocity. However, at higher sliding velocities the pressure bump is somewhat restricted by non-Newtonian effects. For one case, a collision at the centre of the macro contact, they give the asperity tip radius of curvature and the minimum film thickness as a function of the asperity dimensions:

asperity height	asperity width	asperity tip radius	minimum film thickness
0.12 µm	7.5 µm	0.095 mm	0.048 µm
0.15 µm	15 µm	0.304 mm	0.047 µm

From these results it appears that the minimum film thickness is not determined by the asperity tip radius only, and that the amplitude also plays a role. Further, it is found that the minimum film thicknesses occur in the second half of the collision, when the pressure is sharply decreasing.

Collision of three dimensional asperities in a line contact is studied by Ai et al. [2]. They found that the maximum pressure fluctuation occurs just before full overlap, whereas the minimum film thickness is found in the second half of the collision. An increase of the sliding velocity leads to a larger pressure fluctuation and minimum film thickness.

Both Ai and Zheng [3] and Ai et al. [2] include non-Newtonian behaviour in their analysis. However, they do not compare their results with a Newtonian lubricant, so that the influence of non-Newtonian behaviour is not very clear.

Most studies involving asperity collision indicate that the local pressures can rise to large values. Non-Newtonian effects seem to lower the very extremes. At the same time the film thicknesses are small. Generally only parabolic shaped asperities are studied and therefore the influence of geometrical parameters such as radius of curvature and amplitude are known.

2.3.4 Amplitude reduction model

Present numerical methods make a full deterministic and transient analysis of rough surfaces feasible. More general models take full advantage of these possibilities. Probably the most extensive and detailed study was performed by Venner, Lubrecht and co-workers [102, 107, 81, 103]. They introduced the well-known amplitude reduction diagram, an elegant way of describing the effect of a single sinusoidal wave with certain wavelength and amplitude on the film thickness. As the deformation of the surface topography can be described by the linear sum of the deformations of each Fourier component of the roughness, the amplitude reduction curve combined with Fourier analysis becomes a very useful tool to calculate the deformed shape of the surface topography without extensive numerical effort, see for instance Masen et al. [84] and Morales-Espejel et al. [87]. Morales-Espejel et al. combined it with earlier work of Greenwood and Morales-

Espejel [48] to predict the pressure distribution as well. For line contacts the analytical work by Hooke [61] supported the amplitude reduction approach. Note that Hooke denotes the amplitude reduction as *clearance variation*, since under Newtonian conditions "...the original roughness is almost flattened inside the conjunction and that this component of roughness makes little contribution to the final profile" [61, p. 146]. Under rolling/sliding conditions the clearance variation is mainly caused by a wave generated in the inlet and convected at half the sum velocity through the contact. In case of an incompressible lubricant the amplitude of this wave may be even *larger* than the amplitude of the undeformed amplitude, see Hooke [61], Venner and Morales-Espejel [108]. Moreover, Venner and Morales-Espejel [108] showed that the results also apply well to two sided roughness.

After the line contact analysis, the work was first extended to circular contacts under pure rolling conditions by Venner and Lubrecht [107] and later to elliptical contacts (Venner, Kaneta and Lubrecht [103], pure rolling as well). The main observation was that the results were essentially very similar to the line contact analysis. Venner, Kaneta and Lubrecht [103] and Hooke and Venner [63] discuss this in more detail. They show that the deformation of low amplitude roughness for all contact situations is determined by the same unifying mechanism, as illustrated in Figure 2.10. Where Hooke and Venner [63] introduce a combined formula for line and circular contacts, Venner, Kaneta

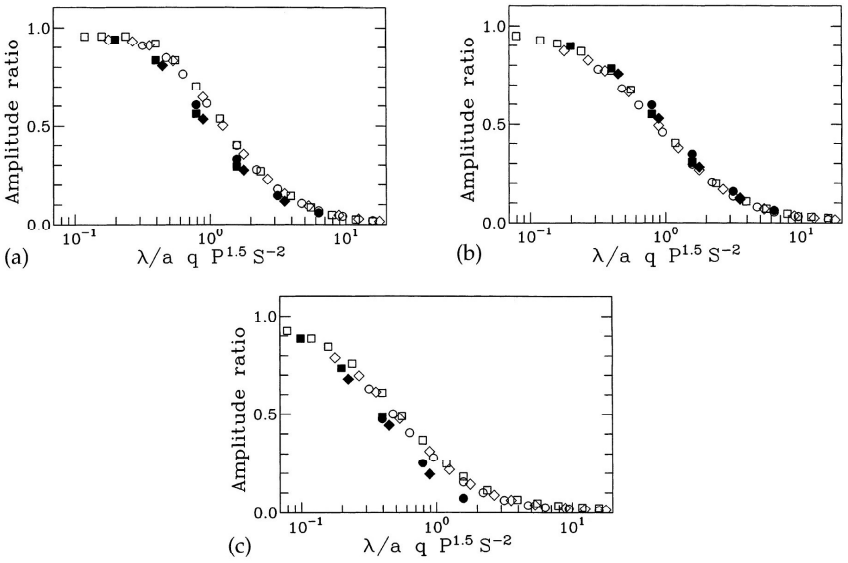

Figure 2.10: Amplitude ratio (A_d/A_i) for line contacts (open symbols) and circular contacts (closed symbols): (a) transverse roughness, (b) isotropic roughness, (c) in-line roughness. λ is the wavelength of the roughness, a is half the Hertzian contact width in running direction, q is the coefficient relating the Hertzian contact width and the pressure, P is the Greenwood load parameter, S is Greenwood speed parameter. Reproduced from [63].

and Lubrecht [103] incorporate elliptical contacts as well, leading to a general amplitude reduction formula for all contact situations under Newtonian conditions and pure rolling.

Although the amplitude reduction method proved to be very useful and has led to many new insights into the effect of roughness on the lubricant film, again it shows a disadvantage. It is valid only for low amplitude roughness, i.e. the amplitude of the roughness is not too large compared to the average film thickness. Venner and Lubrecht [107, p. 155] state that the linear relation between the initial amplitude and the deformed amplitude is lost when the initial amplitude is larger than the film thickness in case of a smooth surface. This can also be written in terms of a film thickness over roughness value. The R_q of a harmonic pattern as used in [107] is given by $1/2A_i$ and $1/\sqrt{2}A_i$ for isotropic and pure transverse/longitudinal patterns respectively, which gives a film thickness over roughness value of about $1.4 \sim 2$. Transforming this result in terms of a Stribeck curve, it means that the amplitude reduction for a single harmonic component is valid roughly up to the transition from full film to mixed lubrication. Beyond this point other models have to be developed to describe the deformation of the wave.

For line contact the limit of linearity is not easy to identify. This is caused by the absence of side flow, so that "everything that goes in must come out". The linearity holds up to at least three times the smooth film thickness, see [102]. At this large initial amplitude, the amplitude reduction diagram would predict metal-to-metal contact. However, this is compensated for by an increase in average film thickness such that the surfaces are still fully separated. In practise, this comes down to the fact that the amplitude reduction is valid only in the full film regime. This is no surprise since the Reynolds equation forms the basis of all the calculations, and no film break-through is allowed. If locally metal-to-metal contact is allowed, i.e. zero film thickness, additional restrictions are required.

Although theoretical analysis is limited to low amplitude roughness, experimental studies showed that the amplitude reduction curve can be applied under somewhat lower film thickness over roughness values. Choo et al. [22] applied the method to the deformation of an array of hemispherical bumps under pure rolling conditions. They presented a figure which is more or less equivalent to an amplitude reduction curve. However, their bumps were relatively high and even in the static case there was still some remaining bump shape visible. The amplitude reduction curve predicts smooth contact in this case (right hand side of the curves). However, if the residual bump shape in the static contact was removed from the shape, Spikes [96] showed that the results coincide remarkably well with the amplitude reduction curve as presented in [63], see Figure 2.11(a). The same observation was made for the deformation of a single ridge under pure rolling conditions, based on measurements by Glovnea et al. [46] (Figure 2.11(b)).

More evidence of the practical applicability of the amplitude reduction curve is given by Félix-Quiñonez et al. [39]. They used the method as presented in [87] and applied it to a trapezium shaped ridge in circular contact under pure rolling conditions. They found that the overall normal deformation was predicted fairly well. The local shape however, showed some differences compared to the calculated shape. Félix-Quiñonez et al. contribute this to: (1) the nature of the Fourier decomposition method when applied to a

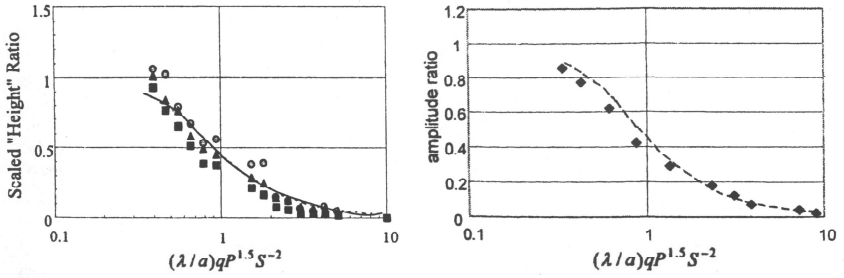

(a) Multiple hemispherical bumps (b) Single ridge

Figure 2.11: Comparison of asperity recovery with theory. Symbols represent experimental results, solid lines represent theoretical results. λ is the wavelength of the roughness, a is half the Hertzian contact width in running direction, q is the coefficient relating the Hertzian contact width and the pressure, P is the Greenwood load parameter, S is Greenwood speed parameter. Reproduced from [96].

ridge with sharp edges and flat top, (2) the deformation of each component is independent (linear behaviour) and (3) the fact that the amplitude reduction does not take the locally enhanced film in front of the asperity into account.

2.3.5 Non-Newtonian behaviour

The effect of non-Newtonian lubricant behaviour on the film thickness is another topic which is studied intensively in the last decades. As with roughness, first the effect on the global film shape was studied using smooth surfaces, see for instance [27, 64, 66, 78]. It appeared that the overall film thickness was not affected much, since the film build up is controlled by the inlet conditions. Generally, non-Newtonian effects are small in the inlet. Once local features were introduced the differences became more pronounced. Chang et al. [19] found that Eyring behaviour can reduce local pressure peaks and asperity flattening, see Figure 2.12. Moreover, the phase shift between the wave generated in the inlet and the pressure bump due to the deformation of the surface has almost disappeared. This effect was also observed by Ai et al. [2].

Jacod et al. [68] made a first step towards incorporating non-Newtonian behaviour in the amplitude reduction diagram. They found that the clearance variation of the waviness is changing from the inlet to the outlet, where it is almost constant in the Newtonian case. When they compared the relative amplitude under non-Newtonian conditions to the Newtonian results as presented by Lubrecht et al. [81], significant differences were found, in particular for $S > 0$, i.e. the rough surface is moving faster than the smooth one. This is illustrated in Figure 2.13. From the results Jacod et al. conclude that whenever loads are high and slip is present, non-Newtonian behaviour should be included.

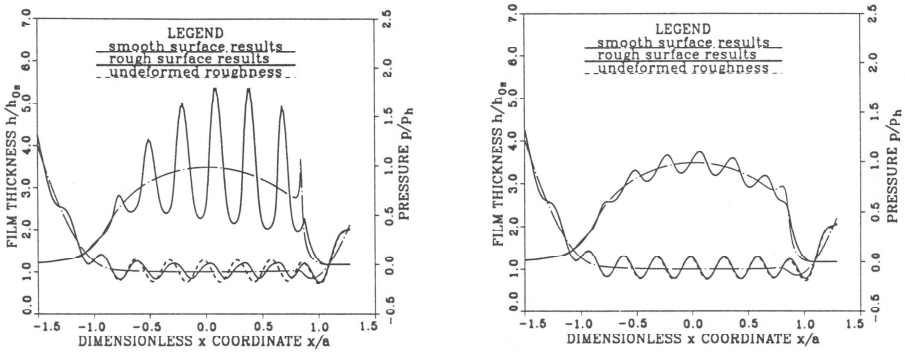

(a) Newtonian (b) non-Newtonian

Figure 2.12: Effects of the roughness-induced transients on pressure and film thickness for $S = 0.2$, (smooth surface is moving faster than rough surface). Reproduced from [19].

Further work on non-Newtonian work concerning amplitude reduction was provided by Hooke [62]. Under pure rolling he found virtually no difference between the Newtonian and the non-Newtonian case. Once sliding is introduced, the complementary wave as found in the Newtonian case has disappeared and the original waviness is simply deformed in amplitude, see Figure 2.14. Hooke also found that the type of non-Newtonian formulation did not have a large influence. For various models the results are fairly similar. The roughness orientation however, had an influence. Surprisingly, it appeared that in-line roughness leads to significant smaller clearance variation and lower pressure per-

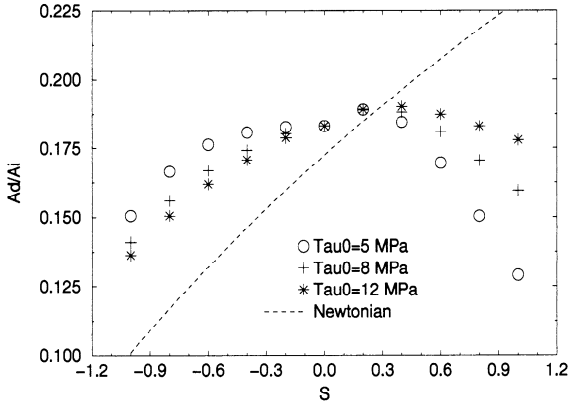

Figure 2.13: Amplitude ratio of the waviness in the centre of the contact as a function of $\mathsf{S} = -S$ for different values of τ_0 (= 5, 8 and 12 MPa) Dashed line is the relative amplitude for the Newtonian case as given in [81]. Reproduced from [68].

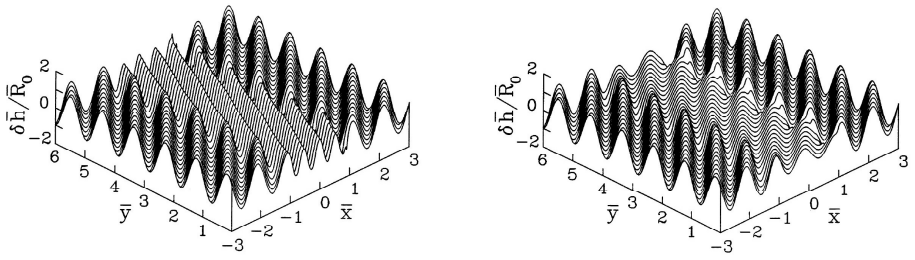

(a) Newtonian (b) non-Newtonian

Figure 2.14: Clearance perturbations under the contact. Roughness orientation at 45°, $\lambda/b = 0.75$. λ is the wavelength of the roughness, b is half the Hertzian contact width, $\delta\bar{h}$ is the dimensionless film thickness perturbation, $\bar{R}_0$ is the dimensionless initial waviness amplitude, P is the Greenwood load parameter, S is Greenwood speed parameter. Reproduced from [62].

turbation. In the Newtonian case the effect of roughness orientation was much smaller [63].

Although the general behaviour differs from the Newtonian case, within the elastic piezoviscous regime the operating conditions do not have a major effect on the results. For a fairly wide range of conditions it was found that the amplitude reduction curve still follows the same trend, as illustrated in Figure 2.15.

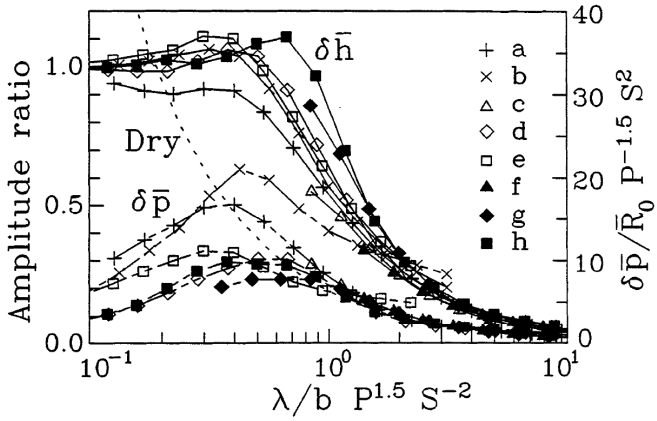

Figure 2.15: Effect of operating conditions, $S = 1$, roughness orientation at 45°.
(a) P = 10, S = 5; (b) P = 10, S = 10; (c) P = 20, S = 5; (d) P = 20, S = 10; (e) P = 20, S = 20; (f) P = 50, S = 5; (g) P = 50, S = 10; (g) P = 50, S = 20. λ is the roughness wavelength, b is half the Hertzian contact width, $\delta\bar{h}$ is the dimensionless film thickness perturbation, $\delta\bar{p}$ is the dimensionless pressure perturbation, $\bar{R}_0$ is the dimensionless initial amplitude, P is the Greenwood load parameter, S is Greenwood speed parameter. Reproduced from [62].

Venner, Kaneta, Nishikawa and Jacod [104] provide additional evidence that in case of slip and at thinner films non-Newtonian behaviour cannot be neglected. They compared numerical simulations with optical measurements of a ball on which a transverse sinusoidal pattern is sputtered in order to show the effect of asperities. In case of pure rolling the measured film thickness on a global as well as on a local scale was predicted very well by the classical Reynolds equation. When slip was introduced, the global average film thickness could still be predicted by the Reynolds equation combined with a Newtonian fluid. However, the local film shape differs significantly from the experiments. The numerical results show the effect of shear flow dominance due to the very high viscosity. Film thickness variations due to the inlet flow oscillations which are traveling at the mean velocity are clearly visible. The experimental results do not show this. Venner et al. suggest that non-Newtonian effects would sufficiently lower the pressure gradients in order to reduce the local asperity deformation. To prove this, the Eyring model was incorporated in the Reynolds equation. Indeed, these results agree much better with the experimental results, as illustrated in Figure 2.16.

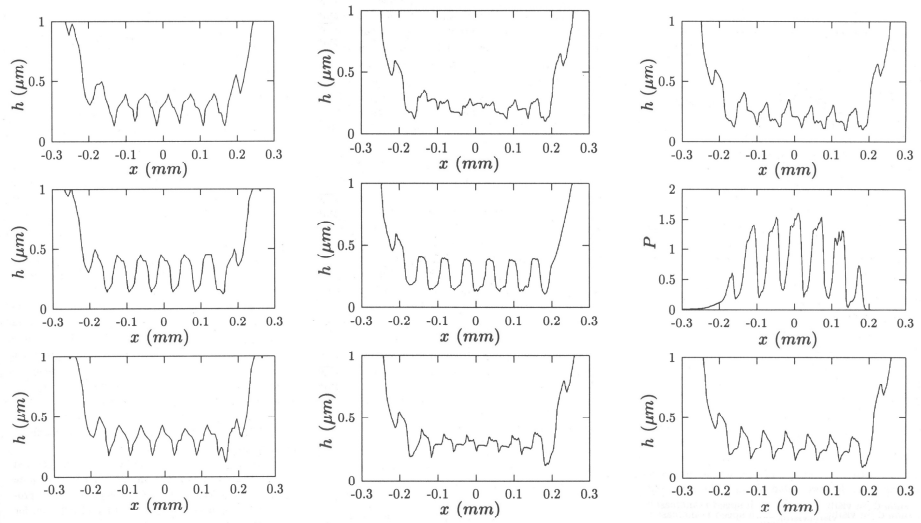

(a) Measured (b) Newtonian (calculated) (c) Non-Newtonian (calculated)

Figure 2.16: Film thickness profiles on the centerline of the contact for $S = 1$ (top), $S = 0$ (centre) and $S = -1$ (bottom). Reproduced from [104].

Recently, Elcoate et al. [30] used the same non-Newtonian model in their analysis of a line contact. However, they used real surface roughness, taken from profilometer traces. Their numerical algorithm was able to handle very thin films under various conditions. At relatively low film thickness over roughness values (minimum film thicknesses were less than 10% of the smooth film thickness) they found no evidence of the passage of a wave generated in the inlet. They contribute this (1) to non-Newtonian effects and (2) to

the valleys, which are large compared to the induced inlet waves. These valleys can act as lubricant reservoirs and may absorb the flow perturbations. A typical result of a detailed part of the surface profile is presented in Figure 2.17. As can be seen, the deformation of the asperities change only slightly as they pass the contact.

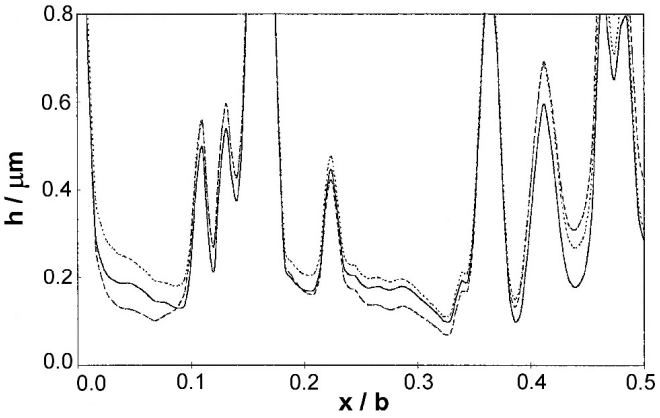

Figure 2.17: Film thickness of a part of a roughness profile for $S = 0.6$. Detailed view centred at $x/b = -0.65$ (dashed), $x/b = 0$ (solid) and $x/b = 0.65$ (dotted), where b is half the Hertzian contact width. Reproduced from [30].

Elcoate et al. also investigated the effects of the slip ratio. Figure 2.18 shows a part of the surface at the same position in the contact at different slip ratios. The figure shows clearly two types of responses to the relative sliding velocity of the asperity corresponding to positive and negative slip ratios. From these results they conclude

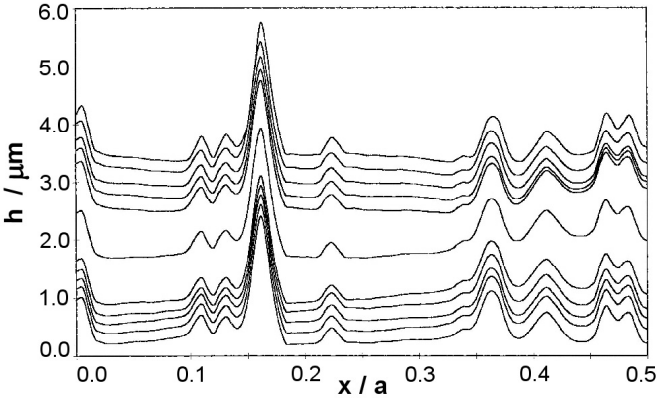

Figure 2.18: Film thickness of a part of roughness profile at the centre of the contact for $S = 2.0$ (highest curve), 1.2, 0.6, 0.3, 0.15, 0, -0.15, -0.3, -0.6, -1.2, and -2.0 (lowest curve) Each curve is offset from its neighbours by 0.2 µm; the curve for $S = 0$ is offset by 0.6 µm. Reproduced from [30].

that "...sliding is seen to have an hydrodynamic effect in micro-EHL which is absent in smooth-smooth contacts in which film formation is determined purely by the rolling velocity" [30, p. 330]. The absolute value film thickness at the asperity however, seems not to be very sensitive to the slip ratio, only the local film shape changes as the slip changes.

2.3.6 Traction experiments

Although optical interferometry has proven its value in experimental research on micro-EHL, it has a disadvantage. Due to the properties of the glass disc the maximum pressure is limited to about 0.5 GPa. In real applications however, the pressures rise to values higher than 1 GPa. In this region traction experiments on steel-steel contacts can be performed. Schipper and co-workers, [93, 94] used this method. Stribeck curves were measured on an S-tribometer (reciprocating pin sliding on a stationary counter surface), where after the experiments photographs were taken from the pin. These pictures showed that the surface in the middle of the Hertzian contact zone was nearly unaffected, especially at higher contact pressures, see Figure 2.19(a). In some cases (mild) wear occurred

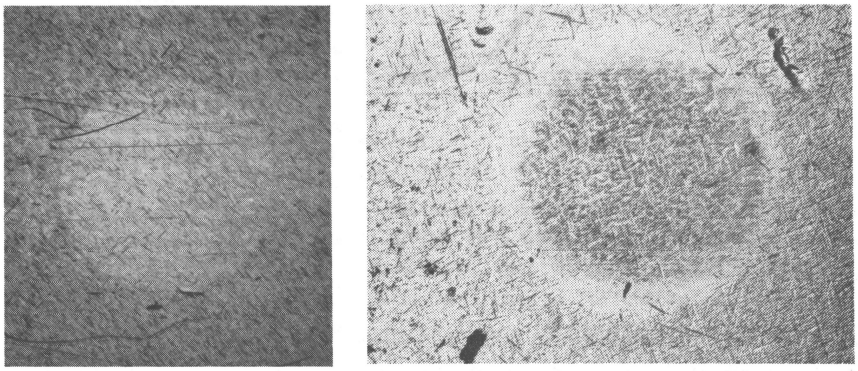

(a) (b)

Figure 2.19: Photographs of the stationary surface taken after measurement of a Stribeck curve under micro-EHL conditions. Reproduced from [93].

only in a ring shaped area with mean diameter equal to the Hertzian contact diameter, as illustrated in Figure 2.19(b). The characteristic friction coefficient related to this kind of experiments appeared to be correlated to the limiting shear stress of the lubricant divided by the mean macroscopic contact pressure (see also curve 2 of Figure 2.22). When neglecting the offset τ_{L_0}, this can be seen as the proportional constant ζ from eq. (2.5). Further, no electrical conductivity was measured. From the results it is concluded that the asperities were separated by a thin film consisting of solidified lubricant.

In case a Stribeck curve was measured by means of changing the velocity only, Schipper [93] found that in order to enter the solid state regime on a microscopic level, a higher initial macroscopic pressure is beneficial. Two possible explanations for this observation are given. To illustrate the first explanation, the lubricant chart as presented by Evans

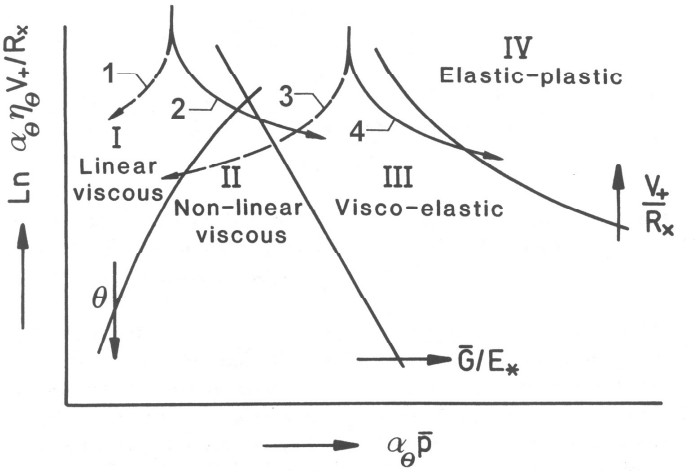

Figure 2.20: Regime chart. θ is the temperature, $\bar{G}$ is the shear modulus, E_* is the reduced modulus of elasticity, V_+ is the sum velocity, R_x is the reduced radius of curvature in running direction, $\bar{p}$ is the mean contact pressure, α_θ is the pressure viscosity index at θ and η_θ is the dynamic viscosity at θ. Reproduced from [34].

[34] is reproduced in Figure 2.20. When decreasing the velocity at low pressures, the macroscopic rheological behaviour follows curve 1, whereas the micro contacts follow curve 2. In this case the lubricant at the micro contact does not easily enter the elastic - plastic regime. However, if initially the contact is operating in the elastic - non-linear viscous regime (visco-elastic), which is the case at higher pressures, it is much more likely that on asperity level the elastic - plastic regime is entered, see curve 4. As a second explanation for the need of higher initial pressures, the larger deformation of the asperities is mentioned. This might alter the inlet conditions of the asperity such that the lubrication conditions are improved.

Another interesting observation is the fact that above a certain value of R_a no micro-EHL seemed to occur, as illustrated in Figure 2.21. This indicates that R_a could be one of the parameters controlling the occurrence of micro-EHL. However, as suggested in [94], it is unlikely that R_a is the *only* parameter, the curvature and slopes of the interacting asperities are assumed to play a very important role as well. In some cases it was observed that, while operating in the micro-EHL regime, a decrease of the sum velocity led to a change-over in friction level from micro-EHL (± 0.09) to the level of boundary lubrication (± 0.13), as indicated by curve 3 in Figure 2.22. Since the load is fully carried by the asperities, this increase cannot be explained by an increase of asperity contacts. Thermal effects causing the change-over seem to be unlikely as well, since the velocity is decreasing. Therefore a change in local lubrication conditions, i.e. micro-EHL to micro-BL, is thought to be the reason for the transition.

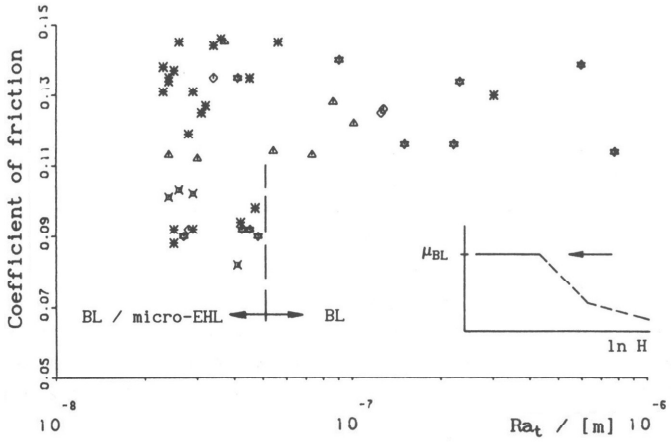

Figure 2.21: BL and micro-EHL in relation to Ra_t. Ra_t is the combined surface roughness defined as $\sqrt{R_{a,1}^2 + R_{a,2}^2}$. Reproduced from [94].

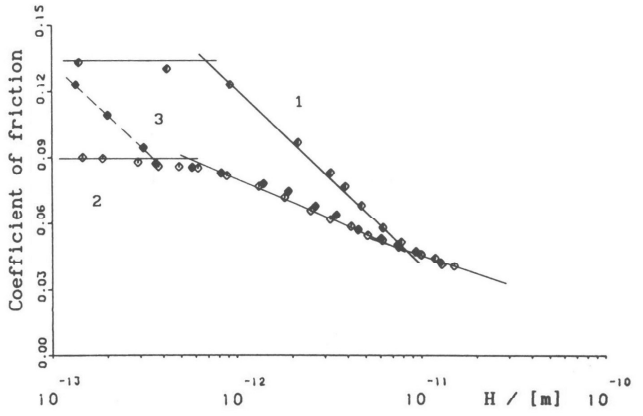

Figure 2.22: Friction curves at liquid state behaviour of the lubricant. Reproduced from [94].

2.4 Conclusion

In chapter 1 the benefits of micro-EHL are indicated. In this chapter the existing work on this topic was discussed and the limitations of this work with respect to micro-EHL analysis was indicated. The mechanisms which come up in micro-EHL are essentially the same as in conventional elastohydrodynamics, however on a smaller scale. Film formation between the asperities is initiated in the inlet region of the macro contact. Squeeze effects are mainly responsible for the pressure build-up for the low slip condition. In the Hertzian contact region, the film can be enhanced by the wedge action if sliding is

present. Another cause of film formation is the collision of asperities. In this case local squeeze and wedge effects account for the local film formation. In all stages, the film formation ability is highly dependent on the asperity geometry and the orientation of the asperity with respect to the surface velocities. Lubricant behaviour also plays an important role. Where in the lightly loaded cases Newtonian behaviour prevails, under more severe conditions non-Newtonian effects cannot be neglected. This has consequences for the film formation. Whereas under Newtonian conditions the film formation is controlled by the inlet pressure sweep, under strong non-Newtonian conditions this plays only a minor role. Then film formation under asperity tips is more a local effect and not influenced by what has happened while entering the contact.

Experimental studies mostly confirm the numerical analysis in a qualitative way (or rather, numerical analysis confirm the experiments). Even in case a quantitative comparison can be made, the agreement is remarkably well. The importance of the asperity geometry (height, width) with respect to the ability to form a lubricant film is clearly indicated. Also the significance of the absence of pressure flow is pointed out.

Unfortunately, experiments involving optical techniques are limited to maximum pressures of about 0.5 GPa, although locally it might be higher, up to 1 GPa, see Guangteng et al. [53]. However, still quite a good impression of the global as well as local phenomena which play a role at the more elevated pressures can be obtained. Traction experiments are not restricted to maximum pressures. This kind of experiments also clearly indicate the occurrence of micro-EHL in a contact. Nevertheless, detailed information about local events cannot be obtained using traction experiments. Traction data generally refer to mean values.

Regarding the quantitative prediction of film thickness, for pure rolling a start is made with the work of Guangteng et al. [52] and Choo et al. [22]. These predictions are based on a modified local radius of curvature and prove to work well under pure rolling conditions, in which the film thickness is mainly determined in the inlet and passes the highly loaded zone relatively unchanged. When slip is introduced, most experiments involving optical techniques show the propagation of inlet generated lubricant waves at the average surface velocity. This behaviour is confirmed by many numerical simulations. The waves are a result of the lack of pressure induced flow due to the high viscosity in the contact and largely determine the film thickness.

However, when entering the BL regime, it is generally assumed that the load is mainly carried by the asperities. Then film formation is determined by the local operating conditions at the micro contacts. In between the asperities the pressure is relatively low, allowing pressure induced flow and largely reducing the effect of inlet generated lubricant waves. At the same time the pressure is considerably larger than the maximum pressure used in the experiments involving optical techniques. This promotes non-Newtonian effects, which is confirmed by the traction experiments by Schipper [93]. These experiments clearly showed the solid state behaviour of the lubricant.

Chapter 3

Micro-EHL model

3.1 Outline of the approach

Film formation between asperities is initiated in the inlet region of the macro EHL contact. Under pure rolling conditions, squeeze effects are responsible for the pressure build up. In case sliding is present, wedge effects will increase or decrease the film formation in the inlet, depending on the velocity of the opposite surface relative to the surface on which the asperity is located. In the Hertzian contact region of the EHL contact however, no squeeze velocities are present. The change in film thickness under the asperity summit is purely due to the difference in velocity between the two surfaces. In all stages, the film formation ability is highly dependent on the lubricant behaviour and the asperity geometry.

This chapter discusses a newly developed model to describe the film formation under asperity summits in the highly loaded contact zone. A largely analytical approach is chosen with respect to the practical implementation of easy-to-use formulas.

3.1.1 Ertel's solution

To the author's knowledge there is only one full analytical model available to solve the film formation under EHL conditions, namely the solution of Ertel [33]. This model was briefly introduced in section 2.2.1 and forms the base of the current work. Because of its importance, Ertel's solution will be discussed now in more detail. To illustrate the solution, a typical EHL contact configuration is shown in Figure 3.1.

The derivation is started with the one dimensional steady state Reynolds equation (see also eq. (2.16)):

$$\frac{d}{dx}\left(\frac{h^3}{12\eta}\frac{dp}{dx}\right) = u_m\frac{dh}{dx} \tag{3.1}$$

Note that due to the assumption of an incompressible lubricant the density ρ is elimi-

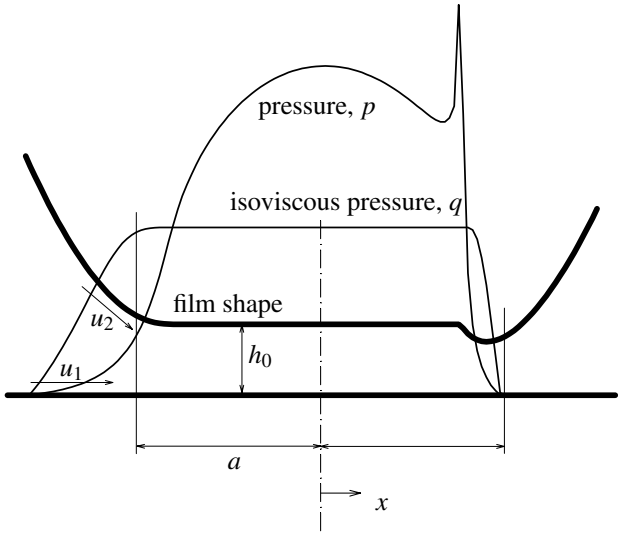

Figure 3.1: Typical film shape and pressure distribution under EHL conditions. Schematic representation.

nated. Integration of eq. (3.1) with $h = h_0$ at $dp/dx = 0$ gives:

$$\frac{1}{\eta}\frac{dp}{dx} = 12u_m\frac{h-h_0}{h^3} \tag{3.2}$$

Since the viscosity is generally pressure dependent, the left hand side of eq. (3.2) can become rather complicated. By choosing the Barus viscosity-pressure dependence and combining it with the Weibull transformation [110], Ertel was able to eliminate the pressure dependence and create an isoviscous problem. He introduced the isoviscous pressure q:

$$q = \frac{1}{\alpha}\left(1 - \mathrm{e}^{-\alpha p}\right) \tag{3.3}$$

If substituted into eq. (3.2), this equation reduces to

$$\frac{dq}{dx} = 12\eta_0 u_m\frac{h-h_0}{h^3} \tag{3.4}$$

Further, Ertel assumed that the absolute limit of q, i.e. $1/\alpha$, is already reached at the leading edge of the Hertzian contact zone, i.e. the point where $x = -a$ in Figure 3.1. Here the parameter a is half the Hertzian dry contact width [58] and reads:

$$a = \sqrt{\frac{8wR'}{\pi E'}}, \text{ with } \frac{1}{R'} = \frac{1}{R_2} + \frac{1}{R_2}, \frac{2}{E'} = \frac{1-\nu_1^2}{E_1} + \frac{1-\nu_2^2}{E_2} \tag{3.5}$$

in which w is the load per unit of length, R_1 and R_2 are the radii of curvature, ν_1 and ν_2 are the Poisson ratios and E_1 and E_2 are moduli of elasticity. Strictly, the pressure

has to rise to infinity to reach $q = 1/\alpha$. However, when assuming typical values for viscosity-pressure dependence and the maximum Hertzian pressure ($\alpha = 20$ GPa^{-1} and $p_H = 1$ GPa respectively), q reaches already 94% of its maximum at $x = -0.99a$. Note that from the above follows that in the Hertzian contact zone $dq/dx \approx 0$, so that $h \approx h_0$. This is in accordance with section 2.2.

Eq. (3.4) can also be written as

$$\int_{q(x'=-\infty)}^{q(x'=-x)} dq = 12\eta_0 u_m \int_{-\infty}^{-x} \frac{h-h_0}{h^3} dx' \tag{3.6}$$

With $q(x' = -\infty) = 0$ and $q(x' = -a) = 1/\alpha$, eq. (3.6) becomes:

$$\frac{1}{\alpha} = 12\eta_0 u_m \int_{-\infty}^{-x} \frac{h-h_0}{h^3} dx' \tag{3.7}$$

The right hand side is solved using the Hertzian dry contact theory. The gap between two solids, which in this case is an approximation of $h - h_0$, may be written as:

$$h - h_0 \approx h_l = \frac{a^2}{2R'} \left(\left|\frac{x}{a}\right| \sqrt{\left(\frac{x}{a}\right)^2 - 1} \; - \; \operatorname{arccosh}\left|\frac{x}{a}\right| \right), \quad |x| \geq a \tag{3.8}$$

Substitution into eq. (3.6) and using the right boundary conditions yields:

$$\frac{1}{\alpha} = 12\eta_0 u_m \int_{-\infty}^{-a} \frac{h_l}{(h_l + h_0)^3} dx \tag{3.9}$$

Ertel approximated the right hand side using a numerical technique. His final result for the film thickness reads:

$$h_0 = 1.175 \frac{\alpha^{0.727} {\eta_0}^{0.727} {u_s}^{0.727} {R'}^{0.364} {E'}^{0.091}}{w^{0.091}} \tag{3.10}$$

However, another fair approximation can be obtained if the Crook approximation [28] for h_l is used:

$$h_l \approx \frac{a^2}{R'} \frac{2\sqrt{2}}{3} \left(\left|\frac{x}{a}\right| - 1 \right)^{3/2} \tag{3.11}$$

Now eq. (3.9) can be solved in closed form, yielding:

$$h_0 = \frac{2^{9/8} \pi^{7/8}}{3^{11/8}} \; \frac{\alpha^{3/4} {\eta_0}^{3/4} {u_s}^{3/4} {R'}^{3/8} {E'}^{1/8}}{w^{1/8}} \tag{3.12}$$

This is only slightly different from the original Ertel solution.

3.2 The micro-EHL line contact model (2D asperity)

The derivation of the new micro-EHL model starts with the most straightforward case: a two dimensional asperity. This can be seen as the passage of a transverse cylinder in line contact. Note that similar to the Hertzian dry contact theory the cylindrical shape will be approximated by a parabola. Figure 3.2 shows schematically the 2D micro-EHL problem as used in the present work. Based on this graphical representation of the problem, the

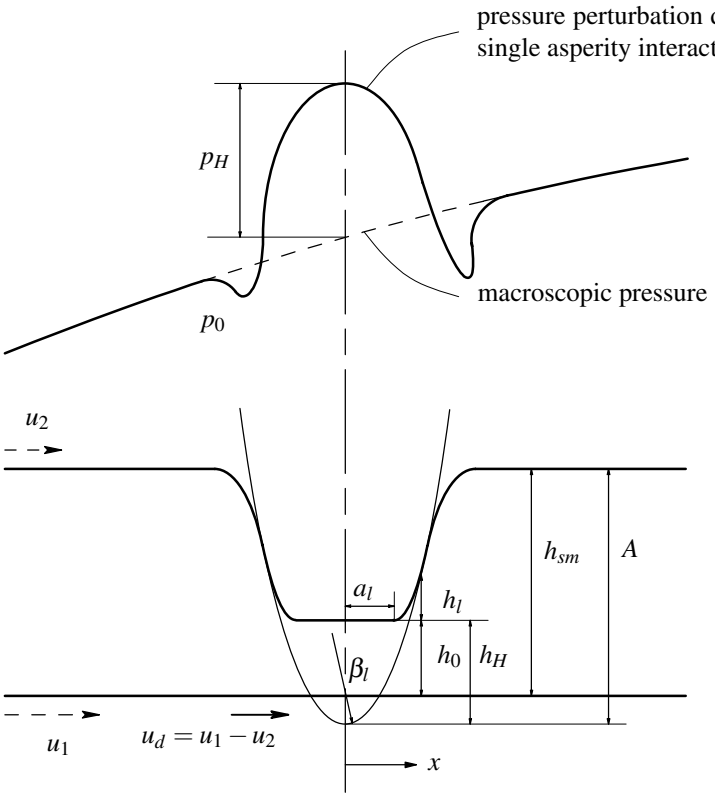

Figure 3.2: Micro-EHL model for cylindrical asperity

equation which gives the film thickness under the asperity summit will be derived.

3.2.1 Assumptions

Before the derivation starts, some assumptions are made to reduce the complexity of the approach.

1. As a first approximation, the lubricant is assumed to behave in a Newtonian way.
2. The compressibility of the lubricant is neglected.

3. The analysis is limited to isothermal conditions.

4. With respect to the asperity deformation it is assumed that the asperity deforms like a macro contact under EHL conditions. Such behaviour is experimentally observed by for instance Choo et al. [22]. This implies that according to Ertel's approach the deformation of the asperity is assumed to follow the Hertzian deformation. The global Hertzian pressure p_0 is considered to be locally constant. It is assumed to act as an elevated ambient pressure and has therefore no influence on the asperity deformation. This deformation is governed solely by the pressure perturbations.

5. Furthermore, it is assumed that the formation of the micro-film is relatively fast compared to the changes in operating conditions on micro scale. This means that the asperity contact can be considered as a quasi steady state situation.

3.2.2 Equations

The aim of the modelling is to find an expression for h_0 as a function of the lubricant parameters (α and η_0), the asperity geometry (β_l and A), the material (E'), the operating conditions load and velocity of the macro contact (p_0 and u_d) and the surrounding film thickness h_{sm}. The parameter h_{sm} follows from a general film thickness formula applied to the smooth macro EHL contact. Note that it is assumed to be constant in the vicinity of the asperity. The surrounding pressure p_0 is determined using the Hertzian pressure of the smooth macro contact at the position corresponding to the position of the asperity in the macro contact. From Figure 3.2 the following expression for h_0 can be deduced:

$$h_0 = h_{sm} - A + h_H \tag{3.13}$$

The term h_H is the Hertzian deformation of the system asperity - smooth surface. When determining h_H a complication arises. For a point contact the maximum deformation, i.e. the deformation at the asperity summit, is given by $h_H = a_s^2/\beta_s$ with a_s the Hertzian contact radius and β_s the radius of curvature of the spherical asperity, see for instance Johnson [70, ch. 4]. For a line contact situation however, the maximum deformation is somewhat arbitrary due to the nature of the equations. The displacement at a certain location x due to a normal pressure distribution $p(x)$ is given by [70]:

$$v(x) = -\frac{4}{\pi E'} \int_{-\infty}^{\infty} p(x') \ln \left| x - x' \right| dx' + C \tag{3.14}$$

The constant C is determined by fixing the deformation at a certain distance from the contact to *zero*. Since the location of *zero* deformation is arbitrary, and with that the maximum deformation at the asperity summit, an assumption has to be made on this. At this point the maximum deformation is chosen similar to the maximum deformation in the point contact situation:

$$h_H = \frac{a_l^2}{\beta_l} \tag{3.15}$$

With $p(x)$ equal to the Hertzian dry contact pressure distribution, this corresponds to *zero* deformation at approximately $2.3a_l$ from the centre of the asperity contact. In section 3.2.4 will be shown that the maximum deformation agrees fairly well with numerical simulations. Note that for numerical analysis on general EHL contacts the constant C does not need to be specified. It is incorporated in the unknown integration constant of the film thickness equation (in fact h_0) and determined by the force balance equation, see for instance [101]. In the Ertel's macroscopic analysis a similar approach is followed. Only h_0 is determined, implicitly the constant is chosen such that the deformation changes the shape of the surface into the Hertzian dry contact geometry.

Using eq. (3.5), eq. (3.15) can also be written as:

$$h_H = \frac{8w}{\pi E'} \tag{3.16}$$

where w can be seen as the load needed to deform the asperity with h_H. Substitution of this into eq. (3.13) gives h_0 as a function of the given parameters h_{sm}, A, E' and the unknown w:

$$h_0 = h_{sm} - A + \frac{8w}{\pi E'} \tag{3.17}$$

To solve h_0 another relation between h_0 and w is needed. This relation is deduced from the Reynolds equation for line contact:

$$\frac{d}{dx}\left(\frac{h^3}{12\eta}\frac{\partial p}{\partial x}\right) = \frac{u_d}{2}\frac{dh}{dx} \tag{3.18}$$

Following Ertel's approach, integration of eq. (3.18) with boundary condition $h = h_0$ if $dp/dx = 0$ gives:

$$\frac{1}{\eta}\frac{dp}{dx} = 6u_d\frac{h-h_0}{h^3} \tag{3.19}$$

Substitution of the iso-viscous pressure, see eq. (3.3) and the Hertzian gap geometry, see eq. (3.8), results into:

$$\frac{dq}{dx} = 6\eta_0 u_d \frac{h_l}{(h_l+h_0)^3} \tag{3.20}$$

For h_l the Crook approximation as given by eq. (3.11) will be used.

To reduce the number of parameters involved, dimensionless groups will be introduced. Since the deformation is assumed to be Hertzian, it is convenient to use Hertzian parameters for this purpose. For the spatial coordinate ($\hat{x}$) and the film thickness ($\hat{h}$) this will be the Hertzian contact width and the maximum Hertzian deformation respectively. The isoviscous pressure is scaled on the inverse of the pressure viscosity index.

$$x = \hat{x}\bar{x} = a_l\bar{x}, \quad h = \hat{h}\bar{h} = \frac{a_l^2}{\beta_l}\bar{h}, \quad q = \hat{q}\bar{q} = \frac{1}{\alpha}\bar{q} \tag{3.21}$$

This results into the following dimensionless equation:

$$\frac{\partial \bar{q}}{\partial \bar{x}} = \mathcal{L}\frac{\bar{h}_l}{(\bar{h}_l+\bar{h}_0)^3} \tag{3.22}$$

where:

$$\bar{h}_l(\bar{x}) = 0\,, \qquad |\bar{x}| < 1 \tag{3.23}$$

$$\bar{h}_l(\bar{x}) = \frac{2\sqrt{2}}{3}\left(|\bar{x}| - 1\right)^{3/2}, \qquad |\bar{x}| \geq 1 \tag{3.24}$$

$$\mathcal{L} = 6\eta_0 u_d \frac{\hat{x}}{\hat{q}\hat{h}^2} = \frac{3\pi^{3/2}}{8\sqrt{2}}\eta_0 \alpha u_d E'^{3/2} w^{-3/2} \beta^{1/2} \tag{3.25}$$

Analogous to eq. (3.6), eq. (3.22) can be written as:

$$\int_{\bar{q}(\bar{x}=-\infty)}^{\bar{q}(\bar{x}=-1)} d\bar{q} = \mathcal{L} \int_{-\infty}^{-1} \frac{\bar{h}_l}{(\bar{h}_l + \bar{h}_0)^3} d\bar{x} \tag{3.26}$$

Working out the left hand side with $p = p_0$ at $\bar{x} = -\infty$ yields:

$$\int_{1-\mathrm{e}^{-\alpha p_0}}^{1} d\bar{q} = \mathrm{e}^{-\alpha p_0} \tag{3.27}$$

To solve the right hand side, first it is rewritten into:

$$\mathcal{L} \int_{1}^{\infty} \frac{\tilde{h}_l}{(\tilde{h}_l + \bar{h}_0)^3} d\bar{y} \tag{3.28}$$

where:

$$\tilde{h}_l = \frac{2\sqrt{2}}{3}\left(\bar{y} - 1\right)^{3/2} \tag{3.29}$$

Next, the following transformation is used:

$$z^3 = \frac{\tilde{h}_l}{\bar{h}_0} = \frac{2\sqrt{2}}{3\bar{h}_0}\left(\bar{y} - 1\right)^{3/2}, \quad d\bar{y} = 2\left(\frac{3\bar{h}_0}{2\sqrt{2}}\right)^{2/3} z\,dz \tag{3.30}$$

As a result, eq. (3.28) changes into:

$$\frac{2\mathcal{L}}{\bar{h}_0^2}\left(\frac{3\bar{h}_0}{2\sqrt{2}}\right)^{2/3} \int_{0}^{\infty} \frac{z^4}{(z^3+1)^3} dz \tag{3.31}$$

The integral in eq. (3.31) reads $2\pi 3^{-7/2}$, which finally, for the right hand side of eq. (3.26) gives:

$$2\pi 3^{-17/6} \bar{h}_0^{-4/3} \mathcal{L} \tag{3.32}$$

Substitution of eq. (3.27) and eq. (3.32) into eq. (3.26) leads to:

$$\bar{h}_0^{4/3} = 2\pi 3^{-17/6}\mathcal{L}e^{\alpha p_0} \tag{3.33}$$

or, with eq. (3.21) and eq. (3.25), in parametric formulation:

$$h_0^{4/3} = 2\pi 3^{-17/6}\mathcal{L}e^{\alpha p_0}\hat{h}^{4/3} = 2^{3/2}\pi^{7/6}3^{-11/6}\eta_0 u_d \alpha^* {E'}^{1/6} w^{-1/6}{\beta_l}^{1/2} \tag{3.34}$$

In eq. (3.34) the parameter $\alpha^* = \alpha e^{\alpha p_0}$ is introduced, which originally is proposed by Blok [17]. It is based on the parametric form of eq. (3.27):

$$\int_{(1-e^{\alpha p_0})/\alpha}^{1/\alpha} dq = \frac{e^{-\alpha p_0}}{\alpha} = \frac{1}{\alpha^*} \tag{3.35}$$

With this parameter it is possible to study the influence of any viscosity-pressure relationship on h_0. Section 3.2.5 will discuss this in more detail. Note that from eq. (3.34) it is a small step to Ertel's solution as given by eq. (3.12).

Eq. (3.34) is the second relation between h_0 and w. The next step is solving h_0 from eq. (3.17) and (3.34). From eq. (3.17) follows:

$$w = \frac{\pi}{8}E'(h_0 - h_{sm} + A) \tag{3.36}$$

Substitution of eq. (3.36) into eq. (3.34) gives:

$$h_0^{4/3}\left(\frac{\pi}{8}E'(h_0 - h_{sm} + A)\right)^{1/6} = 2^{3/2}\pi^{7/6}3^{-11/6}\eta_0 u_d \alpha^* {E'}^{1/6}{\beta_l}^{1/2} \tag{3.37}$$

or:

$$h_0\left(1 + \frac{\mathcal{A}}{h_0}\right)^{1/9} = C_l(\eta_0\alpha^* u_d)^{2/3}{\beta_l}^{1/3} \tag{3.38}$$

where:

$$\mathcal{A} = A - h_{sm} \tag{3.39}$$

$$C_l = \pi^{2/3}2^{4/3}3^{-11/9} \tag{3.40}$$

This equation can be seen as a general formula which represents the influence of various parameters on the film thickness under an asperity summit. From the result it can be seen that the lubricant parameters (η_0 and α^*) and the sliding velocity affect the film thickness most. In particular α^*, which depends exponentially on p_0, can vary much. More on the influence of the lubricant parameters as well as a discussion of other models given in section 2.1.2 can be found in section 3.2.5. The local modulus of elasticity of the asperity does not affect the film thickness. Similar behaviour is found experimentally by Choo et al. [22] under pure rolling conditions, who found that local film thickness is predicted fairly well, even if the influence of chromium instead of steel is neglected. Further, it is observed that the amplitude is of minor importance, for large A its power is

only $1/9$. Since an increase of amplitude can also be seen as an increase of local loading (see eq. (3.36)), this behaviour is comparable to the influence of load in traditional EHL formulas, where the load is also of less importance for film formation. The other geometry parameter, the radius of curvature, does play a role, although its significance is not as large as the lubricant parameters and the sliding velocity.

3.2.3 Region of validity

Since Ertel's solution is an approximation of the film thickness for relatively heavy loaded contacts in combination with piezoviscous lubricant behaviour, it cannot be applied unrestricted. Consequently, the present approach has its limitations. To estimate the region of validity, the boundaries as presented by Koets [77] for Ertel's original analysis are used. In terms of the parameters M and L, these boundaries read:

$$L\sqrt{M} \geq 13.3, \quad M \geq 0.17L^{2/3} \tag{3.41}$$

To use these limitations in the present analysis, they have to be translated to the local conditions. Once the film thickness is determined with eq. (3.38), the local load can be calculated using eq. (3.36), followed by the determination of the local M and L parameter. Then the film thickness can be validated by means of verifying if the local M and L satisfy the relations given in eq. (3.41).

3.2.4 Comparison of the pressure perturbation with numerical work

To check the accuracy of the model, the pressure perturbation due to the deformation of the bump is compared with numerical results from Venner [101]. He calculated the ratio between the maximum pressure in case of the presence of a bump and the maximum pressure in a smooth contact, P_{max}/P_{ms}. The bump was located in the centre of the contact. Further, the problem was considered to be steady state, i.e. only the smooth surface was moving. A typical result is shown in Figure 3.3. In terms of the present parameters p_0 and p_H, the ratio P_{max}/P_{ms} can be expressed as:

$$\frac{P_{max}}{P_{ms}} = \frac{p_0 + p_H}{p_0} \tag{3.42}$$

where according to Hertz:

$$p_H = \frac{2w}{\pi a_l} = \sqrt{\frac{wE'}{2\pi\beta_l}} \tag{3.43}$$

In eq. (3.43) w and β_l are the unknowns. To derive an expression for w, a similar approach is followed as in section 3.2.2. There h_0 was solved from eq. (3.17) and eq. (3.34), where the other unknown in the equations was w. In this case w will be solved by means of substitution of eq. (3.17) into eq. (3.34):

$$\left(h_{sm} - A + \frac{8w}{\pi E'}\right)^{4/3} = 2^{3/2}\pi^{7/6}3^{-11/6}\eta_0 u_d \alpha^* {E'}^{1/6} w^{-1/6} {\beta_l}^{1/2} \tag{3.44}$$

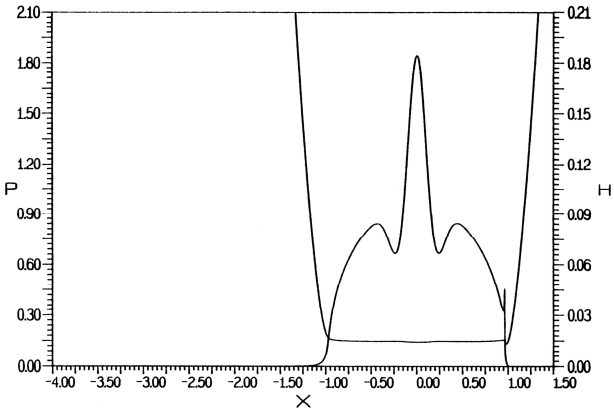

Figure 3.3: Pressure profile and film shape for the 2 GPa load condition in the case of a bump with a wavelength of 0.5 mm and an amplitude of 2 µm at the centre of the contact. P is the dimensionless pressure, H is the dimensionless film thickness and X is the dimensionless coordinate. Reproduced from [101].

Unfortunately this is a rather complicated equation, which does not give much insight. Therefore, a simplified case is investigated.

For the case as shown in Figure 3.3 it seems a reasonable approximation to set h_0 equal to h_{sm}. As a result, eq. (3.17) reduces to:

$$w = \frac{\pi A E'}{8} \tag{3.45}$$

If this equation is substituted into eq. (3.43) the following relation is obtained:

$$p_H = \sqrt{\frac{A E'^2}{16 \beta_l}} \tag{3.46}$$

In eq. (3.46) a second unknown geometry parameter, i.e. the amplitude of the asperity, is introduced. Both unknowns are solved by means of locally fitting the mathematical function as used by Venner [101] to model his bump by a parabolic shape. Venner's bump equation reads:

$$b(x) = A_V \cdot 10^{-10\left(\frac{x-x_d}{\omega}\right)^2} \cos\left(2\pi \frac{x-x_d}{\omega}\right) \tag{3.47}$$

where ω is a measure for the width of the bump. A series expansion around $x = x_d = 0$ yields:

$$b(x) = A_V - 2\frac{A_V(\pi^2 + 5\ln 10)}{\omega^2} x^2 + O\left(x^4\right) \tag{3.48}$$

Given that for a cylindrical asperity $b(x) = A - x^2/(2\beta_l)$, the expression for β_l and A can

readily be derived:

$$A = A_V \tag{3.49}$$

$$\beta_l = \frac{\omega^2}{4(\pi^2+5\ln 10)A_V} \tag{3.50}$$

Substitution of eq. (3.49) and eq. (3.50) into eq. (3.46) gives:

$$p_H = \sqrt{\frac{\pi^2+5\ln 10}{4}}\frac{A_V E'}{\omega} \approx 2.3\frac{A_V E'}{\omega} \tag{3.51}$$

Having this relation, the pressure ratio as a function of A_V and ω for a given E' can be plotted. Venner [101] used in his calculations $E' = 226$ GPa [101, p. 150, Table 7.1] and plotted the ratio for $p_0 = 2$ GPa. The result is shown in Figure 3.4(a). The result of

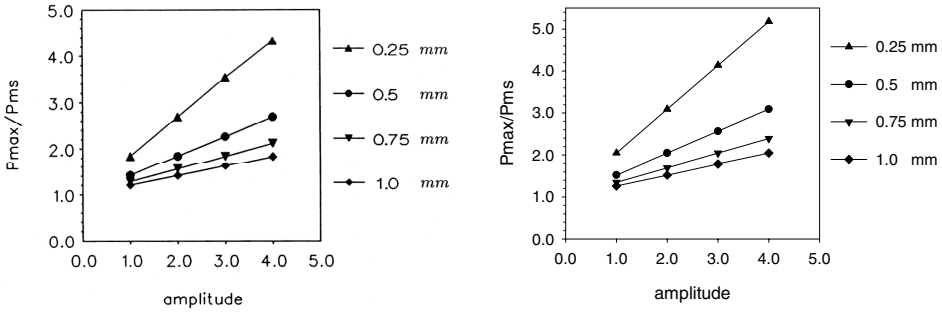

(a) Numerical (b) Analytical

Figure 3.4: Relative maximum pressure as a function of the amplitude for different wavelengths. Figure 3.4(a) is reproduced from [101].

eq. (3.42) and eq. (3.51) is plotted in Figure 3.4(b). The figures show that the analytical and numerical results agree fairly well.

Besides the amplitude and wavelength, Venner [101] also varied the loading condition. A series of calculations with varying wavelength was performed for conditions with maximum pressure of 1, 2 and 3 GPa. The absolute value of the maximum pressure perturbation was plotted against the wavelength. In terms of the present analysis this is equal to plotting the pressure as defined by eq. (3.51) against the wavelength. Both the numerical and analytical results are illustrated in Figure 3.5. The results show good agreement. As stated by Venner, the absolute pressure rise is found to be approximately independent of the loading conditions. Given that $h_0 = h_{sm}$, this is also found in the present model: in eq. (3.51) the parameter p_0 does not play a role.

Figure 3.4 as well as Figure 3.5 show that the pressure perturbations as predicted by the current analysis can be compared very well with numerical predictions as given in Venner [101]. Although strictly valid only for the case $h_0 = h_{sm}$, both analyses indicate that the deformation of the asperity is independent of the surrounding pressure. Therefore, it

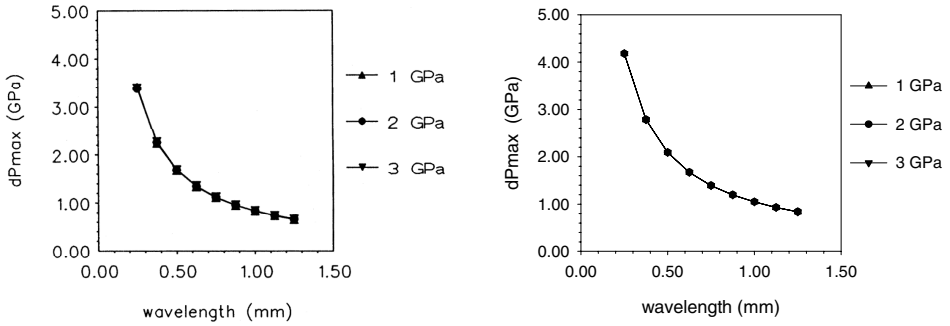

(a) Numerical (b) Analytical

Figure 3.5: Absolute maximum pressure rise as a function of the wavelength for three different load situations. The amplitude is fixed at 2 μm. Figure 3.5(a) is reproduced from [101].

is concluded that assumption 4 in section 3.2.1 can be made safely. Moreover, since the pressure perturbation is linked directly to the deformation, the assumption that the maximum Hertzian deformation equals a_l^2/β_l seems justified as well.

3.2.5 Viscosity dependence

From the micro-EHL model it was found that the lubricant properties play an important role in the film formation. For example, if the Barus relation is chosen, it follows from eq. (3.35) and eq. (3.38) that through α^* the film thickness depends strongly on αp_0. In which way other viscosity-pressure relations affect the film thickness will be discussed next.

Roelands

Although the Barus viscosity-pressure relationship has proven its value in many studies, in particular studies of analytical nature, the validity for practical situations can be limited. As outlined in 2.1.2, at higher pressures the Roelands relation can describe the viscosity-pressure dependence significantly more accurately. Based on eq. (2.10), for isothermal conditions this equation reads:

$$\eta = \eta_0 \exp\left\{\ln\left(\frac{\eta_0}{\eta_\infty}\right)\left[\left(1+\frac{p}{p_c}\right)^z - 1\right]\right\} \tag{3.52}$$

From eq. (3.38) it follows that the viscosity-pressure dependency is included in α^*. To see how α^* is influenced by the inclusion of the Roelands relation instead of the Barus relation, a closer look is given at the calculation of the left hand side of eq. (3.6). Another way to calculate this left hand side is:

$$\int_{p_0}^{\infty} \frac{\eta_0}{\eta(p')} dp' = \frac{e^{-\alpha p_0}}{\alpha} = \frac{1}{\alpha^*} \tag{3.53}$$

This can be seen as a more general way of calculating α^*, see Blok [17]. Substitution of the Roelands relation leads to the following equation for α^*:

$$\frac{1}{\alpha^*} = \int_{p_0}^{\infty} \frac{\eta_0}{\eta(p')} dp' = \frac{p_c}{z} \sigma^{-1/z} e^{\sigma} \Gamma\left(\frac{1}{z}, \sigma\left(1+\frac{p_0}{p_c}\right)^z\right) \tag{3.54}$$

where:

$$\sigma = \ln\left(\frac{\eta_0}{\eta_\infty}\right) \tag{3.55}$$

and Γ represents the incomplete gamma function defined as:

$$\Gamma(a,b) = \int_b^{\infty} e^{-t} t^{a-1} dt \tag{3.56}$$

It is possible to approximate eq. (3.56) for a practical lower and upper boundary z, i.e. $z = 0.5$ and $z = 1$:

$$z = 1: \quad \Gamma(1,b) = \mathrm{e}^{-b} \tag{3.57}$$

$$z = 0.5: \quad \Gamma(2,b) = \mathrm{e}^{-b}(b+1) \tag{3.58}$$

where:

$$b = \sigma\left(1+\frac{p_0}{p_c}\right)^z \tag{3.59}$$

An estimation of the minimum value for b can be given using $p_0 = 0$ and a practical lower boundary for the viscosity at ambient pressure: $\eta_0 = 1$ mPa s. This gives $b > 2.7$. For $0.5 < z < 1$ and $b > 2.7$, eq. (3.57) and eq. (3.58) can be combined to

$$\Gamma\left(\frac{1}{z}, b\right) = \mathrm{e}^{-b}(b+1)^{1/z-1} \tag{3.60}$$

which differs less than 1% from eq. (3.56). Substitution into eq. (3.54) yields:

$$\frac{1}{\alpha^*} = \frac{p_c}{z} \sigma^{-1/z} e^{\sigma} e^{-b} (b+1)^{1/z-1} \tag{3.61}$$

This equation can be used to include the Roelands relation in the new micro-EHL model.

Yasutomi

Where the Barus relation can fail at pressures higher than 0.5 GPa, Roelands on its turn might be less accurate at $p > 1$ GPa. A model which gives better results at these high pressures is the one proposed by Bair and Winer [10], as given in eq. (2.14). Substitution of this model into eq. (3.53) gives:

$$\frac{1}{\alpha^*} = \int_{p_0}^{p_g} \frac{\eta_0}{\eta_g} \mathrm{e}^{f(p')} dp' + \int_{p_g}^{\infty} \frac{\eta_0}{\eta_g} \mathrm{e}^{\{\alpha_g (p_g - p')\}} dp' \tag{3.62}$$

with

$$f(p') = \left\{ 2.3 \frac{C_1 \cdot [T_0 - \{T_g(0) + A_1 \ln(1 + A_2 p')\}] \cdot [1 - B_1 \ln(1 + B_2 p')]}{C_2 + [T_0 - \{T_g(0) + A_1 \ln(1 + A_2 p')\}] \cdot [1 - B_1 \ln(1 + B_2 p')]} \right\} \tag{3.63}$$

where T_0 is a reference temperature, η_0 is the viscosity at *zero* pressure and $p_0 < p_g$. For eq. (3.62) no analytical solution is found. As a consequence the influence of the various lubricant parameters on α^* is not as clear as found for the Barus and the Roelands parameters. However, in case $p_0 \geq p_g$ the first term in eq. (3.62) vanishes, which leads to:

$$\frac{1}{\alpha^*} = \frac{\eta_0}{\alpha_g \eta_g} e^{\alpha_g (p_g - p_0)} \tag{3.64}$$

The product $\eta_0 \alpha^*$

For the Roelands relation α^* is quite generally approximated by the piezoviscosity coefficient at ambient pressure:

$$\alpha_0 = \frac{1}{\eta} \frac{d\eta}{dp}\bigg|_{p=p_a} = \frac{\sigma z}{p_c} \tag{3.65}$$

When this expression is implemented in eq. (3.61), the relation for α^* can also be written as:

$$\alpha^* = \frac{z}{p_c} \sigma^{1/z} e^{-\sigma} e^b (b+1)^{1-1/z} = \alpha_0 \frac{\eta(p_0)}{\eta_0} \left(\frac{b+1}{\sigma} \right)^{1-1/z} \tag{3.66}$$

In eq. (3.38) α^* is always accompanied by η_0. Considering this product, a similarity between Barus, Roelands and Yasutomi at $p_0 > p_g$ can be found:

$$\text{Barus :} \qquad \eta_0 \alpha^* = \eta(p_0)\, \alpha \tag{3.67}$$

$$\text{Roelands :} \qquad \eta_0 \alpha^* = \eta(p_0)\, \alpha_0 \left(\frac{b+1}{\sigma} \right)^{1-1/z} \tag{3.68}$$

$$\text{Yasutomi :} \qquad \eta_0 \alpha^* = \eta(p_0)\, \alpha_g \tag{3.69}$$

From these equations it follows that the product $\eta_0 \alpha^*$ can be replaced by an inlet viscosity at the micro contact $\eta(p_0)$ and the pressure viscosity index at zero pressure, which is for Roelands multiplied by the factor $((b+1)/\sigma)^{1-1/z}$ in order to correct the non-constant pressure viscosity index. From this result the film thickness at the micro contact can also be seen as the Ertel approximation for a macro contact in which a proper value for the inlet viscosity and pressure viscosity index are substituted. Note that for a large p_0 the term $((b+1)/\sigma)^{1-1/z}$ reduces to $(1 + p_0/p_c)^{z-1}$. Then $\alpha_0 (1 + p_0/p_c)^{z-1}$ becomes equal to $1/\eta(p_0)\, d\eta/dp|_{p=p_0}$, i.e. the pressure viscosity index at p_0.

3.2.6 Inlet pressure dependence

From the previous section it was concluded that p_0 has a significant influence on the film thickness, which will now be discussed in more detail. For the conditions belonging

to the case as presented in Figure 3.3, the film thickness under the asperity summit is calculated as a function of the surrounding pressure. The conditions read:

Table 3.1: Operating conditions.

η_0	=	40 mPa s	z	=	0.68
p_c	=	198 MPa	u_d	=	1.94 ms^{-1}
h_{sm}	=	0.256 µm	A	=	0.256 µm
β_l	=	100 µm			

Note that for the radius of curvature a typical value of 100 µm is used instead of the rather large value of 11 mm. For the calculation of α^* eq. (3.66) is used.

Table 3.2: Results for $A = h_{sm} = 0.256$ µm and $\beta_l = 100$ µm.

p_0 [GPa]	h_0/h_{sm} [−]	$p_{H,asp}$ [GPa]
0	0.351	1.69
0.025	0.493	2.01
0.05	0.686	2.37
0.075	0.945	2.78
0.1	1.29	3.25
0.125	1.75	3.78
0.15	2.36	4.39
0.175	3.15	5.08
0.2	4.2	5.86

As can be seen in Table 3.2, at higher values of p_0, unrealistic values for the ratio h_0 over h_{sm} are found; it is very unlikely that $h_0 > h_{sm}$. Moreover, the maximum pressures are unrealistic as well. This somewhat strange behaviour occurs when the inlet viscosity increases. More lubricant will be dragged into the micro contact, which results into a thicker film. Note that this will result into more asperity deformation and consequently into even higher viscosities. As long as the viscosity increases, h_0 will increase as well. For the situation as described above, h_0 already exceeds h_{sm} at an inlet viscosity of about 300 mPa s, which corresponds to a surrounding pressure of only 0.1 GPa.

The reason for the continuing increase of the film thickness is the amount of lubricant available in the micro contact. The current model can be considered as a slightly modified general EHL contact. Such a general EHL contact is described by three equations: the Reynolds equation, film thickness equation and force balance equation. The difference between the general model and the current micro-EHL model is that in the micro-EHL model the force balance equation is replaced by a relation which fixes the integration constant in the film thickness equation. Consequently, changes in film thickness will result into exactly the same amount of elastic deformation of the asperity. The bulk of

the asperity however, stays at a fixed level. This level is directly related to h_{sm}, which gives the coupling between the asperity and the smooth film thickness. So the shape of the macro contact is not taken into account directly by means of, for instance, a specific non-parabolic shape of the asperity, but more or less indirectly by means of a fixed height of the bulk of the asperity.

Since the shape of the macro contact is not modelled in a direct way, the micro-contact is assumed to be fully flooded. This means that the amount of lubricant available in the inlet is unlimited. Depending on the viscosity, the film thickness then can rise to extremely high values, which explains the result as presented in Table 3.2. If the macro contact shape is taken into account, the amount of lubricant will be more or less limited to a layer of thickness h_{sm}. In other words, the micro contact turns into some sort of starved contact. As a result, the film thickness will never exceed h_{sm}, simply because there is not more lubricant available. Many studies, numerical as well as experimental, indeed show that in the Hertzian contact zone the deformation of asperity never significantly surpasses the surrounding film thickness.

As long as the film thickness generated under the asperity summit is small compared to the smooth film thickness, the differences between a fully flooded contact and a "starved" contact may be not very large. The work of Wijnant [112] on starved point contacts shows that a lubricant layer larger than four times the central film thickness virtually gives the same result as a fully flooded contact [112, sec. 7.1]. Moreover, Wijnant shows that in case the inlet lubricant layer is smaller than the fully flooded film thickness, the film thickness converges to the inlet lubricant layer. The observations are supported by Chevalier et al. [20].

3.2.7 Modification

From the previous paragraphs it was concluded that h_0 has to be limited to h_{sm}. Similar to starved lubrication, limitation of the lubricant available in the micro inlet can lead to the desired result. To implement this in the current micro-EHL model, the pressure necessary for the asperity deformation is set to *zero* in the region where $h_0 + h_l > h_{sm}$, see Figure 3.1. Following the approach as presented in section 3.2.2, eq. (3.26) changes into:

$$\int_{\bar{q}(\bar{x}=-\bar{x}_{st})}^{\bar{q}(\bar{x}=-1)} d\bar{q} = \mathcal{L} \int_{-\bar{x}_{st}}^{-1} \frac{\bar{h}_l}{(\bar{h}_l + \bar{h}_0)^3} d\bar{x} \tag{3.70}$$

where $-\bar{x}_{st}$ is the point where the pressure build up starts. Combining $h_0 + h_l = h_{sm}$ with eq. (3.24) gives for $\bar{x}_{st}$:

$$\bar{x}_{st} = \left[\frac{3}{2\sqrt{2}} \left(\bar{h}_{sm} - \bar{h}_0 \right) \right]^{2/3} + 1 \tag{3.71}$$

Since $\bar{q}(\bar{x}=-\bar{x}_{st}) = 0$, the left hand side of eq. (3.71) is exactly the same as its equivalent in eq. (3.26). As a result, the definition of α^* is not affected by the "starved" approach.

As for the right hand side, only the integration boundary changes. Eq. (3.28) becomes:

$$\mathcal{L}\int_{1}^{\bar{y}_{st}} \frac{\tilde{h}_l}{(\tilde{h}_l-\bar{h}_0)^3}d\bar{y} \tag{3.72}$$

with $\tilde{h}_l$ defined by eq. (3.29) and $\bar{y}_{st}$ according to:

$$\bar{y}_{st} = \left[\frac{3}{2\sqrt{2}}\left(\bar{h}_{sm}-\bar{h}_0\right)\right]^{2/3}+1 \tag{3.73}$$

Substitution of the transformation given by eq. (3.30) yields for the right hand side:

$$\frac{2\mathcal{L}}{\bar{h}_0^2}\left(\frac{3\bar{h}_0}{2\sqrt{2}}\right)^{2/3}\int_{0}^{z_{st}} \frac{z^4}{(z^3+1)^3}dz \tag{3.74}$$

with

$$z_{st} = \left(\frac{\bar{h}_{sm}}{\bar{h}_0}-1\right)^{1/3} \tag{3.75}$$

Unfortunately, the solution of eq. (3.74) results into a rather complicated expression:

$$\begin{aligned}&\frac{2\mathcal{L}}{\bar{h}_0^2}\left(\frac{3\bar{h}_0}{2\sqrt{2}}\right)^{2/3}\int_{0}^{z_{st}} \frac{z^4}{(z^3+1)^3}dz = \\ &\mathcal{L}\bar{h}_0^{-4/3}3^{2/3}\left\{\frac{{z_{st}}^2(2{z_{st}}^3-1)}{18(1+{z_{st}}^3)^2}+\frac{1}{54}\ln\left(\frac{1+{z_{st}}^3}{(1+z_{st})^3}\right)+\frac{1}{9\sqrt{3}}\arctan\left(\frac{2z_{st}-1}{\sqrt{3}}\right)\right\}\end{aligned} \tag{3.76}$$

A simplified equation can be obtained if eq. (3.74) is approximated using the asymptotes for $\bar{h}_0/\bar{h}_{sm}\to 0$ and $\bar{h}_0/\bar{h}_{sm}\to 1$. Obviously the first asymptote, denoted as A_1, is equal to eq. (3.32). The second asymptote, referred to as A_2, is obtained by means of a first order series expansion around $z_{st}=0$:

$$\mathsf{A}_2 = \mathcal{L}\frac{3^{2/3}}{5}\bar{h}_0^{-4/3}z_{st}^5 = \mathcal{L}\frac{3^{2/3}}{5}\bar{h}_0^{-4/3}\left(\frac{\bar{h}_{sm}}{\bar{h}_0}-1\right)^{5/3} \tag{3.77}$$

When combining both asymptotes, the approximation reads (deviation less than 3%):

$$\begin{aligned}&\frac{2\mathcal{L}}{\bar{h}_0^2}\left(\frac{3\bar{h}_0}{2\sqrt{2}}\right)^{2/3}\int_{0}^{z_{st}} \frac{z^4}{(z^3+1)^3}dz \approx \\ &\left(\mathsf{A}_1^{-9/14}+\mathsf{A}_2^{-9/14}\right)^{-14/9} = \mathsf{A}_1\left(1+\left(\frac{\mathsf{A}_2}{\mathsf{A}_1}\right)^{-9/14}\right)^{-14/9} = \\ &2\pi 3^{-17/6}\bar{h}_0^{-4/3}\mathcal{L}\left[1+\left(\frac{27\sqrt{3}}{10\pi}\right)^{-9/14}\left(\frac{\bar{h}_{sm}}{\bar{h}_0}-1\right)^{-15/14}\right]^{-14/9}\end{aligned} \tag{3.78}$$

Substitution of eq. (3.27) and eq. (3.78) in eq. (3.70), followed by elimination of w using eq. (3.17) yields for the "starved" film thickness:

$$h_0 f_l \left(1+\frac{\mathcal{A}}{h_0}\right)^{\frac{1}{9}} = C_l(\eta_0\alpha^* u_d)^{2/3}\beta_l{}^{1/3} \tag{3.79}$$

where:

$$\mathcal{A} = A - h_{sm} \tag{3.80}$$

$$C_l = \pi^{2/3}2^{4/3}3^{-11/9} \tag{3.81}$$

$$f_l = \left[1+\left(\frac{27\sqrt{3}}{10\pi}\right)^{-9/14}\left(\frac{h_{sm}}{h_0}-1\right)^{-15/14}\right]^{28/27} \tag{3.82}$$

This equation is basically the same as eq. (3.38). Only when h_0 approaches h_{sm}, the film thickness is limited to h_{sm} by the factor f_l.

3.2.8 Comparison of the film thickness with numerical work

To compare the results as derived in the previous section with numerical work, a simple and straightforward solver is built for line contact. To test the accuracy of the new solver, for typical smooth contact EHL conditions it is compared with the solver as developed by Venner [101], which is known to produce valid results. For $M = 100.0$ and $L = 11.1$ a comparison is illustrated in Figure 3.6. Another comparison for a lightly loaded contact

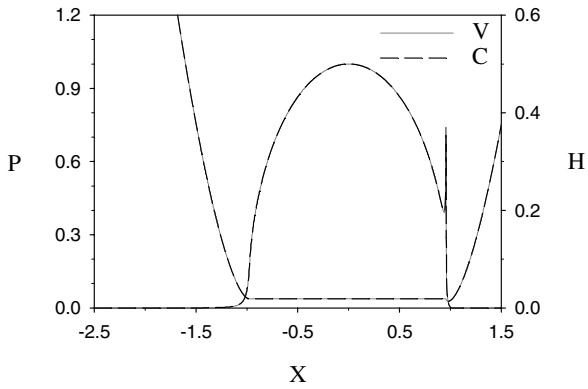

Figure 3.6: Comparison between solver as developed by Venner [101], indicated by V, and current solver, indicated by C. $M = 100.0$, $L = 11.1$

($M = 6.3$ and $L = 11.1$) is shown in Figure 3.7. Although the solver in terms of speed is less efficient than Venner's solver, the results are found to be nearly identical, which proves the validity of the current solver. The "starved" approach is implemented in two steps. First, the force balance equation is replaced by fixing the integration constant in

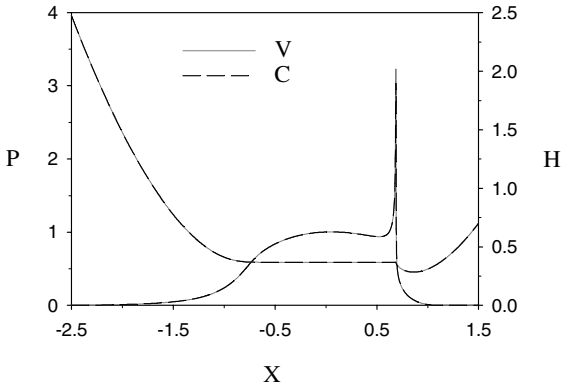

Figure 3.7: Comparison between solver as developed by Venner [101], indicated by V, and current solver, indicated by C. $M = 6.3, \quad L = 11.1$

the film thickness equation. Secondly, in the inlet region the pressure is set to *zero* if the film thickness is higher than h_{sm}. The result of both eq. (3.38) and eq. (3.79) as well as the numerical calculation is plotted in Figure 3.8. The conditions are the same as those given in Table 3.1. When the two analytical models are compared, it is observed that even at the smallest values for p_0 the starved approach reduces the film thickness. This is because the ratio h_0 over h_{sm} is not sufficiently small to limit f_l to 1. On the other hand, the numerical results agree reasonably well with those of the starved analytical model, which the numerical model was intended to simulate.

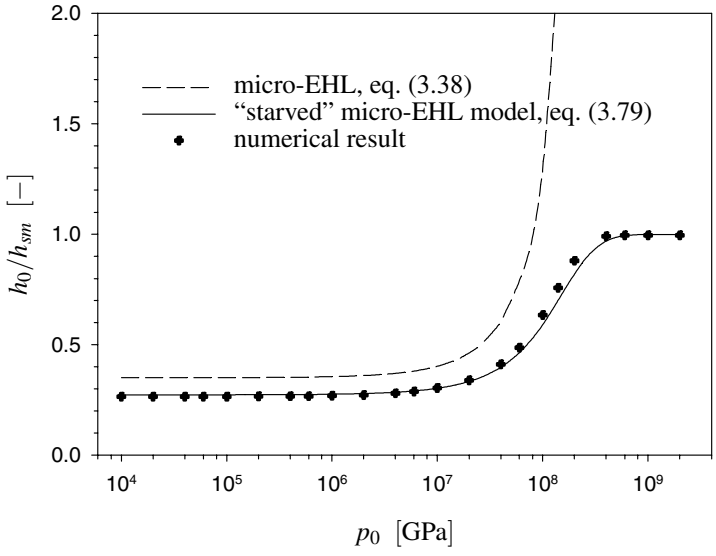

Figure 3.8: Comparison between the analytical models and numerical results

3.3 The micro-EHL circular contact model (3D asperity)

In the previous sections the new micro-EHL model was developed for the line contact situation. With respect to practical applications, a logical step is to extend the model to spherical asperities. Since Ertel's solution, on which the line contact model was based, can also be applied to circular contacts, see section 2.2.1, a similar approach as used in the line contact model is followed.

3.3.1 Equations

For the axi-symmetric case the picture shown in Figure 3.2 does not change much, as illustrated in Figure 3.9. The coordinate x turns into the radial coordinate r, a_s and β_s represent the radius of the Hertzian contact circle and the summit radius of curvature respectively. The relation between the film thickness under the asperity summit, the

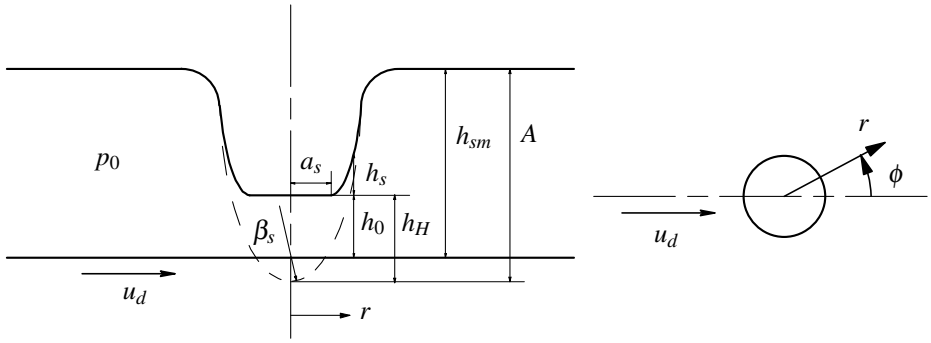

Figure 3.9: Micro-EHL for axi-symmetric asperity, side view and top view

maximum asperity deformation and the amplitude of the bump is given by:

$$h_0 = h_{sm} - A + h_H \tag{3.83}$$

which obviously does not differ from eq. (3.13). In line contact the maximum Hertzian deformation appeared to be undefined and an assumption on its value had to be made. In point contact however, this deformation is known and defined as Hertz [58]:

$$h_H = \frac{a_s^2}{\beta_s} \tag{3.84}$$

With

$$a_s = \left(\frac{3F\beta_s}{2E'} \right)^{1/3} \tag{3.85}$$

in which F is the load, the maximum deformation reads:

$$h_H = \frac{1}{\beta_s}\left(\frac{3F\beta_s}{2E'}\right)^{2/3} \tag{3.86}$$

As a result, the axi-symmetric equivalent of eq. (3.17) reads:

$$h_0 = h_{sm} - A + \frac{1}{\beta_s}\left(\frac{3F\beta_s}{2E'}\right)^{2/3} \tag{3.87}$$

The second relation between h_0 and F is deduced from the Reynolds equation in polar coordinates:

$$\frac{\partial}{\partial\phi}\left(\frac{h^3}{12\eta}\frac{1}{r^2}\frac{\partial p}{\partial\phi}\right) + \frac{1}{r}\frac{\partial}{\partial r}\left(\frac{h^3}{12\eta}r\frac{\partial p}{\partial r}\right) = \frac{\partial}{\partial\phi}(h\omega) + \frac{1}{r}\frac{\partial}{\partial r}(rhu_r) \tag{3.88}$$

where:

$$\omega = -u_d\frac{\sin\phi}{2r} \tag{3.89}$$

$$u_r = u_d\frac{\cos\phi}{2} \tag{3.90}$$

Since an axi-symmetric system is studied, all derivatives of h and p with respect to ϕ are *zero*. Note that this assumption cannot be applied to the velocities. As a result, eq. (3.88) is reduced to:

$$\frac{1}{r}\frac{\partial}{\partial r}\left(\frac{h^3}{12\eta}r\frac{\partial p}{\partial r}\right) = h\frac{\partial\omega}{\partial\phi} + \frac{1}{r}\frac{\partial}{\partial r}(rhu_r) \tag{3.91}$$

Using eqs. (3.89) and (3.90), eq. (3.91) can also be written as:

$$\frac{\partial}{\partial r}\left(\frac{h^3}{12\eta}r\frac{\partial p}{\partial r}\right) = u_r r\frac{\partial h}{\partial r} \tag{3.92}$$

Integrating once gives:

$$\frac{h^3}{12\eta}r\frac{\partial p}{\partial r} = u_r\left(rh - \int h\,dr + C\right) \tag{3.93}$$

Introduction of the isoviscous pressure gives:

$$\frac{\partial q}{\partial r} = 12\eta_0 u_r\frac{rh - \int h\,dr + C}{rh^3} \tag{3.94}$$

Somewhere in the Hertzian contact zone, there will be a point at which $\partial q/\partial r = 0$ and $h = h_0$. This leads to:

$$\frac{\partial q}{\partial r} = 12\eta_0 u_r\frac{r(h-h_0) - \int h\,dr + \int h\,dr|_{h=h_0}}{rh^3} \tag{3.95}$$

Conform to Ertel's approach, the deformation of the asperity is assumed to follow Hertzian dry contact shape, viz. $h = h_0 + h_s$, so that:

$$\frac{\partial q}{\partial r} = 12\eta_0 u_r \frac{r h_s - \int (h_s + h_0)\, dr + \int (h_s + h_0)\, dr|_{h_s=0}}{r(h_s + h_0)^3} \tag{3.96}$$

where:

$$h_s(r) = 0\,, \qquad r < a_s \tag{3.97}$$

$$h_s(r) = \frac{1}{\pi\beta_s}\left[a_s\sqrt{r^2 - a_s^2} - \left(2a_s^2 - r^2\right)\arctan\left(\sqrt{\left(\frac{r}{a_s}\right)^2 - 1}\right)\right], \quad r \geq a_s \tag{3.98}$$

Using the Hertzian circular contact dimensions and the pressure viscosity index, the following dimensionless parameters are introduced:

$$r = \hat{r}\bar{r} = a_s\bar{r}, \quad h = \hat{h}\bar{h} = \frac{a_s^2}{\beta_s}\bar{h}, \quad q = \hat{q}\bar{q} = \frac{1}{\alpha}\bar{q} \tag{3.99}$$

Substitution of these parameters and using Crook's method to approximate the Hertzian gap outside the loaded zone yields for eqs. (3.96) to (3.98):

$$\frac{\partial \bar{q}}{\partial \bar{r}} = \mathcal{S}\frac{\bar{r}\bar{h}_s - \int (\bar{h}_s + \bar{h}_0)\, d\bar{r} + \int (\bar{h}_s + \bar{h}_0)\, d\bar{r}\big|_{\bar{h}_s=0}}{\bar{r}(\bar{h}_s + \bar{h}_0)^3} \tag{3.100}$$

where:

$$\bar{h}_s(\bar{r}) = 0, \qquad \bar{r} < 1 \tag{3.101}$$

$$\bar{h}_s(\bar{r}) = \frac{8\sqrt{2}}{3\pi}(\bar{r} - 1)^{3/2}\,, \qquad \bar{r} \geq 1 \tag{3.102}$$

$$\mathcal{S} = 12\eta_0 u_r \frac{\hat{r}}{\hat{q}\hat{h}^2} = 8\eta_0 \alpha u_r E' \beta_s F^{-1} \tag{3.103}$$

At this point, the first integral in the numerator in the right hand side of eq. (3.100) can be worked out analytically:

$$-\int (\bar{h}_s + \bar{h}_0) d\bar{r} = -\frac{16\sqrt{2}}{\pi 15}(\bar{r} - 1)^{5/2} - \bar{r}\bar{h}_0 = -\frac{2}{5}(\bar{r} - 1)\bar{h}_s - \bar{r}\bar{h}_0 \tag{3.104}$$

Regarding this result, the second integral simply reads $+\bar{r}\bar{h}_0$. Substitution of both integrals into eq. (3.100) gives:

$$\frac{\partial \bar{q}}{\partial \bar{r}} = \mathcal{S}\frac{\frac{3}{5}\bar{r}\bar{h}_s + \frac{2}{5}\bar{h}_s}{\bar{r}(\bar{h}_s + \bar{h}_0)^3} \tag{3.105}$$

Eq. (3.105) has to be integrated once more along the centre line of the contact, i.e. $\phi = \pi$. This also leads to $u_r \overset{\phi=\pi}{=} -u_d/2$. Simultaneously, the starved approach is implemented.

For that, the upper integration boundary for the right hand side has to determined. From eq. (3.102) follows:

$$\bar{r}_{st} = \left[\frac{3\pi}{8\sqrt{2}}(\bar{h}_{sm} - \bar{h}_0)\right]^{2/3} + 1 \tag{3.106}$$

Adding the integration boundaries to eq. (3.105) results into:

$$\int_{\bar{q}(\bar{r}=1)}^{\bar{q}(\bar{r}=\bar{r}_{st})} d\bar{q} = \int_{1}^{\bar{r}_{st}} \mathcal{S}\frac{\frac{3}{5}\bar{r}\bar{h}_s + \frac{2}{5}\bar{h}_s}{\bar{r}(\bar{h}_s + \bar{h}_0)^3} d\bar{r} \tag{3.107}$$

with

$$\mathcal{S} = -4\eta_0\alpha u_d E' \beta_s F^{-1} \tag{3.108}$$

Apart from the sign, the left hand side is the same as its line contact counterpart in eq. (3.27):

$$\int_{\bar{q}(\bar{r}=1)}^{\bar{q}(\bar{r}=\bar{r}_{st})} d\bar{q} = -\mathrm{e}^{-\alpha p_0} \tag{3.109}$$

The right hand side however, results into a quite complicated expression. A simpler expression can be obtained using the assumption that the integral is determined mainly in the region around $\bar{r} = 1$. As a result, $\frac{2}{5}\bar{h}_s$ can be replaced by $\frac{2}{5}\bar{r}\bar{h}_s$. Hence, the right hand side reduces to:

$$\int_{\bar{r}=1}^{\bar{r}=\bar{r}_{st}} \mathcal{S}\frac{\bar{h}_s}{(\bar{h}_s + \bar{h}_0)^3} d\bar{r} \tag{3.110}$$

Eq. (3.110) shows large similarities with eq. (3.72). For this reason, the way to solve eq. (3.108) will be the same as used in section 3.2.7. First, the following transformation is applied:

$$z^3 = \frac{\bar{h}_s}{\bar{h}_0} = \frac{8\sqrt{2}}{3\pi\bar{h}_0}(\bar{r} - 1)^{3/2}, \quad d\bar{r} = 2\left(\frac{3\pi\bar{h}_0}{8\sqrt{2}}\right)^{2/3} z dz \tag{3.111}$$

Substitution gives:

$$\frac{2\mathcal{S}}{\bar{h}_0^2}\left(\frac{3\pi\bar{h}_0}{8\sqrt{2}}\right)^{2/3} \int_0^{z_{st}} \frac{z^4}{(z^3+1)^3} dz \tag{3.112}$$

with z_{st} given by eq. (3.75). The (still) rather complicated solution is simplified further using the asymptotes for $\bar{h}_0/\bar{h}_{sm} \to 0$ and $\bar{h}_0/\bar{h}_{sm} \to 1$. The first asymptote reads:

$$\mathsf{A}_1 = \frac{2\mathcal{S}}{\bar{h}_0^2}\left(\frac{3\pi\bar{h}_0}{8\sqrt{2}}\right)^{2/3} 2\pi 3^{-7/2} = 2^{-1/3}3^{-17/6}\pi^{5/3}\mathcal{S}\bar{h}_0^{-4/3} \tag{3.113}$$

Note that from this asymptote, the solution for point contacts as used in the work of Nijenbanning et al. [88] can be derived:

$$h_0 = 2^{7/12}3^{-35/24}\pi^{5/4}(\eta_0\alpha^* u_d)^{3/4}\beta_s^{5/12}E'^{1/12}F^{-1/12} \tag{3.114}$$

Based on a first order series expansion around $z_{st} = 0$ the second asymptote reads:

$$\mathsf{A}_2 = \frac{2^{-4/3}3^{2/3}\pi^{2/3}}{5}\mathcal{S}\bar{h}_0^{-4/3}\left(\frac{\bar{h}_{sm}}{\bar{h}_0} - 1\right)^{5/3} \tag{3.115}$$

Combination of both asymptotes leads to (deviation less than 3%):

$$\begin{aligned}\frac{2\mathcal{S}}{\bar{h}_0^2}\left(\frac{3\pi\bar{h}_0}{8\sqrt{2}}\right)^{2/3}\int_0^{z_{st}}\frac{z^4}{(z^3+1)^3}dz \approx \\ \left(\mathsf{A}_1^{-9/14} + \mathsf{A}_2^{-9/14}\right)^{-14/9} = \mathsf{A}_1\left(1 + \left(\frac{\mathsf{A}_2}{\mathsf{A}_1}\right)^{-9/14}\right)^{-14/9} = \\ 2^{-1/3}3^{-17/6}\pi^{5/3}\bar{h}_0^{-4/3}\mathcal{S}\left[1 + \left(\frac{27\sqrt{3}}{10\pi}\right)^{-9/14}\left(\frac{\bar{h}_{sm}}{\bar{h}_0} - 1\right)^{-15/14}\right]^{-14/9}\end{aligned} \tag{3.116}$$

Finally, substitution of eq. (3.109) and eq. (3.116) in eq. (3.107), followed by elimination of F using eq. (3.87) yields for film thickness under a spherical asperity:

$$h_0 f_s\left(1 + \frac{\mathcal{A}}{h_0}\right)^{\frac{1}{9}} = C_s(\eta_0\alpha^* u_d)^{2/3}{\beta_s}^{1/3} \tag{3.117}$$

where:

$$\mathcal{A} = A - h_{sm} \tag{3.118}$$

$$C_s = \pi^{10/9}2^{4/9}3^{-11/9} \tag{3.119}$$

$$f_s = \left[1 + \left(\frac{27\sqrt{3}}{10\pi}\right)^{-9/14}\left(\frac{h_{sm}}{h_0} - 1\right)^{-15/14}\right]^{28/27} \tag{3.120}$$

As can be seen, the resemblance between the equations for line and point contact is large. Apart from the constants C_l and C_s, they are exactly the same. This means that the same principles determine the line contact film thickness and the centre line film thickness in point contact. Many numerical studies support this, see for instance Hooke [60] and Holmes et al. [59], which state that the centre line film thickness can be approximated well by a line contact analysis. Hooke and Venner [63] also point out that the deformation of sinusoidal waviness in both line and point contact have the same underlying behaviour.

3.4 Summary

A new micro-EHL model to predict the film thickness at the summit of cylindrical shaped as well as spherical shaped asperities has been derived. The model is based on the general EHL contact solution according to Ertel [33] in which the force balance equation is

replaced by fixing the bulk of the asperity at a certain level depending on the overall film thickness. When highly viscous lubricant is present in the asperity inlet, the model takes into account the amount of lubricant available in the macroscopic Hertzian zone. This limits the maximum deformation of the asperity and thus the film thickness and pressure perturbation.

The equations for line and point contact show great similarities. In both cases the lubricant properties are dominant in the film thickness formula. However, it must be noted that indirectly the properties are determined by the surrounding pressure. With respect to the asperity geometry as used in this analysis, the amplitude is of minor importance and the curvature has only a limited influence. The modulus of elasticity has no effect at all on the film thickness. Changes in the sliding velocity however, affect the film thickness more than changes in asperity geometry.

Chapter 4

Asperity characterized by amplitude and slope

In the previous chapter only asperities given by an amplitude and a radius of curvature are discussed. However, depending on the manufacturing process, asperities may look different. For instance, hard turning can give a surface which is similar to the one indicated schematically in Figure 4.1. For this type of surface a parabolic shaped asperity might

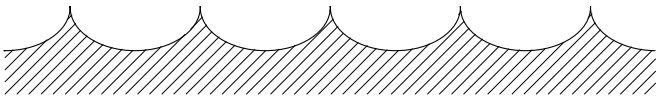

Figure 4.1: Schematic representation of a surface after hard turning

not be the proper representation of a real asperity. This chapter deals with the effects of such a non-parabolic shape on the film formation behaviour. The particular parameters describing the asperity discussed here are an amplitude and a slope. For the 2D case this comes down to a wedge shaped asperity, whereas in point contact a conical shaped asperity is considered. The advantage of this shape is that it can be linked to known numbers, such as various slope parameters which are often used when characterizing surface roughness. Also the well-known plasticity index by Greenwood and Williamson [50] contains a slope related parameter.

In the next section the film thickness under a wedge shaped asperity will be derived. A conical shaped asperity will be examined in 4.2.

4.1 Wedge shaped asperity

Figure 4.2 shows the model of the wedge shaped asperity in contact schematically. The

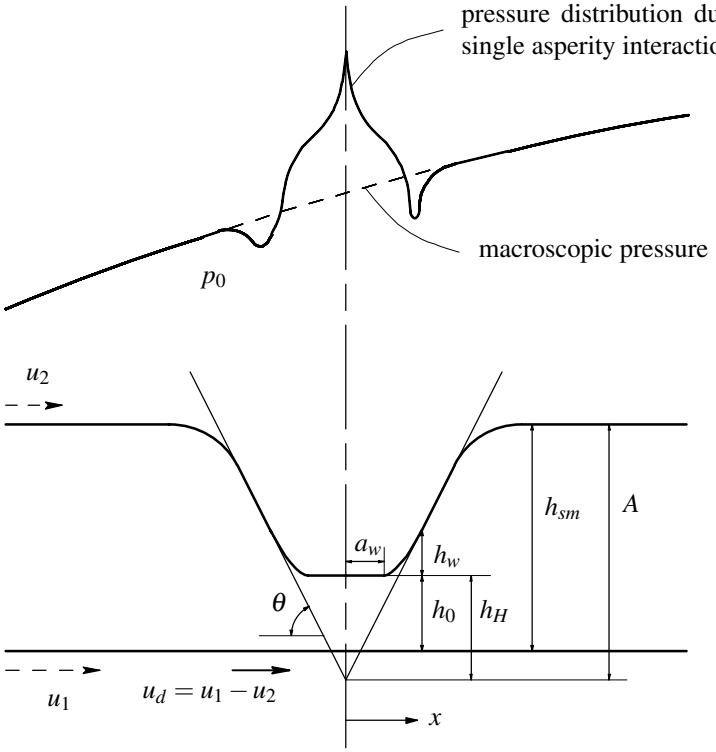

Figure 4.2: Micro-EHL model, wedge shaped asperity

pressure distribution is given by Johnson [70]:

$$p(x) = \frac{E' s_w}{2\pi} \operatorname{arccosh} \left| \frac{a_w}{x} \right| \tag{4.1}$$

where $s_w = \tan\theta$ is the slope of the wedge and $a_w = (2w)/(E' s_w)$ is half the dry contact width [70]. Theoretically, at the asperity tip the pressure rises to an infinite value. Fortunately this has no consequences for the present model, since it is an inlet based analysis. In practical applications however, it can be of importance with respect to fatigue. Sharp asperity tips should be avoided in any case.

The derivation starts with the relation between the central film thickness under the asperity tip, the smooth film thickness, the amplitude of the asperity and the deformation at the summit:

$$h_0 = h_{sm} - A + h_H \tag{4.2}$$

Since a line contact is considered, a similar complication as described in section 3.2.2 is found, namely the term h_H is undefined. Fortunately for the conical case, it is known and defined as $a_n s_n \pi/2$, where a_n is the dry contact radius and s_n is the slope of the cone,

see appendix B. Analogous to the method used in the cylindrical case, the characteristic deformation of a wedge is approximated by:

$$h_H = \frac{\pi}{2} a_w s_w \tag{4.3}$$

Substitution of eq. (4.3) and a_w in eq. (4.2) leads to:

$$h_0 = h_{sm} - A + \frac{\pi w}{E'} \tag{4.4}$$

which is the first relation between w and h_0. The second relation which is needed to solve h_0 follows from Ertel's solution of the Reynolds equation for line contact. Integration of eq. (3.18) with boundary condition $h = h_0$ at $dp/dx = 0$, followed by the introduction of the isoviscous pressure $q = (1 - e^{-\alpha p})/\alpha$ and substitution of Crook's method of approximating the dry contact gap geometry, results into:

$$\frac{dq}{dx} = 6\eta_0 u_d \frac{h_w}{(h_w + h_0)^3} \tag{4.5}$$

$$h(x) = h_0\,, \qquad |x| < a_w \tag{4.6}$$

$$h(x) = h_0 + h_w(x) = h_0 + \frac{4\sqrt{2} s_w}{3\pi\sqrt{a_w}} (|x| - a_w)^{3/2}\,, \quad |x| \geq a_w \tag{4.7}$$

For more details on the derivation of eq. (4.7), the reader is referred to appendix A. Next, the following dimensionless parameters are introduced:

$$x = \hat{x}\bar{x} = a_w \bar{x}, \quad h = \hat{h}\bar{h} = \frac{2}{\pi} a_w s_w \bar{h}, \quad q = \hat{q}\bar{q} = \frac{1}{\alpha}\bar{q} \tag{4.8}$$

As a result, eq. (4.5) to eq. (4.7) change into:

$$\frac{d\bar{q}}{d\bar{x}} = \mathcal{W} \frac{\bar{h}_w}{(\bar{h}_w + \bar{h}_0)^3} \tag{4.9}$$

with

$$\bar{h}_w = 0\,, \qquad |\bar{x}| < 1 \tag{4.10}$$

$$\bar{h}_w = \frac{2\sqrt{2}}{3} (|\bar{x}| - 1)^{3/2}\,, \qquad |\bar{x}| \geq 1 \tag{4.11}$$

$$\mathcal{W} = 6 u_d \eta_0 \frac{\hat{x}}{\hat{q}\hat{h}^2} = \frac{3\pi^2 \eta_0 \alpha u_d E'}{4 w s_w} \tag{4.12}$$

Integration of eq. (4.9) with the boundaries for the starved approach ($p = p_0$ at $\bar{x} = -\bar{x}_{st}$, where $-\bar{x}_{st}$ is the point where $\bar{h} = \bar{h}_{sm}$) gives:

$$\int_{\bar{q}(\bar{x}=-\bar{x}_{st})}^{\bar{q}(\bar{x}=-1)} d\bar{q} = \mathcal{W} \int_{-\bar{x}_{st}}^{-1} \frac{\bar{h}_w}{(\bar{h}_w + \bar{h}_0)^3} d\bar{x} \tag{4.13}$$

where:

$$\bar{x}_{st} = \left[\frac{3}{2\sqrt{2}}\left(\bar{h}_{sm} - \bar{h}_0\right)\right]^{2/3} + 1 \tag{4.14}$$

Since $\bar{h}_w = \bar{h}_l$ (see eq. (3.24)), eq. (4.13) and eq. (4.14) are basically the same as eq. (3.70) and eq. (3.71), only the constants $\mathcal{L}$ and $\mathcal{W}$ differ. Consequently, the solution as presented in section 3.2.7 can readily be used here. Following this approach, with eq. (3.27), eq. (3.78) and $\mathcal{W}$ instead of $\mathcal{L}$, eq. (4.13) becomes:

$$\mathrm{e}^{-\alpha p_0} = 2\pi 3^{-17/6}\bar{h}_0^{-4/3}\mathcal{W}\left[1 + \left(\frac{27\sqrt{3}}{10\pi}\right)^{-9/14}\left(\frac{\bar{h}_{sm}}{\bar{h}_0} - 1\right)^{-15/14}\right]^{-14/9} \tag{4.15}$$

Elimination of w using eq. (4.4) and rearranging finally gives:

$$h_0 f_w \left(1 + \frac{\mathcal{A}}{h_0}\right)^{-1/3} = C_w(\eta_0 u_d \alpha^*){s_w}^{-1} \tag{4.16}$$

where:

$$\mathcal{A} = A - h_{sm} \tag{4.17}$$

$$C_w = \pi^{4/3}2^{5/3}3^{-11/6} \tag{4.18}$$

$$f_w = \left[1 + \left(\frac{27\sqrt{3}}{10\pi}\right)^{-9/14}\left(\frac{h_{sm}}{h_0} - 1\right)^{-15/14}\right]^{14/9} \tag{4.19}$$

Eq. (4.16) gives the film thickness under a wedge shaped asperity as a function of the asperity geometry and the operating conditions. As observed before, the lubricant properties are of great importance for the film build up. Compared to asperities characterized by a radius of curvature, the geometry plays a larger role. When regarding the slope, a steeper edge leads to a smaller film. The amplitude shows an unexpected behaviour. A larger amplitude, which also can be seen as an increase in load, will produce a thicker film. Similar behaviour is observed if the Ertel film thickness solution as presented in section 3.1.1 is applied to a wedge shaped geometry. This film thickness is determined from eq. (4.15) with $\bar{h}_{sm} \to \infty$ and $p_0 = 0$:

$$h_0 = \frac{2^{5/4}\pi^{5/4}}{3^{11/8}} \frac{\alpha^{3/4}{\eta_0}^{3/4}{u_d}^{3/4}w^{1/4}}{{s_w}^{3/4}{E'}^{1/4}} \tag{4.20}$$

The behaviour is caused by the change in the shape of the micro-inlet as the deformation increases. To illustrate this, the Crook's approximation of the gap as given in eq. (4.7) is written slightly different:

$$\begin{aligned} h_w &= a_w s_w \frac{4\sqrt{2}}{3\pi}\left(\left|\frac{x}{a_w}\right| - 1\right)^{3/2} \\ &= s_w\sqrt{\frac{s_w E'}{2w}}\frac{4\sqrt{2}}{3\pi}\left(|x| - a_w\right)^{3/2}, \qquad |x| \geq a_w \end{aligned} \tag{4.21}$$

As the load increases, which means more deformation, the inlet geometry changes such that it becomes more narrow. From lubrication theory it is known that a less fast converging inlet leads to better lubricating properties, see for instance the film thickness solution for a rigid isoviscous line contact in which a larger radius of curvature gives a thicker film. Note that in case of a cylindrical asperity, see eq. (3.11), the inlet geometry reads:

$$\begin{aligned} h_l &= \frac{\sqrt{a_l}}{\beta_l}\frac{2\sqrt{2}}{3}\left(|x|-a_l\right)^{3/2} \\ &= \frac{(8w)^{1/4}}{(\pi E'\beta_l^3)^{1/4}}\frac{2\sqrt{2}}{3}\left(|x|-a_l\right)^{3/2}, \qquad |x| \geq a_l \end{aligned} \tag{4.22}$$

which shows the opposite behaviour with respect to w. Hence, an increase in amplitude, or a higher load, will give thinner films.

4.2 Conical shaped asperity

Similar to the previous chapter, for asperities characterized by a slope and an amplitude, the line contact situation is extended to the point contact situation, i.e. from a wedge shaped asperity to a conical shaped asperity. The approach which is followed is basically the same as the one presented in section 3.3. First, the film thickness is related to the deformation of the asperity (see Figure 4.3):

$$h_0 = h_{sm} - A + h_H \tag{4.23}$$

where $s_n = \tan\theta$ is the slope of the cone, $a_n = \sqrt{(4F)/(\pi s_n E')}$ is the dry contact radius

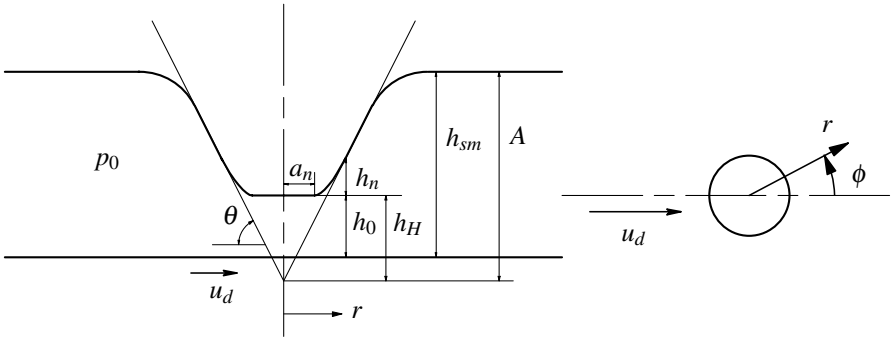

Figure 4.3: Micro-EHL model for conical asperity, side view and top view

(Johnson [70, ch. 5]) and $h_H = a_n s_n \pi/2$ is the maximum deformation at the summit (see appendix B). With h_H and a_n substituted, eq. (4.23) changes into:

$$h_0 = h_{sm} - A + \sqrt{\frac{\pi s_n F}{E'}} \tag{4.24}$$

The next step is to solve the Reynolds equation, which will give a second relation between F and h_0. From eq. (3.88) up to eq. (3.95) the solution is exactly the same. From that point, Crook's [28] approximation of the gap geometry for a conical asperity is substituted (see appendix B):

$$\frac{\partial q}{\partial r} = 12\eta_0 u_r \frac{r h_n - \int (h_n + h_0)\, dr + \int (h_n + h_0)\, dr|_{h_n=0}}{r(h_n + h_0)^3} \tag{4.25}$$

where:

$$h_n(r) = 0, \qquad r < a_n \tag{4.26}$$

$$h_n(r) = \frac{2\sqrt{2}\, s_n}{3\sqrt{a_n}} (r - a_n)^{3/2}, \quad r \geq a_n \tag{4.27}$$

Introduction of:

$$r = \hat{r}\bar{r} = a_n \bar{r}, \quad h = \hat{h}\bar{h} = \frac{4}{\pi} a_n s_n \bar{h}, \quad q = \hat{q}\bar{q} = \frac{1}{\alpha}\bar{q} \tag{4.28}$$

gives:

$$\frac{\partial \bar{q}}{\partial \bar{r}} = \mathcal{N} \frac{\bar{r}\bar{h}_n - \int (\bar{h}_n + \bar{h}_0)\, d\bar{r} + \int (\bar{h}_n + \bar{h}_0)\, d\bar{r}\big|_{\bar{h}_n=0}}{\bar{r}(\bar{h}_n + \bar{h}_0)^3} \tag{4.29}$$

in which:

$$\bar{h}_n(\bar{r}) = 0, \qquad \bar{r} < 1 \tag{4.30}$$

$$\bar{h}_n(\bar{r}) = \frac{8\sqrt{2}}{3\pi} (\bar{r} - 1)^{3/2}, \qquad \bar{r} \geq 1 \tag{4.31}$$

$$\mathcal{N} = 12\eta_0 u_r \frac{\hat{r}}{\hat{q}\hat{h}^2} = \frac{3\pi^2}{8} \frac{\eta_0 \alpha u_r}{s_n} \sqrt{\frac{\pi E'}{s_n F}} \tag{4.32}$$

Like in the line contact case, a large similarity between the conical and the spherical case is found. Apart from the constant $\mathcal{N}$, eq. (4.29) to eq. (4.32) are exactly the same as eq. (3.100) to eq. (3.103). Consequently, the integration of eq. (4.29) along the line $\phi = \pi$ with the starved boundary conditions will lead to the same result. With eq. (3.109), eq. (3.116) and $\mathcal{N}$ instead of $\mathcal{S}$ the integration yields:

$$-\mathrm{e}^{-\alpha p_0} = 2^{-1/3} 3^{-17/6} \pi^{5/3} \bar{h}_0^{-4/3} \mathcal{N} \left[1 + \left(\frac{27\sqrt{3}}{10\pi} \right)^{-9/14} \left(\frac{\bar{h}_{sm}}{\bar{h}_0} - 1 \right)^{-15/14} \right]^{-14/9} \tag{4.33}$$

Substitution of $u_r \overset{\phi=\pi}{=} -u_d/2$ in $\mathcal{N}$ and rearranging gives:

$$h_0 f_n \left(1 + \frac{\mathcal{A}}{h_0} \right)^{-1/3} = C_n(\eta_0 u_d \alpha^*) {s_n}^{-1} \tag{4.34}$$

where:

$$\mathcal{A} = A - h_{sm} \tag{4.35}$$

$$C_n = \pi^2 2^{-1/3} 3^{-11/6} \tag{4.36}$$

$$f_n = \left[1 + \left(\frac{27\sqrt{3}}{10\pi} \right)^{-9/14} \left(\frac{h_{sm}}{h_0} - 1 \right)^{-15/14} \right]^{14/9} \tag{4.37}$$

Similar to asperities given by a radius of curvature, the resemblance between the equations for line and point contact for asperities characterized by an amplitude and a slope is large. Even the correction factors f_w and f_n are the same, only the constants C_w and C_n differ.

Regarding the parameters determining the film thickness, again the lubricant is dominant. However, compared to asperities given by a radius of curvature, the geometry plays a more important role.

Chapter 5

Non-Newtonian lubricant behaviour

In chapter 2 it was concluded that at thin films non-Newtonian lubricant behaviour can affect the film shape. Since in case of micro-EHL thin films frequently occur, it is likely that non-Newtonian effects occur here as well. This chapter will present a preliminary analytical analysis of this effect. The analysis will be limited to a general EHL line contact with isoviscous lubricant behaviour.

5.1 Equations

The model used to describe non-Newtonian lubricant behaviour will be the commonly used Eyring model, in which the elastic component is neglected, see also eq. (2.2):

$$\dot{\gamma} = \frac{\tau_0}{\eta} \sinh\left(\frac{\tau}{\tau_0}\right) \tag{5.1}$$

From this equation the Reynolds equation for an Eyring lubricant will be derived. In a contact, force equilibrium on a infinitely small lubricant particle gives, see Figure 5.1:

$$\begin{aligned} p\,dz + \left(\tau + \frac{\partial \tau}{\partial z} dz\right) dx &= \left(p + \frac{\partial p}{\partial x} dx\right) dz + \tau\, dx \\ \frac{\partial \tau}{\partial z} &= \frac{\partial p}{\partial x} \end{aligned} \tag{5.2}$$

Integration of eq. (5.2) to z and substitution of this result in eq. (5.1) gives:

$$\frac{du}{dz} = \frac{\tau_0}{\eta} \sinh\left(\frac{\frac{dp}{dx} z + C_1}{\tau_0}\right) \tag{5.3}$$

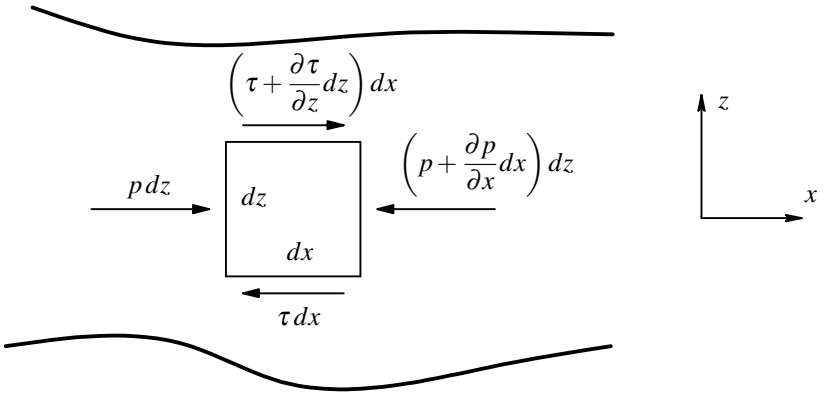

Figure 5.1: Force equilibrium.

Integrating once more gives the velocity profile across the oil film:

$$u(z)=\frac{\tau_0^2}{\eta p_x}\cosh\left(\frac{p_x z+C_1}{\tau_0}\right)+C_2 \tag{5.4}$$

where $p_x = dp/dx$. The constants C_1 and C_2 are solved with the no slip boundary conditions:

$$u(h/2)=u_m\left(1-\frac{S}{2}\right),\quad u(-h/2)=u_m\left(1+\frac{S}{2}\right) \tag{5.5}$$

where u_m is the mean surface velocity, $u_m=\big(u(h/2)+u(-h/2)\big)/2$, and S is the slip or slide to roll ratio, $S=\big(u(-h/2)-u(h/2)\big)/u_m$. For the velocity this yields:

$$u(z)=u_m-\frac{u_m S}{2}\frac{\sinh\left(\frac{p_x z}{\tau_0}\right)}{\sinh\left(\frac{p_x h}{2\tau_0}\right)}-\frac{\cosh\left(\frac{p_x z}{\tau_0}\right)-\cosh\left(\frac{p_x h}{2\tau_0}\right)}{2\eta p_x}\sqrt{\left(\frac{\eta u_m S p_x}{\sinh\left(\frac{p_x h}{2\tau_0}\right)}\right)^2+4\tau_0^4} \tag{5.6}$$

The mass flow per unit of length is obtained by integration of $\rho u(z)$:

$$\begin{aligned}\Phi(x)&=\int_{-h/2}^{h/2}\rho u(z)dz\\&=\rho u_m h-\frac{\rho\tau_0}{\eta p_x^2}\sqrt{\left(\frac{\eta u_m S p_x}{\sinh\left(\frac{p_x h}{2\tau_0}\right)}\right)^2+4\tau_0^4}\left[\frac{p_x h}{2\tau_0}\cosh\left(\frac{p_x h}{2\tau_0}\right)-\sinh\left(\frac{p_x h}{2\tau_0}\right)\right]\end{aligned} \tag{5.7}$$

This can also be written as:

$$\Phi(x)=\rho u_m h-\frac{\rho h^3}{12\eta_e}\frac{dp}{dx} \tag{5.8}$$

where:

$$\eta_e = \eta \frac{h^3 p_x^3}{12\tau_0} \left(\left[\frac{p_x h}{2\tau_0} \cosh\left(\frac{p_x h}{2\tau_0}\right) - \sinh\left(\frac{p_x h}{2\tau_0}\right) \right] \sqrt{\left(\frac{\eta u_m S p_x}{\sinh\left(\frac{p_x h}{2\tau_0}\right)} \right)^2 + 4\tau_0^4} \right)^{-1} \tag{5.9}$$

The Reynolds equation for Newtonian fluids can readily be recognized in eq. (5.8), see for instance eq. (2.16). Compared to the Newtonian case, only the viscosity is replaced by η_e, the effective viscosity. With

$$\mathcal{U} = \frac{\eta u_m S}{h\tau_0}, \quad \mathcal{P} = \frac{p_x h}{2\tau_0} \tag{5.10}$$

this effective viscosity can also be written as:

$$\eta_e = \eta \frac{\mathcal{P}^3}{3} \left(\left(\mathcal{P}\cosh\mathcal{P} - \sinh\mathcal{P} \right) \sqrt{\left(\frac{\mathcal{U}\mathcal{P}}{\sinh\mathcal{P}} \right)^2 + 1} \right)^{-1} \tag{5.11}$$

The group $\mathcal{U}$ can be regarded as the ratio between the shear flow induced shear stress and the non-Newtonian offset, whereas the group $\mathcal{P}$ represents a similar ratio based on the pressure flow induced shear stress.

At $dp/dx = 0$ the mass flow reads $\rho u_m h_0$. With constant ρ, eq. (5.8) can be written as:

$$\frac{1}{\eta_e}\frac{dp}{dx} = 12u_m \frac{h - h_0}{h^3} \tag{5.12}$$

To solve this equation the same solution procedure as the one for the Newtonian case is followed. Basically, this can be described as finding the point where the tangent line to the hydrodynamic pressure at its maximum gradient coincides with a tangent line to the Hertzian dry contact pressure. The basic assumptions are 1) the maximum gradient is reached at the beginning of the Hertzian contact zone and 2) the pressure gradient is constant in the small intermediate region between the start of the Hertzian contact zone and the point where the hydrodynamic pressure merges with the Hertzian pressure. The pressure distribution and film thickness are illustrated schematically in Figure 5.2. Note that for a constant η_e (Newtonian lubricant) the latter implies a constant film thickness in the intermediate region. With η_e according to eq. (5.11) this is not necessarily the case. However, for the analysis this has no consequences.

For the derivation of the tangent line to the hydrodynamic pressure, eq. (5.12) is used. The maximum hydrodynamic pressure gradient and accompanying film thickness follow directly from this equation, in terms of the unknown h_0. Integrating eq. (5.12) in the interval $[-\infty, -a_l]$ gives the pressure at the start of the Hertzian contact zone. Here is h replaced by the sum of the film thickness at which the maximum pressure occurs and h_l as given in eq. (3.11). With the pressure and its maximum gradient the tangent line can be constructed, starting at the beginning of the loaded zone. This line will be of the form $p(x) = C_1(h_0) + C_2(h_0)x$. In the loaded zone a tangent line to the contact pressure can be

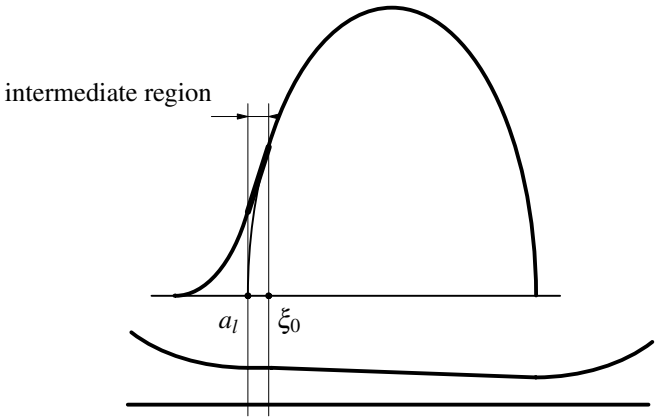

Figure 5.2: Schematic illustration of pressure distribution and film thickness in lubricated contact with isoviscous lubricant and elastically deformed surfaces. Reproduced from [99].

derived from the dry Hertzian contact theory. The only unknown in this line is the point where it touches the dry contact pressure, ξ_0, see Figure 5.2. This will lead to a line given by $p(x) = C_3(\xi_0) + C_2(\xi_0)x$. Equalizing both linear pressure distributions will lead to a set of two equations, from which h_0 and ξ_0 can be solved. This will give the expression for the film thickness.

In the Newtonian case the viscosity is a function of the pressure only, so that the derivation of the maximum pressure gradient and the pressure itself is straightforward using eq. (5.12). In the Eyring case however, this is not possible. The viscosity is a complicated term, in which both dp/dx and x, the latter through h, are present. To still be able to separate the terms containing the derivative of the pressure from the terms containing the spatial coordinate, η_e will be simplified. In the high pressure zone and far back into the inlet zone, i.e. where dp/dx is small, the viscosity can be simply approximated by $\eta/\sqrt{\mathcal{U}^2+1}$. The question is how large $\mathcal{P}$ becomes in the inlet. Because of the non-Newtonian behaviour it becomes larger than *one*. Additionally, since 200% slip is simulated, the shear flow induced shear stress will be large too. The ratio between the two numbers gives:

$$\frac{\mathcal{P}}{\mathcal{U}} = \frac{p_x h^2}{2\eta u_m S} \tag{5.13}$$

For a Newtonian fluid the maximum derivative can be calculated easily from eq. (2.16) (or eq. (5.12) with $\eta_e = \eta$):

$$\left.\frac{dp}{dx}\right|_{\max} = \frac{16 u_m \eta}{9 h_0^2} \quad \text{at} \quad h = \frac{3}{2} h_0 \tag{5.14}$$

If these values are substituted in eq. (5.13) the following is obtained:

$$\frac{\mathcal{P}}{\mathcal{U}} = \frac{2}{S} \tag{5.15}$$

For the pure slip case ($S = 2$) this means that around this region $\mathcal{P}$ and $\mathcal{U}$ are of equal magnitude. In the strong non-Newtonian case the film thickness as well as the maximum pressure gradient are smaller than for a Newtonian fluid, see for instance [27]. As a result, the ratio will be smaller than *one*. This means that for the fit of eq. (5.11), cases where $\mathcal{P} > \mathcal{U}$ do not have to be considered, provided that $\mathcal{P} > 1$. On the other hand, far into the inlet the same ratio reads:

$$\frac{\mathcal{P}}{\mathcal{U}} = \frac{6}{S} \tag{5.16}$$

This is based on the fact that in this region the mass flow through the contact is very small compared to the pressure induced flow and the shear induced flow, which means that the latter two are approximately of the same size with opposite signs. Consequently, in the region where $\mathcal{P}$ is small, the fit must be valid for $\mathcal{P} < 3\mathcal{U}$.

Based on series expansion around $\mathcal{P} = 0$ the following approximation is proposed:

$$\eta_e \approx \eta \frac{\sqrt{1 + \dfrac{2\mathcal{U}^2 - 3}{15(\mathcal{U}^2+1)}\mathcal{P}^2}}{\sqrt{\mathcal{U}^2+1}\sqrt{1 - \dfrac{\mathcal{U}^4 - 138\mathcal{U}^2 + 36}{1575(\mathcal{U}^2+1)^2}\mathcal{P}^4}} \tag{5.17}$$

Its relative deviation from eq. (5.11) is shown schematically in Figure 5.3. From the figure it can be concluded that the fit differs less than 10% for every $\mathcal{U}$ and $\mathcal{P} < 2$.

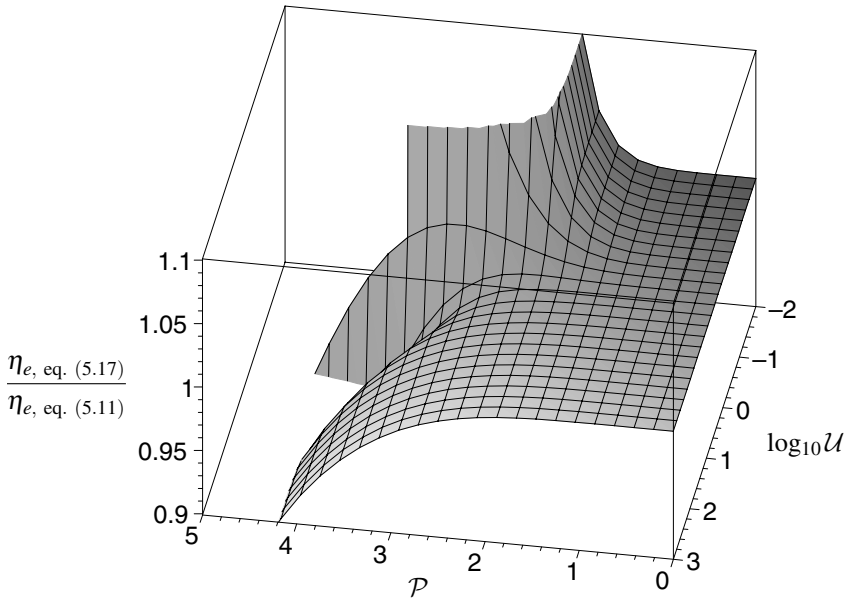

Figure 5.3: Comparison between η_e as defined by eq. (5.11) and its approximation given by eq. (5.17).

For larger $\mathcal{U}$ it is bounded by approximately $\mathcal{P} < 4$. Whether this approximation is sufficiently accurate or not, will be verified afterwards. The following dimensionless parameters will be used to rewrite eq. (5.12) and the parameters $\mathcal{U}$ and $\mathcal{P}$:

$$x = \bar{x}\hat{x} = \bar{x}a = \bar{x}\sqrt{\frac{8wR}{\pi E'}},\quad h = \bar{h}\hat{h} = \bar{h}h_H = \bar{h}\frac{8w}{\pi E'},\quad \eta_e = \bar{\eta}_e\hat{\eta}_e = \bar{\eta}_e\eta \tag{5.18}$$

$$p = \bar{p}\hat{p} = \bar{p}p_H = \bar{p}\sqrt{\frac{wE'}{2\pi R}},\quad \tau_0 = \bar{\tau}_0\hat{\tau}_0 = \bar{\tau}_0\frac{w}{\pi R}$$

This leads to:

$$\frac{1}{\bar{\eta}_e}\frac{d\bar{p}}{d\bar{x}} = \lambda\frac{\bar{h}-\bar{h}_0}{\bar{h}^3} \tag{5.19}$$

and

$$\mathcal{U} = \frac{\lambda S}{6\bar{\tau}_0\bar{h}} = \frac{\Theta S}{\bar{h}},\quad \mathcal{P} = \frac{\frac{d\bar{p}}{d\bar{x}}\bar{h}}{\bar{\tau}_0} = \frac{6\Theta\frac{d\bar{p}}{d\bar{x}}\bar{h}}{\lambda} \tag{5.20}$$

where

$$\lambda = \frac{3\pi^2 u_m\eta RE'}{4w^2},\quad \Theta = \frac{\lambda}{6\bar{\tau}_0} = \frac{\pi u_m\eta E'}{8w\tau_0} \tag{5.21}$$

Substitution of eq. (5.17) with eq. (5.20) into eq. (5.19) and solving for $d\bar{p}/d\bar{x}$ gives:

$$\frac{d\bar{p}}{d\bar{x}} = \lambda\left(\frac{\sqrt{105}}{18\Theta^2\bar{h}^3}\frac{\sqrt{\Xi_1}}{\sqrt{\Xi_2}}\sinh\left(\frac{1}{3}\operatorname{arcsinh}\Xi_3\right)\right)^{1/2} \tag{5.22}$$

with

$$\Xi_1 = \left(5\bar{h}^2S^2 - 24(\bar{h}-\bar{h}_0)^2\right)S^2\Theta^4 + \left(36\bar{h}^2(\bar{h}-\bar{h}_0)^2 + 10\bar{h}^4S^2\right)\Theta^2 + 5\bar{h}^6 \tag{5.23}$$

$$\Xi_2 = S^4\Theta^4 - 138S^2\Theta^2\bar{h}^2 + 36\bar{h}^4 \tag{5.24}$$

$$\Xi_3 = \frac{18\sqrt{105}}{7}\bar{h}\Theta^2(\bar{h}-\bar{h}_0)^2(S^2\Theta^2+\bar{h}^2)\frac{\sqrt{\Xi_2}}{{\Xi_1}^{3/2}} \tag{5.25}$$

For $\Theta \to 0$ the Newtonian equivalent, i.e. $\lambda(\bar{h}-\bar{h}_0)/\bar{h}^3$, is easy to identify. However, for $\Theta > 0$ and $S = 2$ a complication arises. The term Ξ_1 as well as Ξ_2 can become negative, which results into imaginary numbers. From eq. (5.26) follows that for values of Ξ_3 with

$$-\mathrm{I}\sinh\left(\frac{1}{3}\operatorname{arcsinh}(\mathrm{I}x)\right) = \sin\left(\frac{1}{3}\arcsin(x)\right),\quad |x| \le 1 \tag{5.26}$$

modulus smaller than *one*, the final result still will be valid. If the modulus is larger, the pressure derivative is consisting of a real and an imaginary part. To prevent this, first of all Ξ_1 must be limited to real and positive values. At the same time Ξ_2 must be large enough to limit Ξ_3 to real values or imaginary values with a modulus smaller than *one*.

A closer look at Ξ_1 reveals that only for $S \ge \sqrt{24/5}$ it is positive for every Θ and $\bar{h} \ge \bar{h}_0/2$ (the values for Θ and $\bar{h}$ in the region of interest, the inlet region). Based on this observation, a slightly different approximation of $\bar{\eta}_e$ is proposed which shows similar

behaviour for $S \geq 2$:

$$\bar{\eta}_e \approx \frac{\sqrt{1+\dfrac{\mathcal{U}^2-9/5}{9(\mathcal{U}^2+1)}\mathcal{P}^2}}{\sqrt{\mathcal{U}^2+1}\sqrt{1+\dfrac{29\mathcal{U}^2-8}{350(\mathcal{U}^2+1)^2}\mathcal{P}^4}} \tag{5.27}$$

For small $\mathcal{U}$ this fit is virtually the same as the one given by eq. (5.17). For large $\mathcal{U}$ the approximation is even slightly better. As shown in Figure 5.4, it holds for larger $\mathcal{P}$.

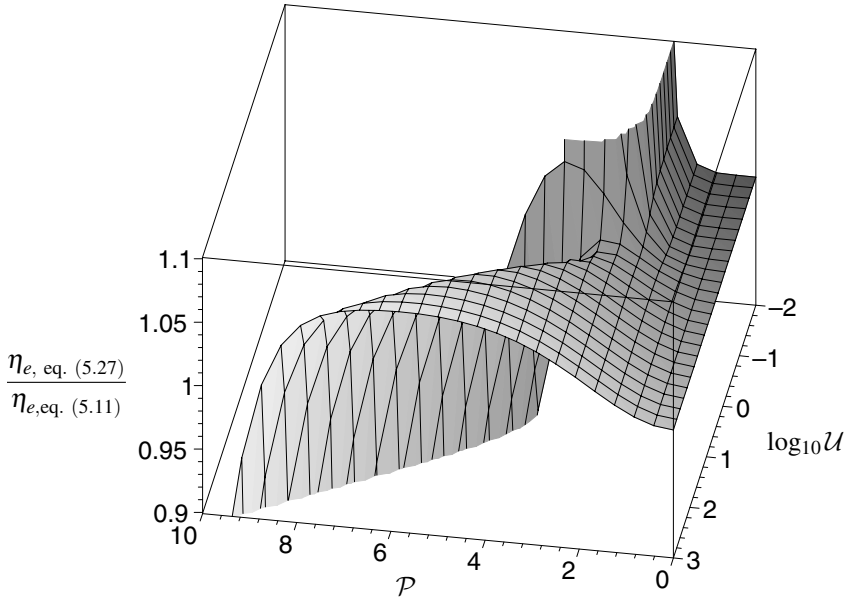

Figure 5.4: Comparison between η_e as defined by eq. (5.11) and its approximation given by eq. (5.27).

Substitution of eq. (5.27) in eq. (5.19) yields:

$$\frac{d\bar{p}}{d\bar{x}} = \lambda\left(\frac{\sqrt{35}}{9\sqrt{6}\Theta^2\bar{h}^4}\frac{\sqrt{\Xi_1}}{\sqrt{\Xi_2}}\sinh\left(\frac{1}{3}\operatorname{arcsinh}\Xi_3\right)\right)^{1/2} \tag{5.28}$$

with

$$\Xi_1 = \left(5\bar{h}^2S^2 - 20(\bar{h}-\bar{h}_0)^2\right)S^2\Theta^4 + \left(36\bar{h}^2(\bar{h}-\bar{h}_0)^2 + 10\bar{h}^4S^2\right)\Theta^2 + 5\bar{h}^6 \tag{5.29}$$

$$\Xi_2 = 29S^2\Theta^2 - 8\bar{h}^2 \tag{5.30}$$

$$\Xi_3 = \frac{27\sqrt{30}}{\sqrt{7}}\bar{h}^2\Theta^2(\bar{h}-\bar{h}_0)^2(S^2\Theta^2+\bar{h}^2)\frac{\sqrt{\Xi_2}}{{\Xi_1}^{3/2}} \tag{5.31}$$

From eq. (5.29) follows that substitution of $S = 2$ leads to positive values for Ξ_1 if $\bar{h} > \bar{h}_0/2$. Furthermore, from Ξ_2 follows that a real value for Ξ_3 is obtained if $\bar{h} < \sqrt{29/8}S\Theta$. For larger $\bar{h}$ it becomes imaginary. In appendix C it is shown that for $S = 2$

$$\|\Xi_3\| < 0.21 \;\text{ for }\; \bar{h} > \sqrt{\frac{29}{2}}\Theta \tag{5.32}$$

From this result follows that eq. (5.28) is valid for every $\bar{h}, \Theta$ and $S = 2$. Valid expressions of the pressure gradient for $S < 2$ can be obtained when different approximations of η_e are used. However, these approximations become worse as the critical S is smaller.

Following the isoviscous elastic solution method, the maximum derivative of the pressure and the film thickness at which it occurs are needed. For the Newtonian case the determination is straightforward, see eq. (5.15). In the Eyring case however, this can not be done in a simple way. However, additional assumptions can be made. Since the location of $(dp/dx)_{\max}$ is close to the loaded zone of the contact, h is already small. For strong non-Newtonian behaviour it means that the shear flow induced shear stress is already much larger than τ_0, which actually can be seen as $\mathcal{U} \gg 1$. As a result, eq. (5.27) reduces to:

$$\bar{\eta}_e \approx \frac{\sqrt{1+\frac{1}{9}\mathcal{P}^2}}{|\mathcal{U}|} \tag{5.33}$$

Substitution in eq. (5.19) and solving for $d\bar{p}/d\bar{x}$ gives:

$$\frac{d\bar{p}}{d\bar{x}} = \frac{\lambda}{\Theta}\frac{\bar{h}-\bar{h}_0}{\bar{h}\left(S^2\bar{h}^2 - 4(\bar{h}-\bar{h}_0)^2\right)^{1/2}} \tag{5.34}$$

The derivative with respect to $\bar{h}$ reads:

$$\frac{d}{d\bar{h}}\left(\frac{d\bar{p}}{d\bar{x}}\right) = \frac{\lambda}{\Theta}\frac{4(\bar{h}-\bar{h}_0)^3 + S^2\bar{h}^2(2\bar{h}_0-\bar{h})}{\bar{h}^2\left(S^2\bar{h}^2 - 4(\bar{h}-\bar{h}_0)^2\right)^{3/2}} \tag{5.35}$$

Solving $\bar{h}$ from the numerator with $S = 2$ yields:

$$\left.\frac{d\bar{p}}{d\bar{x}}\right|_{\max} = \frac{\left(\sqrt{5}+1\right)}{2\sqrt{2+\sqrt{5}}\left(\sqrt{5}+3\right)}\frac{\lambda}{6\Theta\bar{h}_0} \approx \frac{3}{20}\frac{\lambda}{\Theta\bar{h}_0} \quad \text{at} \quad \bar{h} = \frac{3+\sqrt{5}}{2}\bar{h}_0 \tag{5.36}$$

The next step is to find the value of the pressure at the start of the loaded zone. For this purpose eq. (5.28) through eq. (5.31) are used with:

$$\bar{h} = \frac{2\sqrt{2}}{3}\left(|\bar{x}|-1\right)^{3/2} \;+\; \frac{3+\sqrt{5}}{2}\bar{h}_0 \tag{5.37}$$

The expression for $\bar{h}$ is simply the Crook approximation of the Hertzian dry contact geometry outside the loaded zone as defined in eq. (3.24), to which the film thickness at the point of maximum pressure gradient is added. Substitution of:

$$-\bar{x} = \Theta^{2/3}y + 1, \quad \bar{h}_0 = \Theta\tilde{h}_0, \quad S = 2 \tag{5.38}$$

gives for eq. (5.28) through eq. (5.31):

$$\bar{p} = \frac{\lambda}{\Theta^{4/3}} \int_0^\infty \left(\frac{\sqrt{35}}{9\sqrt{6}\tilde{h}^4} \frac{\sqrt{\Xi_1}}{\sqrt{\Xi_2}} \sinh\left(\frac{1}{3}\operatorname{arcsinh}\Xi_3\right)\right)^{1/2} dy \tag{5.39}$$

with:

$$\Xi_1 = 80\tilde{h}_0(2\tilde{h}-\tilde{h}_0) + \tilde{h}^2(19\tilde{h}^2 - 18\tilde{h}\tilde{h}_0 + 9\tilde{h}_0^2) + 5\tilde{h}^6 \tag{5.40}$$

$$\Xi_2 = 116 - 8\tilde{h}^2 \tag{5.41}$$

$$\Xi_3 = \frac{27\sqrt{30}}{\sqrt{7}}\tilde{h}^2(\tilde{h}-\tilde{h}_0)^2(4+\tilde{h}^2)\frac{\sqrt{\Xi_2}}{{\Xi_1}^{3/2}} \tag{5.42}$$

$$\tilde{h} = \frac{2\sqrt{2}}{3}y^{3/2} + \frac{3+\sqrt{5}}{2}\tilde{h}_0 \tag{5.43}$$

Unfortunately, no analytical solution is found. Therefore, numerical integration is performed, from which the result is shown in Figure 5.5. For small Θ, i.e. large $\tilde{h}_0$, an asymptotic solution is found. Here the pressure converges to its Newtonian solution:

$$\bar{p} = \frac{\lambda}{\Theta^{4/3}} 2^{7/3}3^{-17/6}\pi\frac{(5+3\sqrt{5})}{(3+\sqrt{5})^{-7/3}}\tilde{h}_0^{-4/3} = \lambda 2^{7/3}3^{-17/6}\pi\frac{(5+3\sqrt{5})}{(3+\sqrt{5})^{-7/3}}\bar{h}_0^{-4/3} \tag{5.44}$$

In the region of interest, i.e. large Θ or small $\tilde{h}_0$, no asymptotic solution could be found.

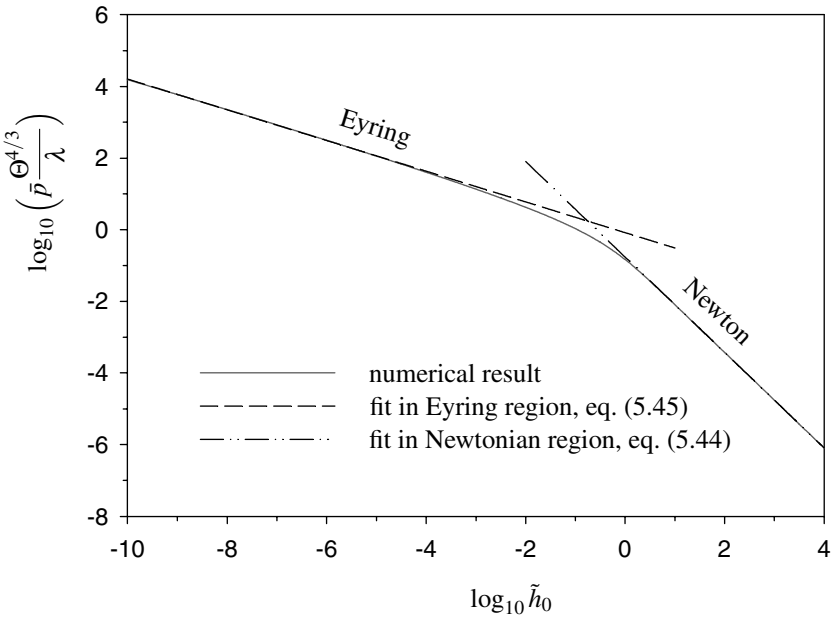

Figure 5.5: Pressure at the start of the loaded zone as a function of $\tilde{h}_0$.

Based on the fit shown in Figure 5.5 the pressure is approximated by:

$$\bar{p} \approx \frac{\lambda}{\Theta^{4/3}} \frac{5}{6} \tilde{h}_0^{-3/7} = \frac{5}{6} \lambda \, \Theta^{-19/21} \bar{h}_0^{-3/7} \tag{5.45}$$

Now the hydrodynamic pressure and its derivative at $\bar{x} = -1$ are known, the pressure in the region $[-1, \bar{\xi}_0]$ can be given by:

$$\begin{aligned} \bar{p}(\bar{x}) = \frac{5}{6} \lambda \, \Theta^{-19/21} \bar{h}_0^{-3/7} \; + \; & \frac{3}{20} \frac{\lambda}{\Theta \bar{h}_0} (\bar{x} + 1) \\ = \; & \frac{\lambda}{\Theta \bar{h}_0} \left(\frac{5}{6} \Theta^{2/21} \bar{h}_0^{4/7} + \frac{3}{20} \right) \; + \; \frac{3}{20} \frac{\lambda}{\Theta \bar{h}_0} \bar{x} \end{aligned} \tag{5.46}$$

Subsequently, the same approximation based on the Hertzian theory is needed. The Hertzian pressure is given by:

$$\bar{p} = \sqrt{1 - \bar{x}^2} \tag{5.47}$$

Close to $\bar{x} = -1$ this can be approximated well by:

$$\bar{p} \approx \sqrt{2} \sqrt{\bar{x} + 1} \tag{5.48}$$

Its derivative reads:

$$\frac{d\bar{p}}{d\bar{x}} = \frac{1}{\sqrt{2}\sqrt{\bar{x} + 1}} \tag{5.49}$$

Based on eq. (5.48) and eq. (5.49) the pressure in the intermediate region reads:

$$\bar{p} = \sqrt{2} \sqrt{\bar{\xi}_0 + 1} + \frac{\bar{x} - \bar{\xi}_0}{\sqrt{2}\sqrt{\bar{\xi}_0 + 1}} = \frac{\bar{\xi}_0 + 2}{\sqrt{2}\sqrt{\bar{\xi}_0 + 1}} + \frac{1}{\sqrt{2}\sqrt{\bar{\xi}_0 + 1}} \bar{x} \tag{5.50}$$

Equalizing eq. (5.46) and eq. (5.50) gives two equations from which $\bar{h}_0$ and $\bar{\xi}_0$ can be solved in terms of λ and Θ. The solution for $\bar{h}_0$ gives the expression for the central film thickness under strong non-Newtonian conditions:

$$\bar{h}_0 = 2^{-7/5} \Theta^{-4/3} \lambda^{7/5} \tag{5.51}$$

This can also be written as:

$$h_0 = 2^{14/5} 3^{7/5} \pi^{7/15} \frac{{\tau_0}^{4/3} {u_m}^{1/15} {\eta_0}^{1/15} R^{7/5}}{w^{7/15} {E'}^{14/15}} \tag{5.52}$$

Its Newtonian equivalent reads, see for instance Moes [86]:

$$h_0 = \frac{2^{17/5} 5^{3/10} \pi^{1/2}}{3^{37/20}} \frac{{u_m}^{3/5} {\eta_0}^{3/5} R^{3/5}}{w^{1/5} {E'}^{2/5}} \tag{5.53}$$

or:

$$\bar{h}_0 = \frac{2^{8/5} 5^{3/10} \pi^{3/10}}{3^{49/20}} \lambda^{3/5} \tag{5.54}$$

5.1.1 Region of validity for the approximation of η_e.

Since the approximation of the viscosity given by eq. (5.27) is valid for limited $\mathcal{P}$, a verification of the maximum $\mathcal{P}$ is necessary. At the point of the maximum pressure derivative this can be given by means of combining eq. (5.20) and eq. (5.36):

$$\mathcal{P} = \frac{9}{20}(3+\sqrt{5}) \approx 2.4 \tag{5.55}$$

This value shows that the approximation is sufficiently accurate in case of higher $\mathcal{U}$, as was assumed when deriving eq. (5.36). Further into the loaded zone $d\bar{p}/d\bar{x}$ as well as $\bar{h}$ are smaller, which means that $\mathcal{P}$ must be smaller too. Back into the inlet zone $\bar{h}$ increases, which might compensate for the decrease of the pressure derivative. However, eventually it will fall back to *zero*, since far into the inlet zone $\mathcal{U} \to 0$ and $\mathcal{P}/\mathcal{U} = 3$, see eq. (5.16). In appendix D it is shown that for $S = 2$

$$\mathcal{P}_{\max} \approx 6^{2/5}\Theta^{1/5}\bar{h}_0^{-1/5} \quad \text{at} \quad \bar{h} \approx \frac{7}{5}\Theta^{2/5}\bar{h}_0^{3/5} \tag{5.56}$$

Substitution of eq. (5.51) gives:

$$\mathcal{P}_{\max} \approx 3^{2/5}2^{17/25}\Theta^{7/15}\lambda^{-7/25} \quad \text{at} \quad \bar{h} \approx \frac{7}{5}2^{-21/25}\Theta^{-2/5}\lambda^{21/25} \tag{5.57}$$

Based on this result, it cannot be said beforehand if the approximation of the effective viscosity can be applied. The position as well as the value of $\mathcal{P}_{\max}$ depend on the conditions. Moreover, a value for $\mathcal{U}$ is needed as well. Since $\mathcal{P}_{\max}$ might occur further back into the inlet zone, $\mathcal{U} \gg 1$ can no longer be assumed. The value of $\mathcal{U}$ at the maximum $\mathcal{P}$ reads:

$$\mathcal{U}_{\mathcal{P}\max} = \frac{5}{7}2^{46/25}\Theta^{7/5}\lambda^{-21/25} \tag{5.58}$$

Note that, similar to the way as described in appendix D, the pressure derivative given by eq. (5.28) can be analyzed to find its maximum. This leads to the same expression as the simplified approach based on eq. (5.33). However, this simplified approach cannot be used to analyze $\mathcal{P}$. It will lead to:

$$\mathcal{P} = 6\frac{\bar{h}-\bar{h}_0}{\left(S^2\bar{h}^2 - 4(\bar{h}-\bar{h}_0)^2\right)^{1/2}} \tag{5.59}$$

For $S = 2$ no maximum is found, since eq. (5.59) rises to *infinity* as $\bar{h}$ increases.

5.2 Numerical verification

In order to verify whether eq. (5.51) is a fair approximation of the film thickness at strong non-Newtonian behaviour or not, the program as developed in section 3.2.8 is slightly modified to account for Eyring behaviour. Basically the piezoviscous viscosity is replaced by eq. (5.11). The result for a wide range of λ and Θ is shown in Figure 5.6. For λ a range corresponding to the region between $M = 10^1$ and $M = 10^3$ is covered. The parameter Θ is chosen such that for every λ both the Newtonian and the Eyring region are

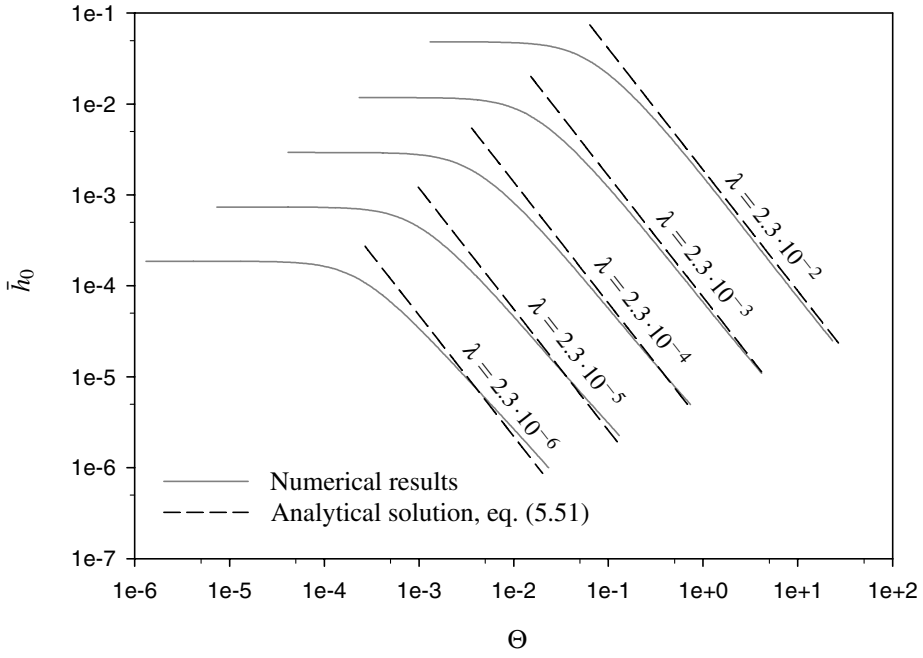

Figure 5.6: $\bar{h}_0$ as a function of Θ and λ, analytical asymptotic Eyring solution versus numerical results.

included. As can be seen, at the higher values for λ (lower M) the agreement between the analytical and the numerical method is fairly good. At higher loading conditions the slopes of the curves start to deviate, leading to significant difference in the extreme Eyring region.

Another possibility is to combine the analytical solutions in the Newtonian region and the one in the Eyring region. For this purpose the following equation is proposed:

$$\bar{h}_0 = \left(\frac{1}{\bar{h}_{0,\,\mathrm{New}}} + \frac{1}{\bar{h}_{0,\,\mathrm{Eyr}}} \right)^{-1} \tag{5.60}$$

where $\bar{h}_{0,\,\mathrm{New}}$ and $\bar{h}_{0,\,\mathrm{Eyr}}$ are given by eq. (5.54) and eq. (5.51) respectively. The result is shown in Figure 5.7. In this way a simple and easy to use formula is obtained which covers the complete isoviscous EHL regime.

5.2.1 Verification of the approximation of η_e.

Based on the approximation of the effective viscosity, an estimation of the maximum $\mathcal{P}$ and accompanying $\mathcal{U}$ was made in section 5.1.1. The results of these numbers are plotted in Figure 5.8 and Figure 5.9 for $M = 13$ and $M = 1280$ respectively. Furthermore, the required value for $\mathcal{U}$, denoted as $\mathcal{U}_{\mathrm{req}}$, is plotted. This is the minimum value of $\mathcal{U}$ needed to limit the difference between the approximation of η_e and eq. (5.11) to 10% at $\mathcal{P}_{\max}$. It is observed that in the Eyring region, i.e. $\bar{h}_0 < 10^{-3}\Theta$ which follows from

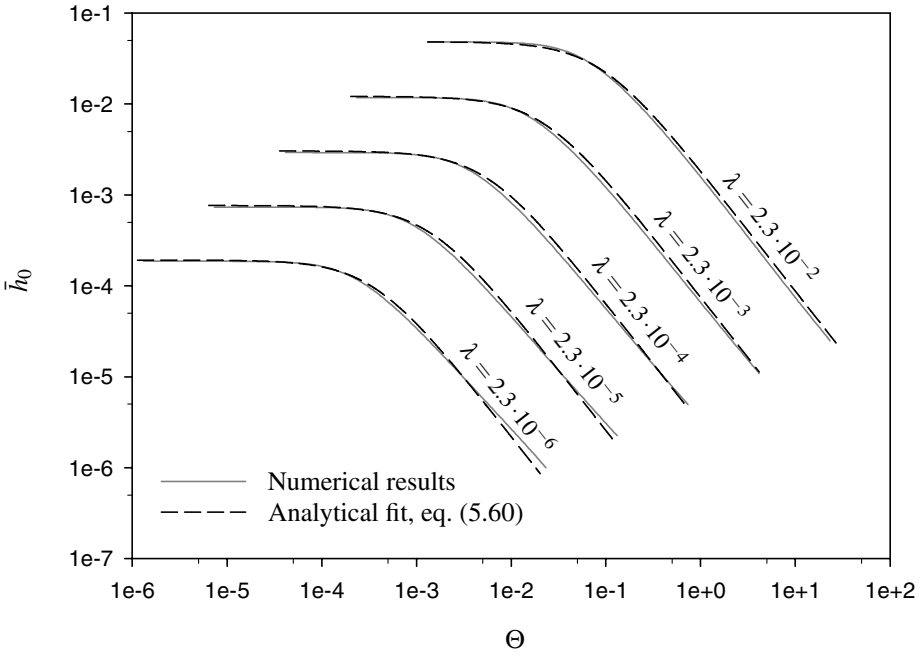

Figure 5.7: $\bar{h}_0$ as a function of Θ and λ, combination of asymptotic solutions versus numerical results.

Figure 5.5, the $\mathcal{U}_{\text{req}}$ is always larger than $\mathcal{U}_{\mathcal{P}\max}$. This implies that at the point where $\mathcal{P}$ is at its maximum, the approximation of η_e is not valid anymore. On the other hand, the agreement between the prediction of h_0 and the numerical results is still rather good. A reason for this can be sought in the fact that $\mathcal{P}_{\max}$ is located relatively far back into the inlet zone, the region where $h \gg h_0$. Inaccurate approximations of η_e might not have a large influence on the final result. This is, for instance, also the case for the Crook approximation of the deformation outside the loaded zone. It can be shown that for isoviscous EHL the Crook approximation deviates more than 10% from the analytical value if $\bar{h} > 0.73$, or $h/h_0 > 1.56\lambda^{-3/5}$. For $M = 13$ this leads to $h/h_0 > 15$, for $M = 1280$ to $h/h_0 > 3800$. The effect on the calculation of the central film thickness is only minor. With eq. (5.56) and $\bar{h}_0 = 10^{-3}\Theta$ (the beginning of the strong non-Newtonian zone) the location of $\mathcal{P}_{\max}$ is at $h/h_0 = 22$. For smaller λ or larger Θ this value increases.

Closer to the loaded zone $\mathcal{P}$ becomes smaller, whereas at the same time $\mathcal{U}$ increases. Both effects will result into a quick improvement of the accuracy of the approximation of η_e. For instance, in section 5.1.1 it is shown that $\mathcal{P}_{\max} = 2.4$ at the point where $(dp/dx)_{\max}$. The accompanying $\mathcal{U}$ reads:

$$\mathcal{U}_{(dp/dx)_{\max}} = \frac{4\Theta}{(3+\sqrt{5})\bar{h}_0} = \frac{2^{17/5}\Theta}{(3+\sqrt{5})\lambda^{7/5}} \tag{5.61}$$

At $\bar{h}_0 = 10^{-3}\Theta$ $\mathcal{U}_{(dp/dx)_{\max}} \approx 760$, which is sufficient. Again, for smaller λ or larger Θ the value increases.

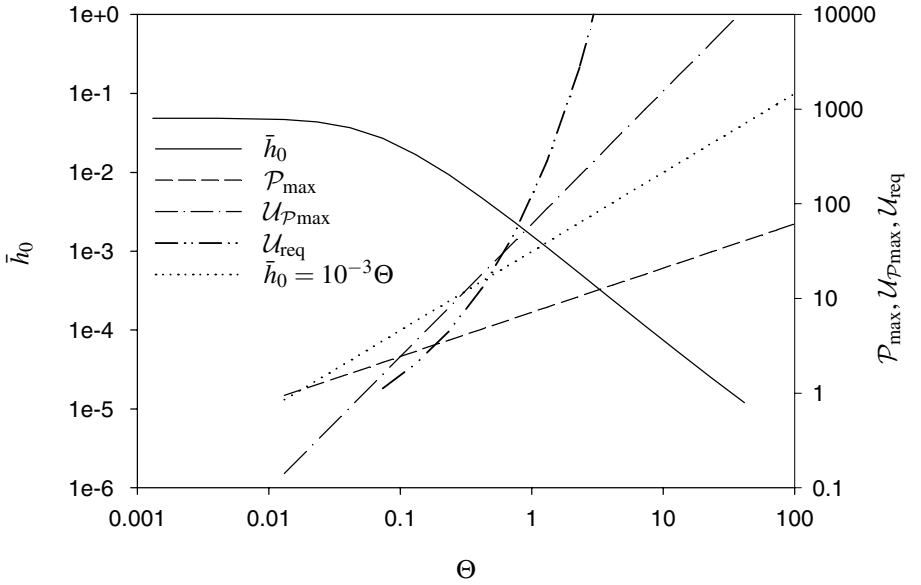

Figure 5.8: $\bar{h}_0$, $\mathcal{P}_{\max}$, $\mathcal{U}_{\mathcal{P}\max}$ and $\mathcal{U}_{\text{req}}$ as a function of Θ for $\lambda = 2.3 \cdot 10^{-2}$ ($M = 13$).

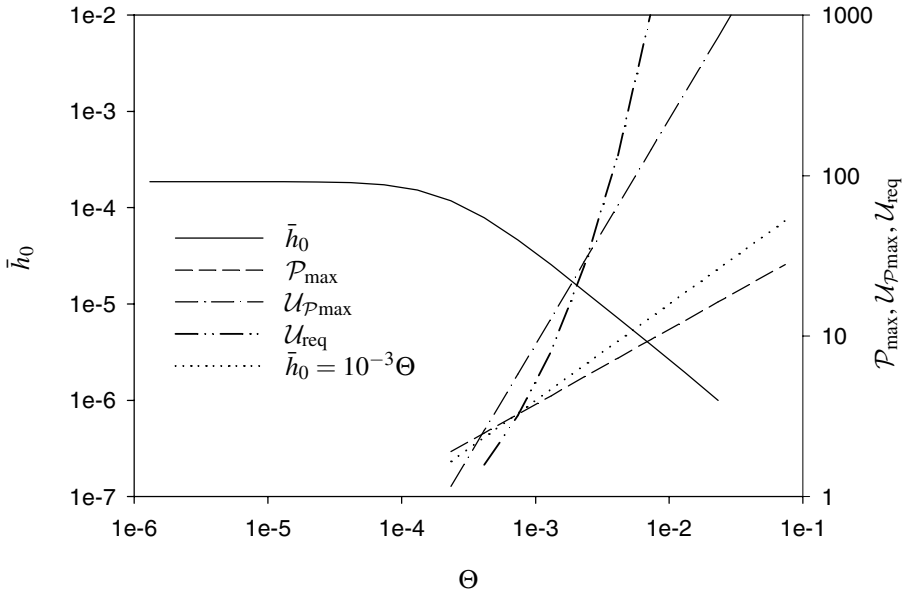

Figure 5.9: $\bar{h}_0$, $\mathcal{P}_{\max}$, $\mathcal{U}_{\mathcal{P}\max}$ and $\mathcal{U}_{\text{req}}$ as a function of Θ for $\lambda = 2.3 \cdot 10^{-6}$ ($M = 1280$).

5.3 Piezoviscous lubricant

For a piezoviscous lubricant no analytical asymptotic solution is found yet. The main problem is to find a suitable approximation of the effective viscosity as given by eq. (5.11). Such an approximation is necessary to be able to split the Reynolds equation in a left side containing the pressure terms and a right side containing the spatial coordinate, see page 70. For an isoviscous lubricant this is relatively easy, because only $\mathcal{P}$ contains the pressure. In the piezoviscous case however, through η the pressure is present in $\mathcal{U}$ as well.

It is still possible to construct a fit based on numerical simulations and in many cases values subtracted from such a fit will be sufficient. It must be noted that the introduction of a parameter like α^* is leading to a significant increase in numerical effort and a more complicated graphical representation of the work.

5.4 Summary

For an isoviscous EHL contact a fair approximation of the film thickness under Newtonian as well as under non-Newtonian conditions is given by eq. (5.60). To incorporate these results in the micro-EHL model, the Eyring asymptote as given by eq. (5.51) or eq. (5.52) can be used. For the starved approach only the integration boundaries in eq. (5.39) should be slightly modified.

When the Eyring solution as given by eq. (5.52) is compared to the Newtonian solution given in eq. (5.53), it is observed that in the Eyring case the effect of the surface velocity and viscosity on the film thickness is greatly reduced. An increase in one of the variables leads to higher shear stresses, which on its turn reduces the effective viscosity. As a result, the film thickness hardly increases. On the other hand, the influence of the load, modulus of elasticity and reduced radius of curvature is more pronounced. This is because, from a Hertzian point of view, these variables affect the pressure derivative in the inlet and thus the effective viscosity. Concluding, it can be said that for the film build up the shape of the contact and the loading become more important when the non-Newtonian region is entered.

The equations for the central film thickness derived in this chapter are valid in the isoviscous EHL region. However, for micro-EHL, the piezoviscous region is of greater importance. Unfortunately, the analytical approach as followed in the isoviscous region did not lead to a similar result in the piezoviscous Eyring region. To get an estimation of the film thickness in this region it seems that numerical simulations are inevitable.

Chapter 6

Stribeck curves

As stated in chapter 1, micro-EHL can have a large influence on wear and friction. In this chapter its relation to friction is discussed in more detail.

6.1 Introduction

To demonstrate the effect of micro-EHL on the Stribeck curve, the work of Faraon [38] on predicting Stribeck curves is used as a starting point. His model can be seen as the simulation of the ML regime, in which the known (E)HL theory, an asperity contact model and a known value for the coefficient of friction in the BL regime are combined in an elegant way. It is based on the concept that at thinner films more asperities come into contact and partly transfer the load, whereas at the same time the load bearing capacity of the fluid is reducing. This idea was first introduced by Johnson et al. [71]. They combined the statistical rough surface theory of Greenwood and Williamson [50] with the general EHL theory to predict the surface separation and loading. Gelinck [45] used this model and combined it with the theory of Greenwood and Tripp [49] to calculate the nominal contact area for lightly loaded line contacts. Furthermore, he determined which part of the contact contributes to the hydrodynamic bearing area and which part consists of asperity contact. Once this was known, the coefficient of friction could be determined. For the hydrodynamic friction Gelinck used the Eyring theory, which also accounts for non-Newtonian effects. An experimentally obtained friction value in the BL regime was used for the friction in the asperity contacts.

Since the asperity contact is based on statistical averages, the model as developed by Gelinck works well for surfaces with a Gaussian roughness distribution, which is supported by measurements [45]. However, for non-Gaussian surfaces, Faraon [38] showed that the model can differ significantly from the measurements. Moreover, it gives valid results only if the deformation of the asperities does not exceed the neutral line of the undeformed roughness, as that would require negative hydrodynamic films. Both shortcomings are accounted for in the work of Faraon [38]. First, he developed a deterministic contact model, which greatly reduced the difference between theory and experiments for non-Gaussian surfaces. Secondly, based on the work of Johnson et al. [71], he used a

different representation of the average hydrodynamic film thickness so that the neutral line of surface is no longer used as a reference for the hydrodynamic film. In this way the theory also becomes valid for large asperity deformations. It is this model which is used as a base for the incorporation of micro-EHL in the prediction of Stribeck curves.

6.2 Micro-EHL in the Stribeck curve

Since micro-EHL takes place on asperity level, it leaves the determination of the hydrodynamic part of the Stribeck curve model unchanged. As for the asperity contacts, the formation of a small film will lead to additional asperity deformation. This results into an increase of the asperity loading, which on its turn gives rise to an increase in average film thickness. More significant changes take place on friction level. Instead of the known coefficient of friction for the BL regime, at each micro contact the friction is calculated using the same approach as for the macroscopic hydrodynamic traction. The basic equation in this approach is shown in eq. (6.1).

$$\tau_m = \tau_0 \operatorname{arcsinh} \frac{\dot{\gamma}\eta}{\tau_0} \tag{6.1}$$

Note that thermal effects are ignored. The shear rate is approximated by the velocity difference of the contacting surfaces divided by the central film thickness following from the micro-EHL model as developed in section 3.3. The viscosity is calculated using the Roelands equation as given in eq. (3.52), in which the sum of the average micro contact pressure and the surrounding pressure is substituted. Multiplying the average shear stress with the micro contact area gives the friction force at the asperity contact. From this point the approach of Faraon is followed to obtain the macroscopic coefficient of friction.

6.3 Detailed description of the procedure with application

For convenience the model of Faraon is denoted as the *ML* model and the model including micro-EHL is indicated by the *mEHL* model. The calculation of the Stribeck curve is described on the basis of a practical example. For this purpose the surface as shown in Figure 6.1 is used. It represents the combined undeformed surface roughness in a contact. The surface is measured using a non-contacting interference microscope. The image consists of five separate images which are stitched together using the method as described in Sloetjes et al. [95]. Note that the white spots are areas where the instrument was not able to measure the surface topography with sufficient accuracy. These spots are left empty. The diameter of the measured spot corresponds with the dry Hertzian contact area under conditions as given in Table 6.1. From the data follows that $a_s = 0.25$ mm with $p_H = 0.45$ GPa. The pressure is kept fairly low, in order to meet the assumptions under which the *mEHL* model was developed. The usual way to simulate a Stribeck curve is to vary the velocity and to keep all other parameters constant. This is also followed here. Furthermore, it is assumed the rougher surface is stationary, so that a situation of 200% slip is obtained.

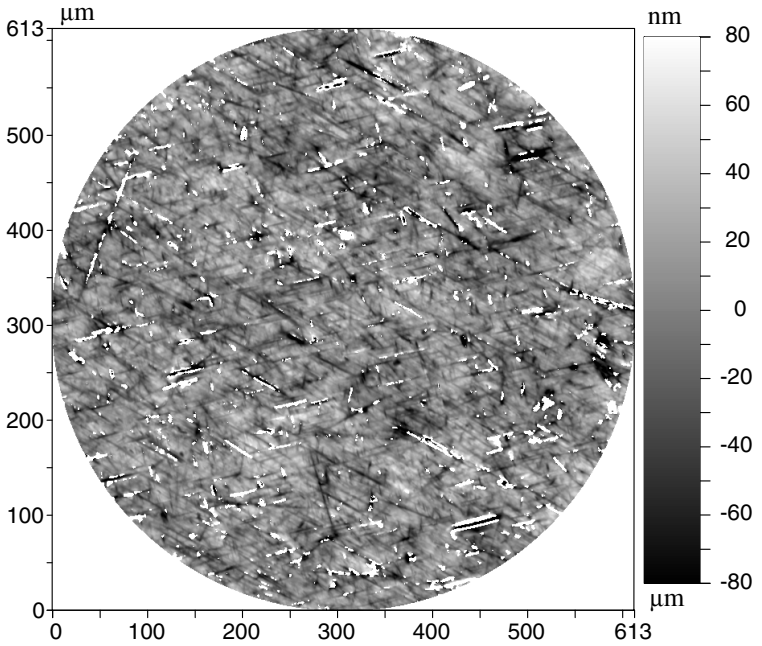

Figure 6.1: Surface with Gaussian distribution. $R_q = 25$ nm. Sampling interval 0.846 µm in both x and y direction.

Table 6.1: Operating conditions.

η_0	=	18.2 mPa s	z	=	0.55
p_c	=	198 MPa	η_∞	=	$6.315 \cdot 10^{-5}$ Pa s
α_0	=	15.7 GPa^{-1}	τ_0	=	11.8 MPa
F	=	90 N	R'_x	=	50.0 mm
E'	=	231 GPa			

6.3.1 Hydrodynamic part

To determine the film thickness in the full film regime (and in the hydrodynamic part in the ML regime), the formula as proposed by Nijenbanning et al. [88] is used. Note that in the *mEHL* model this film thickness is taken for h_{sm}. The next step is to determine the hydrodynamic friction. For this eq. (6.1) is used. In this equation, the Eyring stress τ_0 is given in Table 6.1. The shear rate $\dot{\gamma}$ follows from u_d/h_{sm}. Since 200% slip is assumed, u_d is equal to the sum velocity u_s used as the horizontal axis in the Stribeck curve calculation. The viscosity is calculated according to the Roelands equation as given eq. (3.52), in which the average hydrodynamic pressure and η_0, z, p_c and η_∞ from Table 6.1 are substituted. The last step is to multiply the average shear stress from eq. (6.1)

with the nominal contact area in order to obtain the hydrodynamic friction force.

6.3.2 Asperity contact part

The parameters for the hydrodynamic part as discussed above are required for both the *ML* model as well as the *mEHL* Stribeck curve. The only parameter left to determine is the friction at the asperities. In the *ML* model the coefficient of friction in the BL regime is used: $\mu_{\mathrm{BL}} = 0.13$. This is multiplied by the asperity contact force to obtain the friction force at the asperity contact.

In the *mEHL* model the determination of the asperity friction force requires a bit more effort. First, the local film thickness must be determined. For this, at each asperity the following parameters are needed (see eq. (3.117) to eq. (3.120), eq. (3.52), eq. (3.68), eq. (3.59) and eq. (3.55)): h_{sm}, A, β_s, η_0, z, u_d and p_0. The film thickness h_{sm} simply follows from the hydrodynamic part, as also mentioned in section 6.3.1. From the surface a complete list of asperities, their reduced radius of curvature, initial amplitude and position in the macro contact is created. From this list the asperities in contact are selected. Compared to the *ML* model the number of asperities in contact is slightly larger. In the *mEHL* model all asperities with amplitude tip less than h_{sm} away from the counter surface should be taken into account, whereas in the *ML* model only asperities penetrating the counter surface are assumed to deform. This is illustrated in Figure 6.2, in which the asperities indicated by *ML* are in contact and boundary lubricated in the *ML* model and asperities indicated by *mEHL* are "in contact" only in the *mEHL* model Stribeck curve. The lubricant parameters η_0 and z are given in Table 6.1. The velocity u_d follows directly

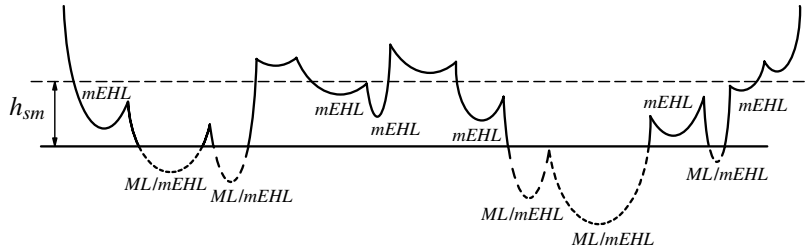

Figure 6.2: Asperities in contact. Both models indicated by *ML/mEHL*, *mEHL* model only indicated by *mEHL*.

from the velocity used in the Stribeck curve calculation. For p_0, first the macroscopic hydrodynamic pressure distribution is required. Combined with the position of the asperity in the contact this will give the surrounding asperity pressure. This completes the list of parameters needed to calculate the local film thickness h_0 at each asperity contact.

The next step is to calculate the coefficient of friction in the micro contact. The procedure is similar to the determination of the friction in the hydrodynamic part, which means that eq. (6.1) is used. The Eyring stress τ_0 is given in Table 6.1. The shear rate $\dot{\gamma}$ follows from u_d/h_0. For the determination of the viscosity, the average pressure in the micro contact is needed. The average pressure follows from the maximum Hertzian

pressure. For point contact this pressure is given by [58]:

$$p_H = \frac{1}{\pi}\left(\frac{3FE'^2}{2\beta_s^2}\right)^{1/3} \tag{6.2}$$

Substitution of eq. (3.85) leads to:

$$p_H = \frac{E'a_s}{\pi\beta_s} \tag{6.3}$$

With eq. (3.83) and eq. (3.84) this can also be written as:

$$p_H = \frac{E'}{\pi}\sqrt{\frac{h_0 - h_{sm} + A}{\beta_s}} \tag{6.4}$$

The average pressure then follows from:

$$p_m = \frac{2}{3}p_H = \frac{2E'}{3\pi}\sqrt{\frac{h_0 - h_{sm} + A}{\beta_s}} \tag{6.5}$$

To obtain the right viscosity, the average pressure must be added to the surrounding pressure p_0. This sum is substituted in the Roelands equation given in eq. (3.52). The last step is to multiply the shear stress by the contact area. With eq. (3.83) and eq. (3.84) the contact area is given by:

$$\pi a_s^2 = \pi\beta_s(h_0 - h_{sm} + A) \tag{6.6}$$

The sum of all the friction force components at the micro contacts added to the macroscopic hydrodynamic friction force from the hydrodynamic part gives the total friction force. The coefficient of friction is obtained by dividing it by the normal force given in Table 6.1.

6.3.3 Results

Before the actual Stribeck curve can be calculated, the asperities must be located and each individual radius of curvature and amplitude must be determined. The asperities are selected according to the nine-point summit definition, i.e. if the centre point of a 3X3 window is higher than its eight neighbours, this point is then defined as an asperity summit. The distribution of the summits is shown in Figure 6.3. Once all asperities are located, their individual radius of curvature is calculated following the method as

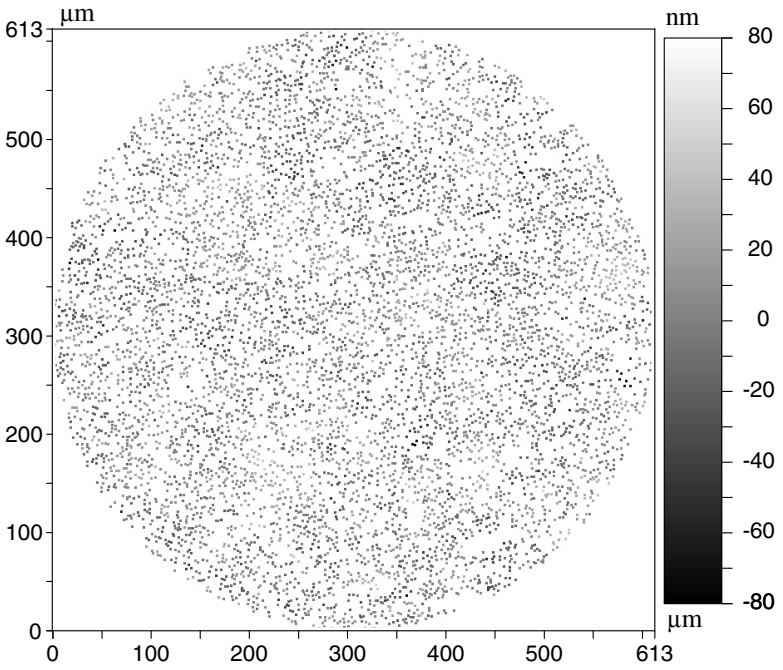

Figure 6.3: Distribution of asperity tops.

proposed by Greenwood and Williamson [50] and given by eq. (6.7) to eq. (6.10).

$$\rho_x = \frac{z_{i-1,j} - 2z_{i,j} + z_{i+1,j}}{d_x^2} \tag{6.7}$$

$$\rho_y = \frac{z_{i,j-1} - 2z_{i,j} + z_{i,j+1}}{d_y^2} \tag{6.8}$$

$$\rho_{i,j} = \sqrt{\rho_x \rho_y} \tag{6.9}$$

$$\beta_{i,j} = \frac{1}{\rho_{i,j}} \tag{6.10}$$

where ρ_x local curvature in x-direction
ρ_y local curvature in y-direction
$z_{i,j}$ height data
d_x sampling interval in x-direction
d_y sampling interval in y-direction
$\rho_{i,j}$ equivalent local curvature
$\beta_{i,j}$ local radius of curvature

Note that $\beta_{i,j} = \beta_s$ and for the centre point of an asperity $z_{i,j} = A$. Although the Greenwood and Williamson [50] parameters β, n σ^* and their product are not required for the calculation, they are given here too for the sake of completeness:

$$\beta = 93\ \mu\text{m}, \quad n = 0.0255\ \mu\text{m}^{-2}, \quad \sigma^* = 0.018\ \mu\text{m}, \quad \beta n \sigma^* = 0.043 \tag{6.11}$$

It was shown by Whitehouse and Archard [111] that $\sigma^* = 0.7R_q$ and by Johnson et al. [71] that $\beta n \sigma^* = 0.05$. The numbers for the present surface indicate that it follows the Gaussian trend. Moreover, the distance between the mean of the asperity summits and the neutral line of the surface is 0.018 µm, not far from the theoretical $0.8R_q$ [111].

If all asperity data are available, the Stribeck curve can be calculated. Figure 6.4 shows the result. In the full film regime obviously no differences are found between

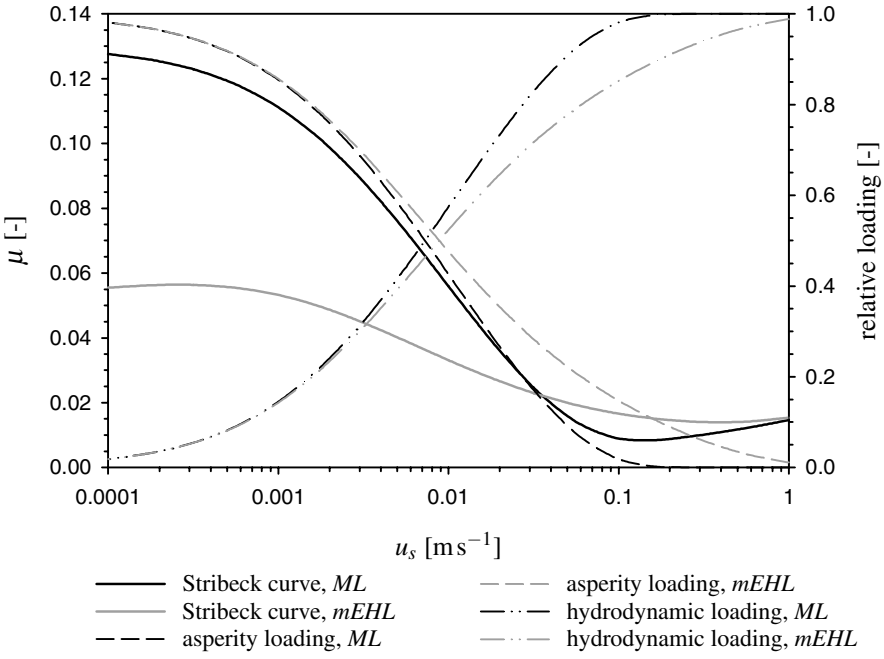

Figure 6.4: Stribeck curves according to the *ML* model and according to the *mEHL* model.

the *ML* curve and the *mEHL* curve. When approaching the mixed regime, initially the *mEHL* curve has a higher coefficient of friction. This is because theoretically, in the *mEHL* model a part of the asperities is always "in contact". Since the friction in asperity contacts is higher than in the hydrodynamic part, the overall friction is also a little higher. In the *ML* model asperities are in contact only if the undeformed asperity penetrates the counter surface. This is also shown by the asperity loading curves. Over the complete mixed regime, the *mEHL* model predicts more asperity contact than the *ML* model. This is a result from the small deformations of the asperities from which the undeformed shape

approaches the smooth opposing surface.

Once the asperities start to deform in the *ML* model, this curve also starts to increase. The slope is higher than in the *mEHL* model, since the asperity contact coefficient of friction in the *ML* model is higher than in the *mEHL* model. Where the *ML* curve increases further and gradually approaches its asymptote $\mu = 0.13$, the *mEHL* curve reaches a maximum at about $u_s = 0.0003\ \mathrm{m\,s^{-1}}$. At lower velocities the coefficient of friction decreases. In this velocity range the majority of the force is carried by the asperities and the friction is almost completely determined by the asperity contacts. As a result, in the *mEHL* model the friction will decrease with decreasing velocity, see eq. (6.1).

Far into the mixed regime and in the BL regime, there is not much difference in load sharing between the two models. This indicates that the additional deformation of the asperities is relatively small and that the increase in average film thickness, i.e. h_{sm}, is small too. In Figure 6.5 this is confirmed. The figure shows the hydrodynamic film

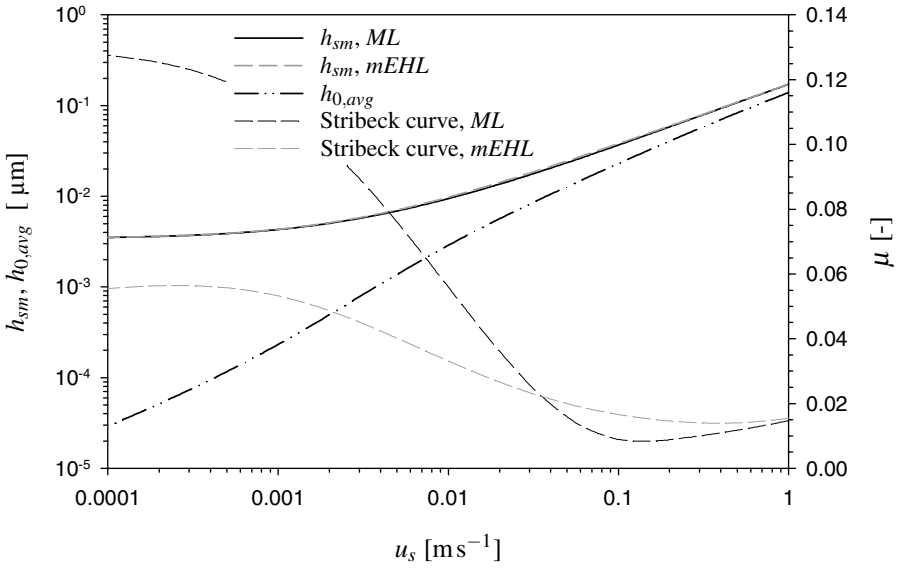

Figure 6.5: Average film thickness in the *ML* and *mEHL* model and the average micro contact film. Stribeck curves are included.

in both models and the average of the films in the micro contacts. The mean films are virtually the same. At thick films almost no asperity deformation takes place so that the difference between h_{sm} and $h_{0,avg}$ is constant and approximately equal to the average of the positive amplitudes. When the surfaces start to touch, the asperities close to the counter surface deform relatively much and the micro contact area of these contacting asperities increases. As a result, the total area of the micro contacts is determined for a large part by these asperities close to the opposing surface, leading to a slightly steeper drop in $h_{0,avg}$ in the ML regime. At very low velocities, the film thickness in the micro contacts is determined by the same principles as the macro contact at full film, i.e. both are in the EHL regime, so that the change in film with velocity is the same.

It is very important to note that in the low velocity region $h_{0,avg}$ decreases to very low values, only fractions of nanometers. It is questionable if under these conditions the asperities are still lubricated by a liquid film.

6.4 Parameter study

To study the influence of the various parameters in the micro-EHL model a parameter study is performed. Two micro-geometry parameters, β_s and A, and three lubricant parameters, τ_0, α_0, and η_0 will be discussed.

It is quite difficult to create a new surface which has the right properties in order to obtain the desired variation in β_s or A. To avoid this problem, the list of asperities of the surface from the previous section is used as a reference. Variations in β_s or A are applied directly to the data in the list. Extreme changes can result into a representation of a surface which has a limited practical meaning.

Radius of curvature

Figure 6.6 shows the influence of β. It can be seen that for the *ML* model a larger β gives

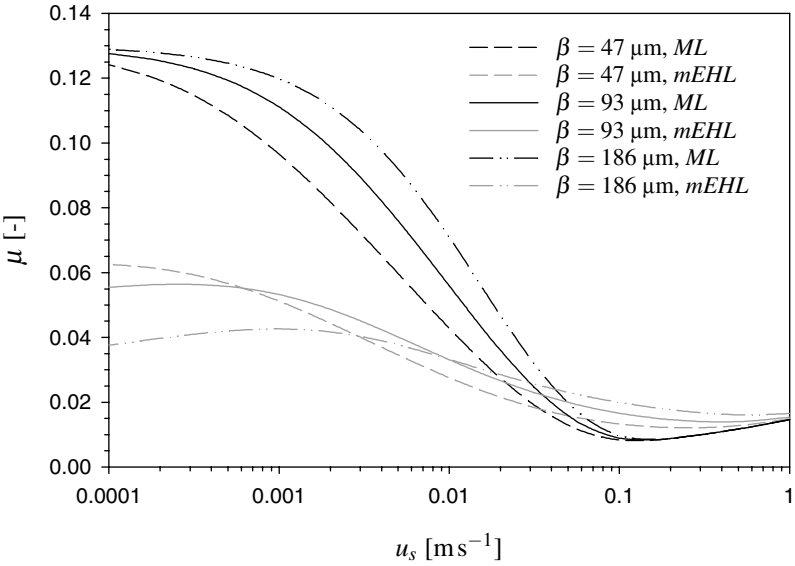

Figure 6.6: Influence of β on the Stribeck curve.

higher friction levels. Combination of eq. (3.84), eq. (3.85) and eq. (6.2) leads to:

$$a_s = \sqrt{h_H \beta_s}, \quad p_H = \frac{E'}{\pi}\sqrt{\frac{h_H}{\beta_s}}, \quad F = \frac{2E'}{3}\sqrt{h_H^3 \beta_s} \tag{6.12}$$

If β increases, slightly less asperity deformation is needed for the same loading, so that BL regime is reached at thicker hydrodynamic films.

For the *mEHL* model a larger β means lower friction. From eq. (6.11) it follows that for the same loading the pressure in the micro contacts is reducing, which results into an exponentially decrease in viscosity. At the same time, a larger β_s leads to a higher h_0. Both effects give rise to a lower shear stress in the micro contacts. However, due to the non-Newtonian behaviour the decrease will be less extreme than the decrease in viscosity is suggesting.

Amplitude

The result of a change in amplitude is shown in Figure 6.7. The *ML* method clearly

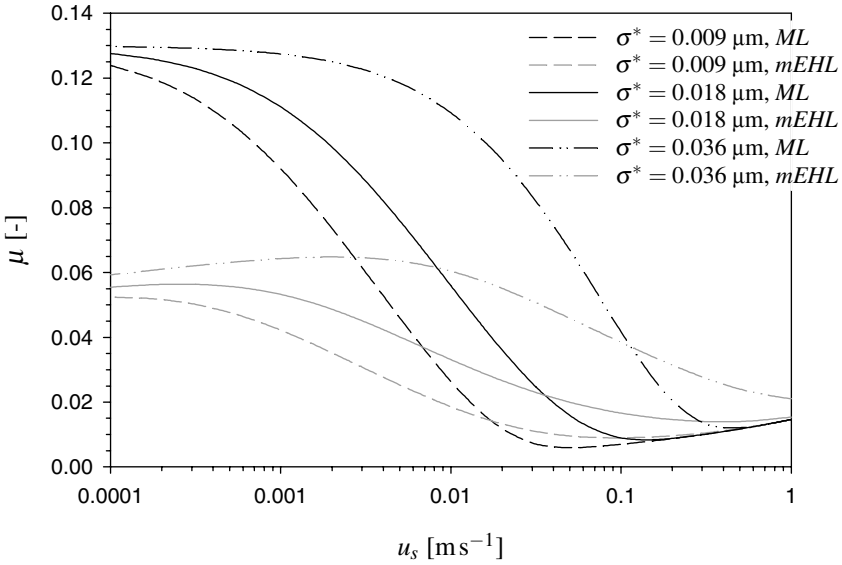

Figure 6.7: Influence of σ^* on the Stribeck curve.

shows the well-known shift to the right with increasing roughness. The same phenomena play a role in the *mEHL* model. Further, the friction level at full asperity contact does not seem to be influenced much by the amplitude. At larger amplitudes more asperity deformation is needed and less asperities are in contact. However, since the loading capacity is proportional to $h_H^{3/2}$ and the micro contact pressure increases only with $\sqrt{h_H}$, the average pressure in the micro contacts will not increase much. At the same time h_0 does not change significantly with a change in amplitude. Both effects result into only a minor change in the shear stress.

Eyring stress

Changing τ_0 leads to the results shown in Figure 6.8. The full film regime is not in-

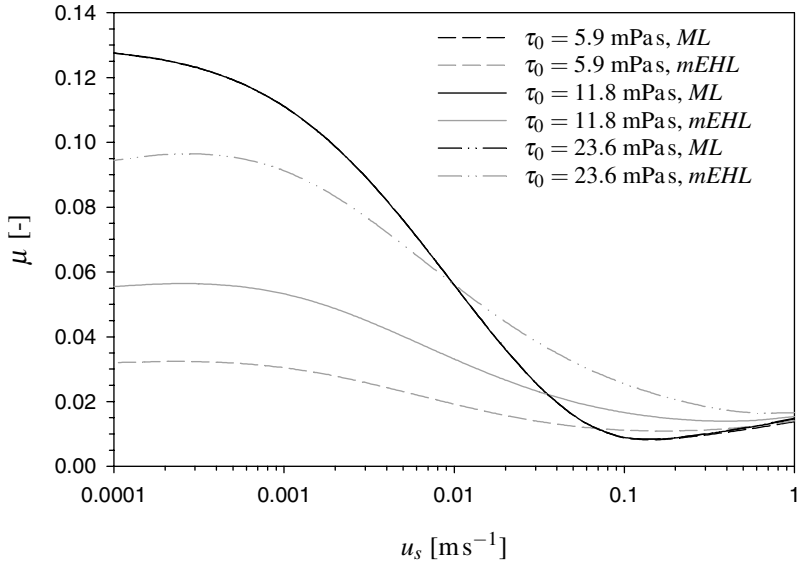

Figure 6.8: Influence of τ_0 on the Stribeck curve.

fluenced by a change in Eyring stress. This is because the macroscopic conditions are such that the lubricant behaves as a Newtonian fluid. The micro contacts enter the non-Newtonian region more easily. However, only the shear stress is affected, the results of the calculation of the asperity deformation and film thickness are exactly the same for each τ_0.

In general, it can be said that an increase in τ_0 leads to an increase in friction. In the low velocity region, where all the force is carried by the asperities, the increase in friction does not differ much from a linear increase with τ_0. This can be explained using eq. (6.1). With $p_{m,avg} \approx 0.93$ GPa and $h_{0,avg} = 2.9 \cdot 10^{-5}$ µm for $u_s = 0.0001$ m s^{-1} and $\tau_0 = 11.8$ MPa, the term $(\eta u_s)/(\tau_0 h_0)$ reads 45. Since $\operatorname{arcsinh} x \approx \ln 2x$ for $x \gg 1$, a twice as high τ_0 will lead to only a 15% decrease in the arcsinh-term. Therefore, the increase in friction is largely determined by the τ_0 before the arcsinh-term.

Pressure viscosity index

A change in α_0 leads to the results as illustrated in Figure 6.9. The figure shows a large influence of α_0 on the hydrodynamic friction. In order to keep the differences between the curves limited, the pressure viscosity index is changed with a factor of $\sqrt{2}$ instead of 2.

Actually α_0 affects the Stribeck curve in two ways. First, it influences the film thickness, both h_{sm} and h_0. Secondly, it changes the shear stresses through the viscosity. In the *ML* model, the influence on the friction level in the hydrodynamic part is evident, a higher α_0 leads to a large increase in friction. The conditions are such that the lubricant is still close to or in the Newtonian region, so that a change in α_0 leads to a close to ex-

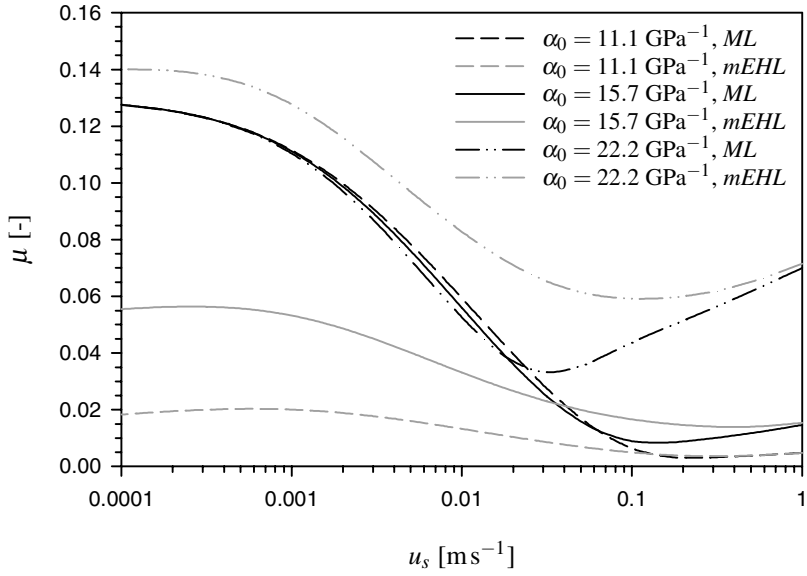

Figure 6.9: Influence of α_0 on the Stribeck curve.

ponential change in friction. The influence on h_{sm} can be seen in the central ML regime, where the asperity friction becomes more important. A higher α_0 gives a thicker film and consequently less asperity contact. Hence the friction will be lower. Although the effect is only minor, it is clearly visible.

For the *mEHL* model the pressure viscosity index affects the whole Stribeck curve. The parameter doubles from the lowest to the highest value, whereas the friction level in the "BL regime" increases roughly with a factor of 7.

Inlet viscosity

Figure 6.10 shows the results of a variation in η_0. For the *ML* model it is observed that the Stribeck curve shifts to the left with increasing inlet viscosity. Due to the increased film formation, the BL regime is reached at lower velocities. The friction level at full film does not seem to be affected much. The increased film thickness and the elevated viscosity are compensating each other for a large part. A detailed observation shows a small increase in friction with increasing η_0. Since the lubricant behaves in a Newtonian way, the shear stress is proportional to $(\eta u_s)/h_0$. The film thickness is proportional to $\eta_0^{3/4}$ (or $\eta_0^{2/3}$ when approaching the rigid piezoviscous regime, i.e. low load and highly viscous lubricant [86]). This means that a slight increase in friction can be expected with increasing η_0.

In the *mEHL* model a decrease in friction with increasing η_0 is observed. According to the statements in the previous paragraph this is not expected. An increase is thought to occur, although much reduced due to the non-Newtonian effects. The decrease is caused

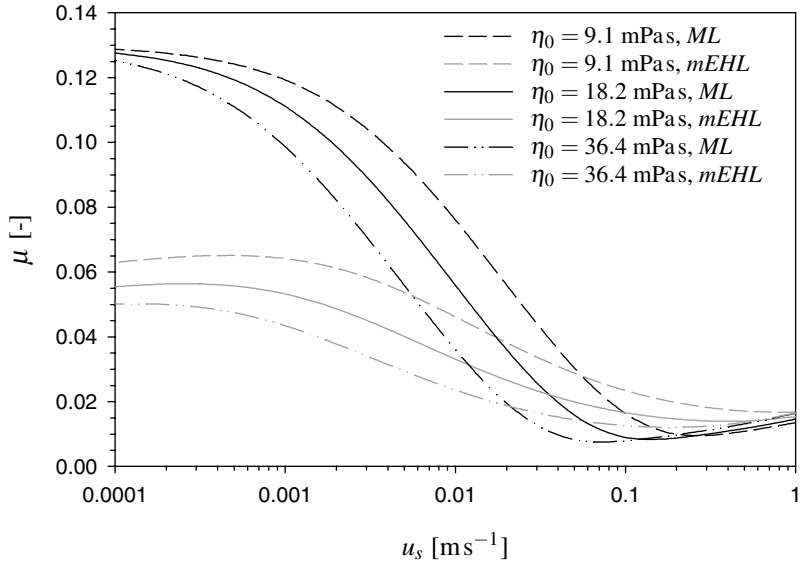

Figure 6.10: Influence of η_0 on the Stribeck curve.

by the nature of the Roelands relation. An increase in η_0 is actually a (small) *decrease* in z according to eq. (3.65). For low pressures, less than p_c, the effect of a change in η_0 or z is the same. For high pressures however, eq. (3.52) can be written as:

$$\eta \approx \eta_0 \exp\left\{\ln\left(\frac{\eta_0}{\eta_\infty}\right)\left(\frac{p}{p_c}\right)^z\right\} \tag{6.13}$$

Here it can be seen that a decrease in z leads to a decrease in viscosity. Combined with an increase in h_0, this results into a lower friction. It also plays a role in the full film regime, particularly if the pressure is in the range of p_c, which is the case. There it reduces the increase in friction.

The characteristics of the Roelands relation should also be taken into account while analyzing the results of changes in α_0. However, since an increase in α_0 gives a same increase in z, here the viscosity is rising even faster than the increase in α_0 is suggesting. As a result, the friction shows an additional increase as well.

6.5 Elastic piezoviscous lubricated micro contacts

Similar to the line contacts situation, a region of validity of the micro EHL contact model should be defined. In section 3.2.3 this is done for the 2D contact problem. To the author's knowledge a similar analysis for point contacts does not exist. However, a fair approximation of the region of validity can be made based on the (partly) analytical asymptotes for the point contact. These asymptotes are given in Nijenbanning et al. [88]

and used to construct the general film thickness formula. The asymptotes read:

$$H_{\mathrm{RI}} = 41.3N^{-2} \tag{6.14}$$

$$H_{\mathrm{RP}} = 0.90L^{2/3} \tag{6.15}$$

$$H_{\mathrm{EI}} = 2^{29/15}3^{-119/60}5^{3/10}\pi^{11/10}N^{-2/15} \tag{6.16}$$

$$H_{\mathrm{EP}} = 2^{7/12}3^{-35/24}\pi^{5/4}N^{-1/12}L^{3/4} \tag{6.17}$$

where RI stands for the rigid isoviscous regime, RP for the rigid piezoviscous regime, EI for the elastic isoviscous regime and EP for the elastic piezoviscous regime. For the present model, the transitions from the RP regime to the EP regime and the transition from the EI regime to the EP regime are of importance on roughness level. Based on eq. (6.15) to eq. (6.17) the boundaries are given by:

$$L < 0.017N \tag{6.18}$$

$$L > 2.4N^{-1/15} \tag{6.19}$$

The check whether a micro contact is in the EP regime or not can be performed by using eq. (6.18) and eq. (6.19). If these equations are not fulfilled, the micro contact does not operate locally in the EP regime. If they are excluded from the calculation of the Stribeck curve, the friction curve as presented in Figure 6.4 changes into the dashed line shown in Figure 6.11. It is observed that in the *mEHL* curve with only EP lubricated

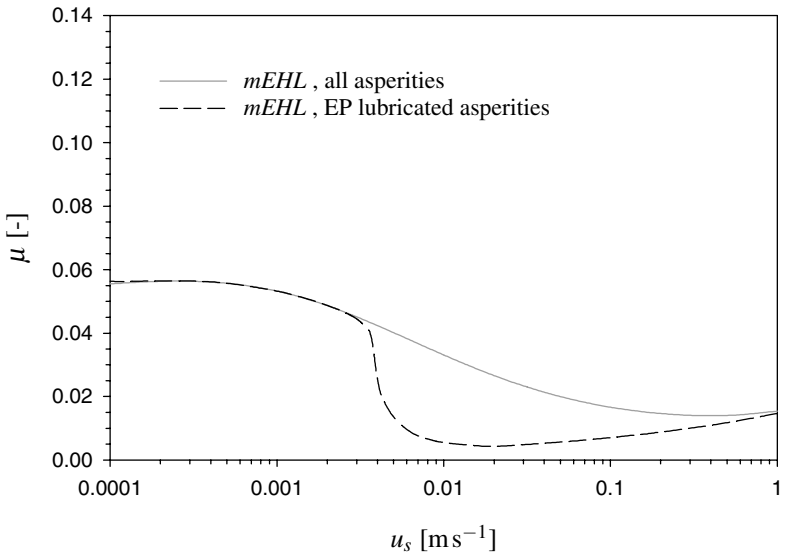

Figure 6.11: Micro-EHL Stribeck curves with all asperities and asperities operating in the elastic piezoviscous regime.

micro contacts, the contribution to friction is reduced to virtually *zero* up to half-way the

ML regime. Then it quickly approaches the *mEHL* curve, indicating that EP lubricated contacts control the friction. The reason for the EP lubricated contact reduction is that, according to the local N and L values, the micro contacts are actually in the RP region. Due to the increased macroscopic hydrodynamic pressure the local inlet viscosity is very high, leading to a lower N and higher L.

At very low velocities part of the contacts changes regime as well. Combination of the low velocities and lower inlet viscosity makes the contacts enter the EI regime.

6.6 Comparison with measurement

Schipper [93] measured Stribeck curves which indicate the occurrence of micro EHL. He measured a low coefficient of friction and at the same time measured no electrical conductivity, indicating a separation of the surfaces in the ML and BL regime. The operating conditions were the same as the conditions given in Table 6.1. One of the surfaces was the one given in Figure 6.1. Unfortunately, the other surface got lost, so no combined roughness could be created. However, the measured curve can still be compared to the predictions. In Figure 6.12 the *mEHL* curve and the measured curve are presented. Although the measured curve is shifted to the right, the changes take place over a reduced

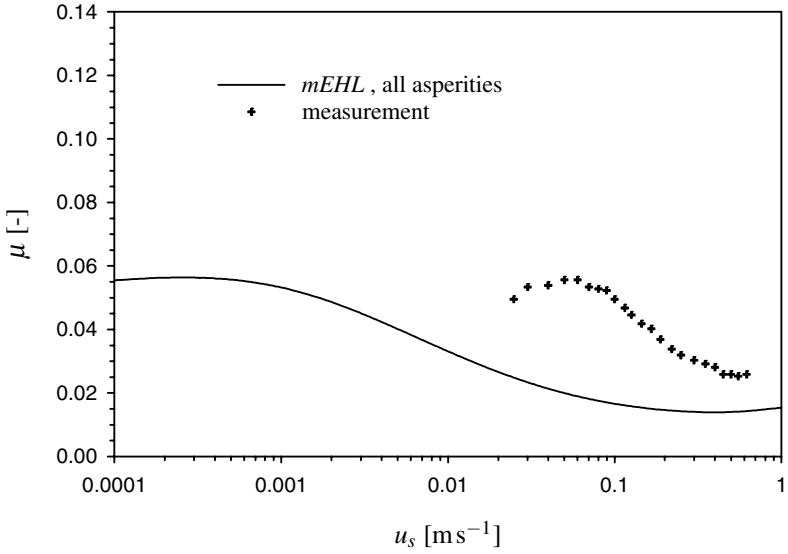

Figure 6.12: Measured and predicted Stribeck curves.

velocity range and the friction level in the full film regime is slightly higher, the general trend is the same as the prediction. Even the decrease at the low velocities is measured. The higher level of friction in the full film regime could be explained by a slightly higher α_0, since there is still some uncertainty in the determination of this parameter. The shift to the right can be explained by an increased combined roughness, indicating that the unknown counter surface was much rougher than the one given in Figure 6.1.

6.7 Summary

If the conditions are such that micro-EHL may occur, generally this will have a large impact on friction. It will reduce considerably. In the full asperity contact regime it even decreases with decreasing velocity, provided that the fluid stays in the liquid state. The occurrence of micro-EHL under certain operational conditions will be limited by the ability to form a lubricant layer at films of sub nanometer level. Whether it is really possible to build a lubricant film at these small gaps or not, is still a question mark.

As stated in chapter 1, an increased lifetime of roller bearings would be realized with decreasing the friction. This can be realized by increasing η_0 or decreasing α_0, τ_0 and σ^*. The effect of the radius of curvature of the asperities on life is not that clear, only to generate micro-EHL an increase in β is beneficial.

The parameter study reveals that the lubricant parameters are relatively important with respect to friction level, in particular α_0. However, it must be noted that some of the effects are caused by the limited possibilities to transform the lubricant parameters properly into the Roelands parameters.

Regarding experimental work involving friction, it is observed that the general trend of the experimental results is predicted well by the present model. Unfortunately, no sufficient information about the contacting surfaces was available to compare theory and experiment in a quantitative way.

Chapter 7

Conclusions and recommendations

In this thesis micro-EHL and its effect on friction is studied. A model is developed to give more insight into the processes which control the occurrence of micro-EHL. Based on the work presented in the previous chapters a number of conclusions can be drawn which will be presented here. The conclusions are followed by recommendations for further work in this field.

7.1 Conclusions

Chapter 1: Introduction

At full asperity contact the friction depends on the state in which the lubricant is functioning. If the lubricant behaves as a solid, the friction is close to the limiting shear stress over pressure coefficient and is independent of the velocity. If it behaves as a liquid the friction can decrease with decreasing velocity. In either case the friction is lower compared to boundary lubricated asperities. Since the asperities are separated by a (small) film, the wear is reduced as well. Both the reduction in friction and wear lead to an increase of the life of the contacting surfaces.

Chapter 2: Background

The film formation under asperity summits under Newtonian conditions and relatively thick films is studied extensively and successfully. The models presented in literature indicate that the film thickness is determined by the inlet pressure sweep. Inside the loaded zone the viscosity is very high, preventing pressure induced flow. The micro geometry is of importance with respect to the pressure peaks (and with that fatigue), the micro-EHL film thickness does not change significantly when passing the contact.

If the conditions become more severe, it is very likely that non-Newtonian effects become more important. This will promote pressure induced flow, reducing the

influence of the inlet pressure sweep. Another effect promoting the increase of pressure flow is the reduction of the hydrodynamic pressure, which is caused by the load transfer of the asperity contacts. As a result, micro-EHL becomes a more local effect; the asperity geometry is going to play a role inside the loaded zone. This initiated the present approach, which considers each asperity as a concentrated contact on micro scale.

Chapter 3: Micro-EHL model

Based on the Ertel assumptions a new model is developed which is able to predict the film thickness under a cylindrical shaped asperity as well as under a spherical shaped asperity, provided that the lubricant behaves in a Newtonian manner. The model also accounts for the limited amount of lubricant available in the macro contact. The equations for the 2D and 3D situation show great resemblance, apart from a constant they are exactly the same. The lubricant parameters are the dominant factors, in which the modulus of elasticity and the amplitude are of minor importance. The second geometry parameter, the radius of curvature, also has a limited influence. The trend agrees with the work available as discussed in chapter 2, which shows that under Newtonian conditions the significance of the local geometry in the loaded zone is limited.

Chapter 4: Asperity characterized by amplitude and slope

Asperities characterized by a slope and an amplitude are studied by means of a wedge shaped (2D) and a conical shaped (3D) asperity. The dependence of the film thickness on the lubricant parameters is only slightly larger than in the case where asperities are given by a radius of curvature and amplitude. The geometry parameters however have a significantly larger influence. For the slope, the behaviour follows ones intuition: a larger slope leads to a smaller film. For the amplitude however, it is the other way around. A larger amplitude leads to a thicker film. In other words: a rougher surface with the same slope as the smoother surface has better lubrication properties.

Chapter 5: Non-Newtonian lubricant behaviour

Non-Newtonian lubricant behaviour is studied under isoviscous conditions for the cylindrical shaped asperity. The main conclusion is that the influence of the lubricant is less pronounced, whereas the importance of the asperity geometry parameters increases. This agrees with the observations made in chapter 2. Unfortunately no analytical approximation of the piezoviscous non-Newtonian lubricant behaviour is found. For more details in this field, a full numerical analysis seems inevitable.

Chapter 6: Stribeck curves

If micro-EHL occurs, the friction decreases substantially. Once all the load is carried by the asperities, the friction decreases with decreasing velocity, provided that the lubricant stays in the liquid regime. The limit of micro-EHL will be the actual lubricating ability of the micro contact at very small predicted films. Numbers in the order of fractions of nanometers are not unusual and it is questionable if it is possible to build up a film under these conditions.

For an increased life of a bearing surface a low friction is favorable. This is realized by increasing η_0 or decreasing α_0, τ_0 and σ^*. As for the radius of curvature, a larger β leads to thicker micro films. Its influence on the friction however, is not that clear. Further, it is shown that the lubricant parameters have a larger influence on friction than the geometry parameters.

The theory and experiments agree in a qualitative way. Lack of experimental data concerning the micro geometry limits the comparison in a quantitative way.

7.2 Recommendations

Several recommendation for further work can be made. The most important ones are listed in this section.

- One of the key subjects will be the experimental verification. A number of experiments must be performed which include a reliable measurement of the micro-geometry. At the same time the selection of asperities and determination of the radius of curvature must be studied. In the present model the asperity interaction at large deformation is neglected. The deformation at full asperity contact however indicates that it can play a role. A dynamic way of asperity determination as presented in the work of Masen [83] and Jamari [69] could improve the present approach.

- Piezoviscous non-Newtonian lubricant behaviour must be included, even if this requires considerable numerical effort. Further, the incorporation of a limiting shear stress approach is desirable. The work of Jacod [67] can be used as a starting point.

- With the present friction model for calculating the micro-EHL Stribeck curve, all contacts are regarded as EP lubricated contacts. The model can be improved by incorporating the rigid piezoviscous lubricated micro contacts. It must be noted that this might introduce some difficulties regarding the determination of the local loading, micro contact area and local friction force.

  The EI lubricated micro contacts can be included in a similar way as in the present model. Since the Hertzian formulas apply, the determination of the local contact area and coefficient of friction is equal to the EP case.

References

[1] **Ai, X. and Cheng, H.S.**, 1996, 'The effects of surface texture on EHL point contacts', *Journal of Tribology* **118**, pp. 59–66.

[2] **Ai, X, Cheng, H.S. and Zheng, L.**, 1993, 'A transient model for microelastohydrodynamic lubrication with three-dimensional irregularities', *Journal of Tribology* **115**, pp. 102–110.

[3] **Ai, X. and Zheng, L.**, 1989, 'A general model for microelastohydrodynamic lubrication and its full numeric solution', *Journal of Tribology* **111**, pp. 569–576.

[4] **Archard, J.F. and Cowking, E.W.**, 1966, 'Elastohydrodynamic lubrication of point contacts', *Proceedings of the Institution of Mechanical Engineers. Part 3B* **180**, pp. 47–56.

[5] **ASME Research Committee on Lubrication**, 1953, 'Pressure-viscosity report, vols. I & II'.

[6] **Bair, S. and Winer, W.O.**, 1979*a*, 'A rheological model for elastohydrodynamic contacts based on primary laboratory data', *Journal of Lubrication Technology* **101**, pp. 258–265.

[7] **Bair, S. and Winer, W.O.**, 1979*b*, 'Shear strength measurements of lubricants at high pressure', *Journal of Lubrication Technology* **101**, pp. 251–257.

[8] **Bair, S. and Winer, W.O.**, 1982*a*, 'Regimes of traction in concentrated contact lubrication', *Journal of Tribology* **104**, pp. 382–391.

[9] **Bair, S. and Winer, W.O.**, 1982*b*, 'Some observations in high pressure rheology of lubricants', *Journal of Tribology* **104**, pp. 357–364.

[10] **Bair, S. and Winer, W.O.**, 1992, 'The high pressure high shear stress rheology of liquid lubricants', *Journal of Tribology* **114**, pp. 1–13.

[11] **Bair, S. and Winer, W.O.**, 1995, Application of the Yasutomi free volume model to various liquid lubricants, *in* 'Proceedings of the International Tribology Conference, Yokohama', ITC, pp. 651–655.

[12] **Bair, S., Winer, W.O. and Qureshi, F.**, 1993, 'Lubricant rheological properties at high pressure', *Lubrication Science* **5**, pp. 189–203.

[13] **Barlow, A.J., Erginsav, A. and Lamb, J.**, 1967, 'Viscoelastic relaxation of supercooled liquids', *Proceedings of the Royal Society of London* **298**, pp. 481–494.

[14] **Barlow, A.J., Harrison, G., Irving, J.B., Kim, M.G., Lamb, J. and Pursley, N.C.**, 1972, 'The effect of pressure on the viscoelastic properties of liquids', *Proceedings of the Royal Society of London* **327**, pp. 403–412.

[15] **Barus, C.**, 1893, 'Isothermals, isopiestics and isometrics relative to viscosity', *American Journal of Science* **45**, pp. 87–96.

[16] **Bayer, R.G. and Ku, T.C.**, 1964, *Handbook of Analytical Design for Wear*, Plenum Press.

[17] **Blok, H.**, 1965, Inverse problems in hydrodynamic lubrication and design directives for lubricated flexible surfaces, *in* D. Muster and B. Sternlicht, eds, 'Proceedings of the International Symposium on Lubrication and Wear', Mc Cutchan Publishing Corp., Berkeley, California, pp. 1–79.

[18] **Chang, L., Cusano, C. and Conry, T.F.**, 1989, 'Effects of lubricant rheology and kinematic conditions on micro-elastohydrodymaic lubrication', *Journal of Tribology* **111**, pp. 344–351.

[19] **Chang, L., Webster, M.N. and Jackson, A.**, 1993, 'On the pressure rippling and roughness deformation in elastohydrodynamic lubrication of rough surfaces', *Journal of Tribology* **115**, pp. 439–444.

[20] **Chevalier, F., Lubrecht, A.A., Cann, P.M.E., Colin, F. and Dalmaz, G.**, 1998, 'Film thickness in starved EHL point contacts', *Journal of Tribology* **120**, pp. 126–133.

[21] **Chittenden, R.J., Dowson, D., Dunn, J.F. and Taylor, C.M.**, 1985, 'A theoretical analysis of the isothermal elastohydrodynamic lubrication of concentrated contacts. II. General case, with lubricant entrainment along either principal axis of the hertzian contact ellipse or at some intermediate angle.', *Proceedings of the Royal Society of London, Series A* **397**, pp. 245–270.

[22] **Choo, J.W., Glovnea, R.P., Olver, A.V. and Spikes, H.A.**, 2003, 'The effects of three-dimensional model surface roughness features on lubricant film thickness in EHL contacts', *Journal of Tribology* **125**, pp. 533–542.

[23] **Christensen, H.**, 1970, 'Stochastic models for hydrodynamic lubrication of rough surfaces', *Proceedings of the Institution of Mechanical Engineers. Part 1* **184**, pp. 1013–1026.

[24] **Christensen, H.**, 1971, 'Some aspects of the functional influence of surface roughness in lubrication', *Wear* **17**, pp. 149–163.

[25] **Christensen, H. and Tønder, K.**, 1971, 'The hydrodynamic lubrication of rough bearing surfaces of finite width', *Journal of Lubrication Technology* **93**, pp. 324–330.

[26] **Christensen, H. and Tønder, K.**, 1973, 'The hydrodynamic lubrication of rough journal bearings', *Journal of Lubrication Technology* pp. 166–172.

[27] **Conry, T.F., Wang, S. and Cusano, C.**, 1987, 'A Reynolds-Eyring equation for elastohydrodynamic lubrication in line contacts', *Journal of Tribology* **109**, pp. 648–658.

[28] **Crook, A.W.**, 1961, 'The lubrication of rollers - II. Film thickness with relation to viscosity and speed', *Philosophical Transactions of the Royal Society of London* **254**, pp. 223–258.

[29] **Dowson, D. and Higginson, G.R.**, 1966, *Elasto-Hydrodynamic Lubrication, The Fundamentals of Roller and Gear Lubrication*, Pergamon Press, Oxford, Great Britain.

[30] **Elcoate, C.D., Evans, H.P., Hughes, T.G. and Snidle, R.W.**, 2001, 'Transient elastohydrodynamic analysis of rough surfaces using a novel coupled differential deflection method', *Proceedings of the Institution of Mechanical Engineers. Part J. Journal of Engineering Tribology* **215**, pp. 319–337.

[31] **Elrod, H.G.**, 1973, 'Thin-film lubrication theory for netonian fluids with surfaces possessing striated roughness or grooving', *Journal of Lubrication Technology* **95**, pp. 484–489.

[32] **Elsharkawy, A.A. and Hamrock, B.J.**, 1991, 'Subsurface stresses in micro-EHL line contacts', *Journal of Tribology* **113**, pp. 645–657.

[33] **Ertel, A.M.**, 1939, 'Hydrodynamic theory of lubrication based on new principles', *Acad. Nauk SSSR, Prikadnaya Mathematica i Mekhanika* **3**(2), pp. 41–52.

[34] **Evans, C.R.**, 1983, The Measurement and Mapping of the Rheological Properties of Elastohydrodynamic Lubricants, PhD thesis, University of Cambridge.

[35] **Evans, C.R. and Johnson, K.L.**, 1986*a*, 'Regimes of traction in elastohydrodynamic lubrication', *Proceedings of the Institution of Mechanical Engineers* **200**, pp. 313–324.

[36] **Evans, C.R. and Johnson, K.L.**, 1986*b*, 'The rheological properties of elastohydrodynamic lubricants', *Proceedings of the Institution of Mechanical Engineers* **200**, pp. 303–312.

[37] **Eyring, H.**, 1936, 'Viscosity, plasticity and diffusion as examples of reaction rates', *Journal of Chemical Physics* **4**, p. 283.

[38] **Faraon, I.C.**, 2005, Mixed Lubricated Line Contacts, PhD thesis, University of Twente.

[39] **Félix-Quiñonez, A., Ehret, P., Summers, J.L. and Morales-Espejel, G.E.**, 2004, 'Fourier analysis of a single transverse ridge passing through an elastohydrodynamically lubricated contact: A comparison with experiment', *Proceedings of*

the Institution of Mechanical Engineers. Part J. Journal of Engineering Tribology **218**, pp. 33–43.

[40] **Fowles, P.E.**, 1969, 'The application of elastohydrodynamic lubrication theory to individual asperity-asperity collisions', *Journal of Lubrication Technology* **91**, pp. 464–476.

[41] **Fowles, P.E.**, 1971*a*, 'Extension of the elastohydrodynamic theory of individual asperity-asperity collisions to the second half of the collision', *Journal of Lubrication Technology* **93**, pp. 213–215.

[42] **Fowles, P.E.**, 1971*b*, 'A thermal elastohydrodynamic theory for individual asperity-asperity collisions', *Journal of Lubrication Technology* **93**, pp. 383–397.

[43] **Fowles, P.E.**, 1975, 'The statistical application of a thermal EHL theory for individual asperity-asperity collisions to the sliding contact of rough surfaces', *Journal of Lubrication Technology* **97**, pp. 311–320.

[44] **Gecim, B. and Winer, W.O.**, 1980, 'Lubricant limiting shear stress effect on EHD film thickness', *Journal of Lubrication Technology* **102**, pp. 213–221.

[45] **Gelinck, E.R.M.**, 1999, Mixed Lubrication of Line Contacts, PhD thesis, University of Twente.

[46] **Glovnea, R.P., Choo, J.W., Olver, A.V. and Spikes, H.A.**, 2003, 'Compression of a single transverse ridge in a circular elastohydrodynamic contact', *Journal of Tribology* **125**, pp. 275–282.

[47] **Greenwood, J.A.**, 1972, 'An extension of the Grubin theory of elastohydrodynamic lubrication', *Journal of Psysics. Section D. Applied physics* **5**, pp. 2195–2211.

[48] **Greenwood, J.A. and Morales-Espejel, G.E.**, 1993, 'The behaviour of transverse roughness in EHL contacts', *Proceedings of the Institution of Mechanical Engineers. Part J. Journal of Engineering Tribology* **208**, pp. 121–132.

[49] **Greenwood, J.A. and Tripp, J.H.**, 1967, 'The elastic contact of rough spheres', *Journal of Applied Mechanics* **34**, pp. 153–159.

[50] **Greenwood, J.A. and Williamson, J.B.P.**, 1966, 'Contact of nominally flat surfaces', *Proceedings of the Royal Society of London* **295**, pp. 300–319.

[51] **Grubin, A.N.**, 1949, Fundamentals of the hydrodynamic theory of lubrication of heavily loaded cylindrical surfaces, *in* Kh.F. Ketova, ed., 'Investigation of the Contact of Machine Components, DSIR Translation, Book Nr. 30', TsNIITMASh, pp. 115–166. Based on [33].

[52] **Guangteng, G., Cann, P.M., Olver, A.V. and Spikes, H.A.**, 2000, 'Lubricant film thickness in rough surface, mixed elastohydrodynamic contact', *Journal of Tribology* **122**, pp. 65–76.

[53] **Guangteng, G., Cann, P.M., Spikes, H.A. and Olver, A.**, 1999, Mapping of surface features in the thin film lubrication regime, *in* 'Proceedings of the 25th Leeds-Lyon Symposium on Tribology', pp. 175–183.

[54] **Hamrock, B.J. and Dowson, D.**, 1977, 'Isothermal EHL of point contacts, part III, fully flooded results', *Journal of Lubrication Technology* **99**, pp. 264–276.

[55] **Hamrock, B.J. and Jacobson, B.O.**, 1984, 'Elastohydrodynamic lubrication of line contacts', *ASLE Transactions* **27**, pp. 275–287.

[56] **Harris, T.A. and Yu, W.K.**, 1999, 'Lundberg-palmgren fatigue theory: Considerations of failure stress and stressed volume.', *Journal of Tribology* **121**, pp. 85–89.

[57] **Hersey, M.D.**, 1914, 'The laws of lubrication of journal bearings', *Transactions of the ASME* **4**, pp. 542–552.

[58] **Hertz, H.**, 1881, 'Über die Berührung fester elastischer Körper', *Journal für die reine und angewandte Mathematik* **92**, pp. 156–171.

[59] **Holmes, M.J.A., Evans, H.P., Hughes, T.G. and Snidle, R.W.**, 2003, 'Transient elastohydrodynamic point contact analysis using a new coupled differential deflection method. part 2: Results.', *Proceedings of the Institution of mechanical Engineers. Part J. Journal of engineering tribology* **217**, pp. 305–321.

[60] **Hooke, C.J.**, 1980, 'The elastohydrodynamic lubrication of heavily loaded point contacts', *Journal of Mechanical Engineering Science* **22**, pp. 183–187.

[61] **Hooke, C.J.**, 1998, 'Surface roughness modification in elastohydrodynamic line contacts operating in the elastic piezoviscous regime', *Proceedings of the Institution of Mechanical Engineers, Part J, Journal of Engineering Tribology* **212**, pp. 145–162.

[62] **Hooke, C.J.**, 2000, 'The behaviour of low-amplitude surface roughness under line contacts: Non-Newtonian fluids', *Proceedings of the Institution of Mechanical Engineers. Part J. Journal of Engineering Tribology* **214**, pp. 253–265.

[63] **Hooke, C.J. and Venner, C.H.**, 2000, 'Surface roughness attenuation in line and point contacts', *Proceedings of the Institution of Mechanical Engineers, Part J, Journal of Engineering Tribology* **214**, pp. 439–444.

[64] **Iivonen, H. and Hamrock, B.J.**, 1991, 'A non-Newtonian fluid model for elastohydrodynamic lubrication of rectangular contacts', *Wear* **143**, pp. 287–305.

[65] **Ioannides, E., Bergling, G. and Gabelli, A.**, 1999, 'An analytical formulation for the life of rolling bearings.', *Acta polytechnica Scandinavica* **137**.

[66] **Jacobson, B.O. and Hamrock, B.J.**, 1984, 'Non-Newtonian fluid model incorporated into elastohydrodynamic lubrication of rectangular contacts', *Journal of Tribology* **106**, pp. 275–284.

[67] **Jacod, B.**, 2002, Friction in Elasto-Hydrodynamic Lubrication, PhD thesis, University of Twente, Enschede, The Netherlands.

[68] **Jacod, B., Lugt, P.M., Dumont, M.L., Tripp, J.H. and Venner, C.H.**, 2000, 'Amplitude reduction of waviness in elastohydrodynamic lubrication using an Eyring fluid model', *Proceedings of the Institution of Mechanical Engineers. Part J. Journal of Engineering Tribology* **214**, pp. 343–350.

[69] **Jamari**, 2006, Running-in of Rolling Contacts, PhD thesis, University of Twente, Enschede, The Netherlands.

[70] **Johnson, K.L.**, 1987, *Contact Mechanics*, Cambridge University Press.

[71] **Johnson, K.L., Greenwood, J.A. and Poon, S.Y.**, 1972, 'A simple theory of asperity contact in elastohydrodynamic lubrication.', *Wear* **19**, pp. 91–108.

[72] **Johnson, K.L. and Tevaarwerk, J.L.**, 1977, 'Shear behaviour of elastohydrodynamic oil films', *Proceedings of the Royal Society of London* **356**, pp. 215–236.

[73] **Kaneta, M. and Cameron, A.**, 1980, 'Effects of asperities in elastohydrodynamic lubrication', *Journal of Lubrication Technology* **102**, pp. 374–379.

[74] **Kaneta, M. and Nishikawa, H.**, 1999, 'Experimental study on microelastohydrodynamic lubrication', *Proceedings of the Institution of Mechanical Engineers. Part J. Journal of Engineering Tribology* **213**, pp. 371–381.

[75] **Kaneta, M., Sakai, T. and Nishikawa, H.**, 1992, 'Optical interferometric observations of the effects of a bump on point contact EHL', *Journal of Tribology* **114**, pp. 779–784.

[76] **Kaneta, M., Sakai, T. and Nishikawa, H.**, 1993, 'Effects of surface roughness on point contact EHL', *Tribology Transactions* **36**, pp. 605–612.

[77] **Koets, O.J.**, 1962, Een overzicht van de elastohydrodynamische smeringstheorie, Master's thesis, University of Twente, Enschede, The Netherlands.

[78] **Lee, R. and Hamrock, B.J.**, 1990, 'A circular non-Newtonian fluid model: Part I - Used in elastohydrodynamic lubrication', *Journal of Tribology* **112**, pp. 486–496.

[79] **Love, A.E.H.**, 1939, 'Boussinesq's problem for a rigid cone', *Quarterly Journal of Mathematics* **10**, p. 161.

[80] **Lubrecht, A.A.**, 1987, The Numerical Solution of the Elastohydrodynamically Lubricated Line and Point Contact Problem, Using Multigrid Techniques, PhD thesis, University of Twente, Enschede, The Netherlands.

[81] **Lubrecht, A.A., Graille, D., Venner, C.H. and Greenwood, J.A.**, 1999, 'Waviness amplitude reduction in EHL line contacts under rolling-sliding', *Journal of Tribology* **120**, pp. 705–710.

[82] **Lundberg, G. and Palmgren, A.**, 1947, 'Dynamic capacity of rolling bearings.', *Acta polytechnica Scandinavica* **3,7**.

[83] **Masen, M.A.**, 2004, Abrasive Tool Wear in Metal Forming Processes, PhD thesis, University of Twente, Enschede, The Netherlands.

[84] **Masen, M.A., Venner, C.H., Lugt, P.M. and Tripp, J.H.**, 2002, 'Effects of surface micro-geometry on the lift-off speed of an EHL-contact', *Tribology Transactions* **45**, pp. 21–30.

[85] **Moes, H.**, 1992, 'Optimum similarity analysis with applications to elastohydrodynamic lubrication', *Wear* **159**, pp. 57–66.

[86] **Moes, H.**, 2000, *Lubrication and Beyond*, University of Twente. Lecture notes, for students only.

[87] **Morales-Espejel, G.E., Venner, C.H. and Greenwood, J.A.**, 2000, 'Kinematics of transverse real roughness in elastohydrodynamically lubricated line contacts using fourier analysis', *Proceedings of the Institution of Mechanical Engineers. Part J Journal of Engineering Tribology* **214**, pp. 523–534.

[88] **Nijenbanning, G., Venner, C.H. and Moes, H.**, 1994, 'Film thickness in elastohydrodynamically lubricated elliptic contacts', *Wear* **176**, pp. 217–229.

[89] **Patir, N. and Cheng, H.S.**, 1978, 'An average flow model for determining effects of three-dimensional roughness on partial hydrodynamic lubrication', *Journal of Lubrication Technology* **100**, pp. 12–17.

[90] **Petrusevich, A.I.**, 1951, 'Fundamental conclusions from the hydrodynamic theory of lubrication', *Izv. Akad. Nauk. SSSR (OTN)* **2**, pp. 209–233.

[91] **Reynolds, O.**, 1886, 'On the theory of lubrication and its application to mr. Beauchamp Tower's experiments, including an experimental determination of the viscosity of olive oil.', *Philosophical Transactions of the Royal Society of London, Part I* **177**, pp. 157–234.

[92] **Roelands, C.J.A.**, 1966, Correlational Aspects of the Viscosity-Temperature-Pressure Relationship of Lubrication Oils, PhD thesis, Technische Hogeschool Delft, The Netherlands.

[93] **Schipper, D.J.**, 1988, Transitions in the Lubrication of Concentrated Contacts, PhD thesis, University of Twente, Enschede, The Netherlands.

[94] **Schipper, D.J., Vroegop, P.H., De Gee, A.W.J. and Bosma, R.**, 1990, 'Micro-EHL in lubricated concentrated contacts', *Journal of Tribology* **112**, pp. 392–397.

[95] **Sloetjes, J.W., Schipper, D.J., Lugt, P.M. and Tripp, J.H.**, 2000, The determination of changes in surface topography using image processing techniques, *in* 'Proceedings of the International Tribology Conference, Nagasaki'.

[96] **Spikes, H.A.**, 2004, Fundamentals of mixed lubrication, *in* 'Tribology and Lubrication Engineering; 14th International Colloquium Tribology, Technische Akademie Esslingen', p. 21.

[97] **Stribeck, R.**, 1902, 'Die wesentlichen Eigenschaften der Gleit- und Rollenlager', *Zeitschrift des Vereines Deutscher Ingenieure* **46**, pp. 1341–1348, 1432–1438, 1463–1470.

[98] **Tabor, D.**, 1982, The role of surface and intermolecular forces in thin film lubrication, *in* 'Microscopic Aspects of Adhesion and Lubrication', p. 651.

[99] **Ten Napel, W.E.**, 1998, *Elastohydrodynamische Smering*, University of Twente. Lecture notes, code 115536.

[100] **Tzeng, S.T. and Saibel, E.**, 1967, 'Surface roughness effects on slider bearing lubrication', *ASLE Transactions* **10**, pp. 334–338.

[101] **Venner, C.H.**, 1991, Multilevel Solutions of the EHL Line and Point Contact Problems, PhD thesis, University of Twente, Enschede, The Netherlands.

[102] **Venner, C.H., Couhier, F., Lubrecht, A.A. and Greenwood, J.A.**, 1997, Amplitude reduction of waviness in transient EHL line contacts, *in* 'Elastohydrodynamics '96, Proceedings of the 23rd Leeds-Lyon Symposium on Tribology', pp. 103–112.

[103] **Venner, C.H., Kaneta, M. and Lubrecht, A.A.**, 2000, Surface roughness in elastohydrodynamically lubricated contacts, *in* 'Proceedings of the 26th Leeds-Lyon Symposium on Tribology, 1999', pp. 25–36.

[104] **Venner, C.H., Kaneta, M., Nishikawa, H. and Jacod, B.**, 2000, Effects of waviness on the film thickness in a circular EHL contact under rolling/sliding, *in* 'Proceedings of the International Tribology Conference, Nagasaki', pp. 631–636.

[105] **Venner, C.H. and Lubrecht, A.A.**, 1994*a*, 'Numerical simulation of a transverse ridge in a circular EHL contact under rolling/sliding', *Journal of Tribology* **116**, pp. 751–761.

[106] **Venner, C.H. and Lubrecht, A.A.**, 1994*b*, 'Transient analysis of surface features in an EHL line contact in the case of sliding', *Journal of Tribology* **116**, pp. 186–193.

[107] **Venner, C.H. and Lubrecht, A.A.**, 1999, Amplitude reduction of non-isotropic harmonic patterns in circular EHL contacts, under pure rolling, *in* 'Proceedings of the 25th Leeds-Lyon Symposium on Tribology', pp. 151–162.

[108] **Venner, C.H. and Morales-Espejel, G.E.**, 1999, 'Amplitude reduction of small-amplitude waviness in transient elastihydrodynamically lubricated line contacts', *Proceedings of the Institution of Mechanical Engineers. Part J Journal of Engineering Tribology* **213**, pp. 487–504.

[109] **Wedeven, L.D. and Cusano, C.**, 1979, 'Elastohydrodynamic film thickness measurements of artificially produced surface dents and grooves', *ASLE Transactions* **22**, pp. 369–381.

[110] **Weibull, W.**, 1925, 'Glidlagerteori med variabel viscositet', *Teknisk tidskrift, Mekanik* **55**, pp. 164–167.

[111] **Whitehouse, D.J. and Archard, J.F.**, 1970, 'The properties of random surfaces of significance in their contact', *Proceedings of the Royal Society of London, Series A* **316**, pp. 97–121.

[112] **Wijnant, Y.H.**, 1998, Contact Dynamics in the Field of Elastohydrodynamic Lubrication, PhD thesis, University of Twente, Enschede, The Netherlands.

[113] **Yasutomi, S., Bair, S. and Winer, W.O.**, 1984, 'An application of a free volume model to lubricant rheology 1 - Dependence of viscosity on temperature and pressure', *Journal of Tribology* **106**, pp. 291–303.

Appendix A

Deformation of a wedge shaped asperity

For a cylindrical asperity, the dry contact geometry outside the loaded zone was derived by Hertz [58]. In this appendix an approximation of the gap in case of a wedge shaped asperity will be given.

The undeformed and deformed wedge shape are shown in Figure A.1.

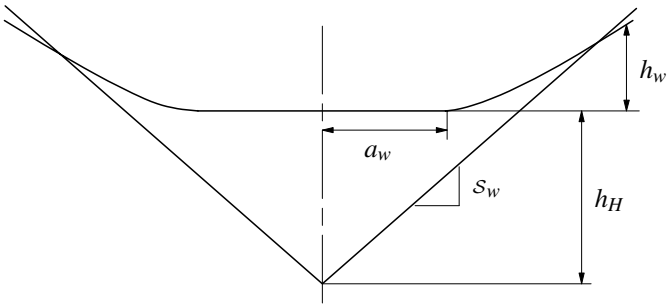

Figure A.1: Deformed and undeformed wedge shaped geometry.

The deformation resulting from a pressure distribution in normal direction reads [70, ch. 2]:

$$v(x) = -\frac{4}{\pi E'} \int_{-a_w}^{a_w} p(s) \ln|x-s| ds + C \tag{A.1}$$

The pressure distribution is given by Johnson [70] and reads [70, ch. 5]:

$$p(x) = \frac{E' s_w}{2\pi} \operatorname{arccosh}\left|\frac{a_w}{x}\right| \tag{A.2}$$

Substitution of eq. (A.2), $x = a_w\bar{x}$ and $s = a_w\bar{s}$ in eq. (A.1) gives:

$$v(x) = -\frac{2s_w a_w}{\pi^2}\int_{-1}^{1} \operatorname{arccosh}\left|\frac{1}{\bar{s}}\right| \ln|\bar{x}-\bar{s}|d\bar{s} + \bar{C} \tag{A.3}$$

Once the deformation is known, the gap geometry outside the loaded zone is determined simply by:

$$h_w(x) = s_w|x| + v(x) \tag{A.4}$$

Unfortunately, no solution for h_w is found yet. However, based on 1) preliminary analysis based on series expansion, 2) extrapolation of the similarity between the gap geometry for the spherical and conical asperity to the cylindrical and wedge shaped asperity and 3) some trial and error, the following gap geometry for the wedge shaped asperity is proposed:

$$h_w(x) = \frac{2s_w}{\pi}\left(|x|\arctan\left(\sqrt{\left(\frac{x}{a_w}\right)^2 - 1}\right) - a_w \ln\left(\left|\frac{x}{a_w}\right| + \sqrt{\left(\frac{x}{a_w}\right)^2 - 1}\right)\right), \quad |x| \geq a_w \tag{A.5}$$

The result is confirmed by numerical analysis. For $s_w = a_w = 1$ the gap geometry given by eq. (A.5) perfectly fits eq. (A.4) with the deformation based on direct numerical integration of eq. (A.3).

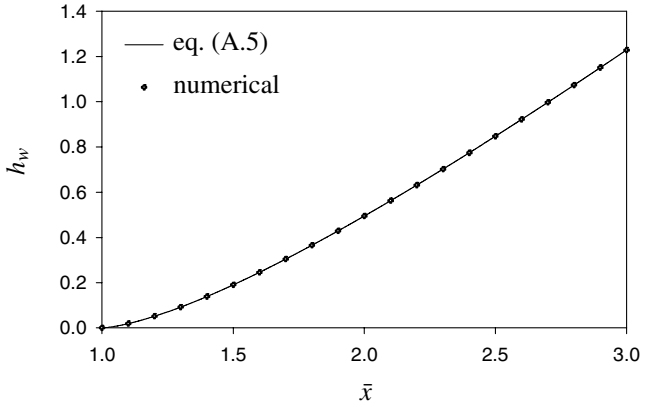

Figure A.2: Gap geometry outside the loaded zone.

Following Crook's [28] method to approximate the gap outside the loaded zone, it seems justified to use the first term from the series expansion of eq. (A.5) for $\sqrt{|x| - a_w} \geq 0$ in the case such an approximation is needed, see for instance section 4.1 is this thesis.

$$h_w(x) \approx \frac{4\sqrt{2}\,s_w}{3\pi\sqrt{a_w}}\left(|x| - a_w\right)^{3/2} = \frac{4\sqrt{2}\,a_w s_w}{3\pi}\left(|\bar{x}| - 1\right)^{3/2} \tag{A.6}$$

Appendix B

Deformation of a conical shaped asperity

For a spherical shaped asperity, the maximum deformation at the summit and the dry contact geometry outside the loaded zone was derived by Hertz [58]. This appendix presents the same for a conical shaped asperity, denoted as h_H and h_n respectively, see Figure B.1. First the deformation inside the loaded zone is determined to obtain the maximum deformation at the summit of the cone. In section B.2 the gap geometry outside the loaded zone is derived. Both derivations are based on the approach as described in Johnson [70, ch. 3].

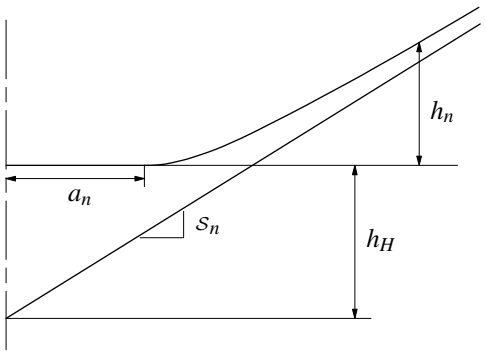

Figure B.1: Deformed and undeformed conical shaped geometry.

B.1 Deformation inside the loaded zone

The deformation at a certain point on a surface due to a concentrated normal force P is given by [70, ch. 3]:

$$v(r) = \frac{1-\nu^2}{\pi E}\frac{\mathsf{P}}{r} \tag{B.1}$$

The deformation resulting from a distributed normal force is obtained by integration, see Figure B.2:

$$v(r) = \frac{1-\nu^2}{\pi E}\iint_{\Omega}\frac{p(t,\theta)}{|r-t|}dt\,t\,d\theta \tag{B.2}$$

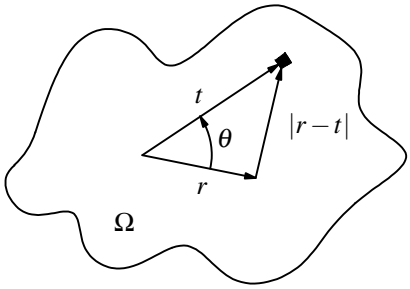

Figure B.2: Deformation resulting from distributed pressure.

In a contact, in which the pressure acts on both surfaces, the total deformation is the sum of deformation of the individual surfaces:

$$v(r) = \frac{2}{\pi E'}\iint_{\Omega}\frac{p(t,\theta)}{|r-t|}dt\,t\,d\theta \tag{B.3}$$

In terms of the present configuration, see Figure B.3, this can be written as:

$$v(r) = \frac{2}{\pi E'}\int_0^{\pi}\int_{s_{mn}}^{s_{mx}} p(s,\phi)\,ds\,s\,d\phi \tag{B.4}$$

where:

$$s_{mx} = \sqrt{a_n^2 - r^2\sin^2\phi} - r\cos\phi \tag{B.5}$$

$$s_{mn} = -\sqrt{a_n^2 - r^2\sin^2\phi} - r\cos\phi \tag{B.6}$$

For a conical asperity the pressure distribution is given by Love [79] and reads [70, ch. 5]:

$$p(r) = \frac{E' s_n}{4}\operatorname{arccosh}\left|\frac{a_n}{r}\right| = \frac{E' s_n}{4}\operatorname{arctanh}\left(\sqrt{1-\left(\frac{r}{a_n}\right)^2}\right) \tag{B.7}$$

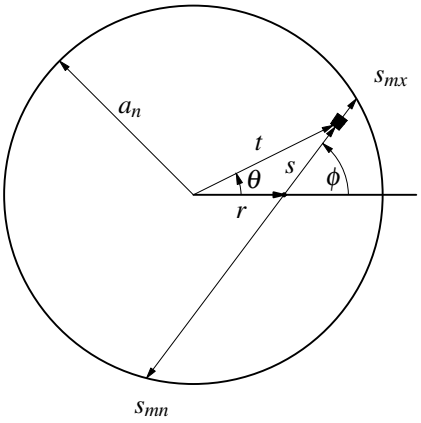

Figure B.3: Calculation of deformation in the loaded zone. Reproduced from [70].

With eq. (B.7), $r = a_n\bar{r} =$ and $s = a_n\bar{s}$, eq. (B.4) to eq. (B.6) become:

$$v(r) = \frac{a_n \mathcal{S}_n}{2\pi} \int_0^{\pi} \int_{\bar{s}_{mn}}^{\bar{s}_{mx}} \operatorname{arctanh}\left(\sqrt{1-(\bar{s}^2+\bar{r}^2+2\bar{r}\bar{s}\cos\phi)}\right) d\bar{s}d\phi \tag{B.8}$$

where:

$$\bar{s}_{mx} = \sqrt{1-\bar{r}^2\sin^2\phi} - \bar{r}\cos\phi \tag{B.9}$$

$$\bar{s}_{mn} = -\sqrt{1-\bar{r}^2\sin^2\phi} - \bar{r}\cos\phi \tag{B.10}$$

The next step is the first integration:

$$\begin{aligned}\int_{\bar{s}_{mn}}^{\bar{s}_{mx}} \operatorname{arctanh}\left(\sqrt{1-(\bar{s}^2+\bar{r}^2+2\bar{r}\bar{s}\cos\phi)}\right) d\bar{s} = \\ \Bigg[\frac{1}{2}(\bar{r}\mathcal{G}+\bar{r}\cos\phi)\operatorname{arctanh}\left(\frac{\bar{r}\bar{s}\mathcal{G}+\bar{r}^2\mathcal{G}\cos\phi+1+\bar{r}^2\mathcal{G}^2}{\mathcal{K}}\right) \\ + \frac{1}{2}(\bar{r}\mathcal{G}-\bar{r}\cos\phi)\operatorname{arctanh}\left(\frac{\bar{r}\bar{s}\mathcal{G}+\bar{r}^2\mathcal{G}\cos\phi-1-\bar{r}^2\mathcal{G}^2}{\mathcal{K}}\right) \\ + \bar{s}\operatorname{arctanh}(\mathcal{K}) + \arctan\left(\frac{\bar{s}+\bar{r}\cos\phi}{\mathcal{K}}\right) \Bigg]_{\bar{s}_{mn}}^{\bar{s}_{mx}} = \pi(1-\bar{r}|\sin\phi|)\end{aligned} \tag{B.11}$$

where:

$$\mathcal{G} = \sqrt{\cos^2\phi - 1} \tag{B.12}$$

$$\mathcal{K} = \sqrt{1-(\bar{s}^2+\bar{r}^2+2\bar{r}\bar{s}\cos\phi)} \tag{B.13}$$

Integrating once more gives:

$$\int_0^{\pi} \pi\,(1-\bar{r}|\sin\phi|)\,d\phi = \pi^2 - 2\pi\bar{r} \tag{B.14}$$

Substitution of this result in eq. (B.8) yields for the deformation:

$$v(r) = s_n\left(\frac{\pi a_n}{2} - r\right) \tag{B.15}$$

As expected, the deformation is a linear function following the shape of the undeformed cone. Maximum deformation is reached at the summit:

$$h_H = \frac{\pi}{2} s_n a_n \tag{B.16}$$

B.2 Deformation outside the loaded zone

The derivation of the deformation outside the loaded zone is based on the same approach. The equivalent of eq. (B.8) reads (see also Figure B.4):

$$v(r) = \frac{a_n s_n}{2\pi}\int_{\phi_{mn}}^{\phi_{mx}}\int_{\bar{s}_{mn}}^{\bar{s}_{mx}} \operatorname{arctanh}\left(\sqrt{1-(\bar{s}^2+\bar{r}^2-2\bar{r}\bar{s}\cos\phi)}\right) d\bar{s}\,d\phi \tag{B.17}$$

where:

$$\bar{s}_{mx} = \sqrt{1-\bar{r}^2\sin^2\phi} + \bar{r}\cos\phi \tag{B.18}$$

$$\bar{s}_{mn} = -\sqrt{1-\bar{r}^2\sin^2\phi} + \bar{r}\cos\phi \tag{B.19}$$

$$\phi_{mx} = \arcsin\left(\frac{1}{\bar{r}}\right) \tag{B.20}$$

$$\phi_{mn} = -\arcsin\left(\frac{1}{\bar{r}}\right) \tag{B.21}$$

The first integration gives:

$$\begin{aligned}
&\int_{\bar{s}_{mn}}^{\bar{s}_{mx}} \operatorname{arctanh}\left(\sqrt{1-(\bar{s}^2+\bar{r}^2-2\bar{r}\bar{s}\cos\phi)}\right) d\bar{s} = \\
&\quad\Bigg[-\frac{1}{2}(\bar{r}\mathcal{G}+\bar{r}\cos\phi)\operatorname{arctanh}\left(\frac{-\bar{r}\bar{s}\mathcal{G}+\bar{r}^2\mathcal{G}\cos\phi+1+\bar{r}^2\mathcal{G}^2}{\mathcal{K}}\right) \\
&\qquad + \frac{1}{2}(\bar{r}\mathcal{G}-\bar{r}\cos\phi)\operatorname{arctanh}\left(\frac{\bar{r}\bar{s}\mathcal{G}-\bar{r}^2\mathcal{G}\cos\phi+1+\bar{r}^2\mathcal{G}^2}{\mathcal{K}}\right) \\
&\qquad + \bar{s}\operatorname{arctanh}(\mathcal{K}) - \arctan\left(\frac{-\bar{s}+\bar{r}\cos\phi}{\mathcal{K}}\right)\Bigg]_{\bar{s}_{mn}}^{\bar{s}_{mx}} = \pi\,(1-\bar{r}|\sin\phi|)
\end{aligned} \tag{B.22}$$

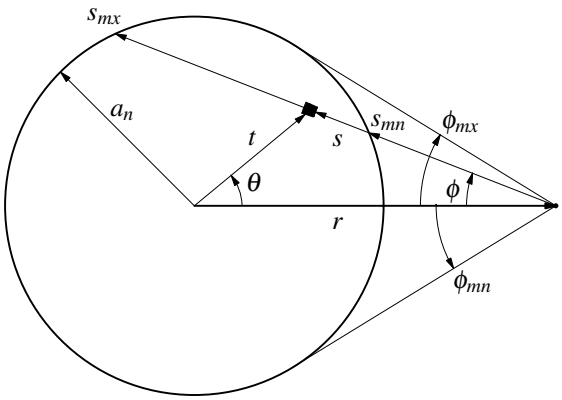

Figure B.4: Calculation of deformation outside the loaded zone. Reproduced from [70].

where:

$$\mathcal{G} = \sqrt{\cos^2\phi - 1} \tag{B.23}$$

$$\mathcal{K} = \sqrt{1 - (\bar{s}^2 + \bar{r}^2 - 2\bar{r}\bar{s}\cos\phi)} \tag{B.24}$$

The second integration results into:

$$\int_{\phi_{mn}}^{\phi_{mx}} \pi\,(1 - \bar{r}|\sin\phi|)\,d\phi = 2\pi\left(\arcsin\left(\frac{1}{\bar{r}}\right) + \sqrt{\bar{r}^2 - 1} - \bar{r}\right) \tag{B.25}$$

Substitution in eq. (B.17) yields for the deformation outside the loaded zone:

$$v(r) = \mathcal{S}_n\left(a_n \arcsin\left(\frac{a_n}{r}\right) + \sqrt{r^2 - a_n^2} - r\right) \tag{B.26}$$

Addition of the deformation to the undeformed geometry, i.e. $\mathcal{S}_n r$, gives the gap geometry (see also eq. (A.4)):

$$h_n(r) = \mathcal{S}_n\left(a_n \arcsin\left(\frac{a_n}{r}\right) + \sqrt{r^2 - a_n^2} - \frac{a_n\pi}{2}\right), \quad r \geq a_n \tag{B.27}$$

Note that the term $-a_n\pi/2$ is added to ensure $h_n(a_n) = 0$. Eq. (B.27) can also be written as:

$$h_n(r) = \mathcal{S}_n\left(\sqrt{r^2 - a_n^2} - a_n \arctan\left(\sqrt{\left(\frac{r}{a_n}\right)^2 - 1}\right)\right), \quad r \geq a_n \tag{B.28}$$

which shows large similarities with the gap geometry for a spherical asperity, see eq. (3.98).

Often Crook's [28] approach is used to approximate the gap geometry. For the conical case this comes down to:

$$h_n(r) \approx \frac{2\sqrt{2}\,\mathcal{S}_n}{3\sqrt{a_n}}(r - a_n)^{3/2} = \frac{2\sqrt{2}\,a_n\mathcal{S}_n}{3}(\bar{r} - 1)^{3/2} \tag{B.29}$$

Appendix C

Modulus of Ξ_3

The equations (5.29) through (5.31) are given:

$$\Xi_1 = \left(5\bar{h}^2S^2 - 20(\bar{h}-\bar{h}_0)^2\right)S^2\Theta^4 + \left(36\bar{h}^2(\bar{h}-\bar{h}_0)^2 + 10\bar{h}^4S^2\right)\Theta^2 + 5\bar{h}^6 \tag{C.1}$$

$$\Xi_2 = 29S^2\Theta^2 - 8\bar{h}^2 \tag{C.2}$$

$$\Xi_3 = \frac{27\sqrt{30}}{\sqrt{7}}\bar{h}^2\Theta^2(\bar{h}-\bar{h}_0)^2(S^2\Theta^2+\bar{h}^2)\frac{\sqrt{\Xi_2}}{{\Xi_1}^{3/2}} \tag{C.3}$$

From Ξ_2 follows that a real value for Ξ_3 is obtained if $\bar{h} < \sqrt{29/8}\,S\Theta$. For larger $\bar{h}$ it becomes imaginary. The aim is to verify if in such cases its modulus is smaller than *one*. For this purpose the upper limit, i.e. $\bar{h}_0 = 0$, is examined. Substitution of $\bar{h}_0 = 0$ gives:

$$\Xi_3 = \mathrm{I}\frac{27\sqrt{30}}{\sqrt{7}}\frac{\bar{h}^4\Theta^2(S^2\Theta^2+\bar{h}^2)\sqrt{8\bar{h}^2-29S^2\Theta^2}}{\left((5S^2-20)\bar{h}^2S^2\Theta^4 + (36+10S^2)\bar{h}^4\Theta^2 + 5\bar{h}^6\right)^{3/2}} \tag{C.4}$$

With I the imaginary unit and $\bar{h} = \Theta\tilde{h}$, this can be simplified further to:

$$\Xi_3 = \mathrm{I}\frac{27\sqrt{30}}{\sqrt{7}}\frac{\tilde{h}(S^2+\tilde{h}^2)\sqrt{8\tilde{h}^2-29S^2}}{\left((5S^2-20)S^2 + (36+10S^2)\tilde{h}^2 + 5\tilde{h}^4\right)^{3/2}} \tag{C.5}$$

The derivative with respect to $\tilde{h}$ reads:

$$\frac{d\Xi_3}{d\tilde{h}} = -\mathrm{I}\frac{27\sqrt{30}}{\sqrt{7}}$$
$$\frac{80\tilde{h}^8 - (355S^2+288)\tilde{h}^6 - (805S^2-928)S^2\tilde{h}^4 - (225S^2+3508)S^4\tilde{h}^2 + (145S^2-580)S^6}{\left((5S^2-20)S^2 + (36+10S^2)\tilde{h}^2 + 5\tilde{h}^4\right)^{5/2}\sqrt{8\tilde{h}^2-29S^2}} \tag{C.6}$$

Solving this equation can be done analytically, however the solutions are quite complicated. For $S = 2$ the term $145S^2-580$ vanishes, thereby simplifying the solution proce-

dure to solving a cubic equation. It turns out that there is only one valid solution which reads:

$$\frac{\sqrt{(q^2+427q+319849)}}{2\sqrt{15q}} \text{ with } q = \left(261148843 + 120\sqrt{2463686355189}\right)^{1/3} \approx 766 \tag{C.7}$$

Substitution of this solution in the second order derivative leads to a negative value, which implies that the extreme point must be a maximum of eq. (C.5). Substitution of eq. (C.7) in eq. (C.5) gives for the modulus of Ξ_3:

$$\|\Xi_3\| < 0.21 \text{ for } \bar{h} > \sqrt{\frac{29}{2}}\Theta, \; S = 2 \tag{C.8}$$

Appendix D

Maximum pressure flow induced shear stress component

For the determination of $\mathcal{P}|_{\max}$, the pressure derivative given by eq. (5.28) is substituted in $\mathcal{P}$ as defined in eq. (5.20). Simultaneously $S = 2$ and $\bar{h} = \Theta\tilde{h}$ are substituted. With eq. (5.21) this results into:

$$\mathcal{P} = 6\left(\frac{\sqrt{35}}{9\sqrt{6}\tilde{h}^2}\frac{\sqrt{\Xi_1}}{\sqrt{\Xi_2}}\sinh\left(\frac{1}{3}\operatorname{arcsinh}\Xi_3\right)\right)^{1/2} \tag{D.1}$$

where:

$$\Xi_1 = 80\tilde{h}_0(2\tilde{h} - \tilde{h}_0) + \tilde{h}^2(19\tilde{h}^2 - 18\tilde{h}\tilde{h}_0 + 9\tilde{h}_0^2) + 5\tilde{h}^6 \tag{D.2}$$

$$\Xi_2 = 116 - 8\tilde{h}^2 \tag{D.3}$$

$$\Xi_3 = \frac{27\sqrt{30}}{\sqrt{7}}\tilde{h}^2(\tilde{h} - \tilde{h}_0)^2(4 + \tilde{h}^2)\frac{\sqrt{\Xi_2}}{{\Xi_1}^{3/2}} \tag{D.4}$$

From Figure 5.5 it can be observed that the region of interest is $\tilde{h}_0 < 10^{-3}$. Graphical inspection of $\mathcal{P}$ for $\tilde{h}_0 = 10^{-3}$ and $\tilde{h}_0 = 10^{-10}$ shows that the maximum is located at $\tilde{h} \gg \tilde{h}_0$, see Figure D.1. Consequently, eq. (D.1) through eq. (D.4) can be reduced to:

$$\mathcal{P} = 6\left(\frac{\sqrt{35}}{9\sqrt{6}\tilde{h}^2}\frac{\sqrt{\Xi_1}}{\sqrt{\Xi_2}}\sinh\left(\frac{1}{3}\operatorname{arcsinh}\Xi_3\right)\right)^{1/2} \tag{D.5}$$

where:

$$\Xi_1 = 160\tilde{h}_0\tilde{h} \tag{D.6}$$

$$\Xi_2 = 116 \tag{D.7}$$

$$\Xi_3 = \frac{108\sqrt{30}}{\sqrt{7}}\tilde{h}^4\frac{\sqrt{\Xi_2}}{{\Xi_1}^{3/2}} \tag{D.8}$$

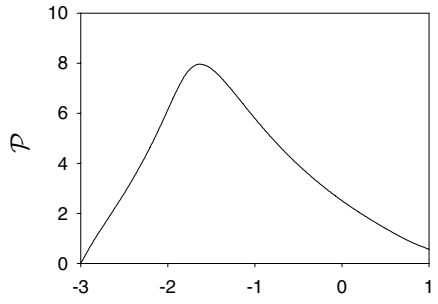

(a) $\tilde{h}_0 = 10^{-3}$

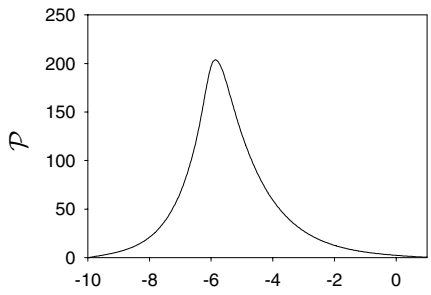

(b) $\tilde{h}_0 = 10^{-10}$

Figure D.1: $\mathcal{P}$ as a function of $\tilde{h}$ for (a) $\tilde{h}_0 = 10^{-3}$ and (b) $\tilde{h}_0 = 10^{-10}$.

This can also be written as:

$$\mathcal{P} = \frac{2^{3/2}5^{1/2}7^{1/4}}{87^{1/4}} \frac{\tilde{h}_0^{1/4}}{\tilde{h}^{3/4}} \sqrt{\sinh\left(\frac{1}{3}\operatorname{arcsinh}\left(\frac{27\sqrt{87}}{80\sqrt{7}} \frac{\tilde{h}^{5/2}}{\tilde{h}_0^{3/2}}\right)\right)} \tag{D.9}$$

The derivative with respect to $\tilde{h}$ reads:

$$\frac{d\mathcal{P}}{d\tilde{h}} = \frac{3^{3/4}7^{1/4}5^{1/2}}{2^{1/2}29^{1/4}} \frac{\tilde{h}_0^{1/4}\cosh\Xi_4}{\tilde{h}^{7/4}\Xi_5\sqrt{\sinh\Xi_4}} (1 - \Xi_5\tanh\Xi_4) \tag{D.10}$$

with

$$\Xi_4 = \frac{1}{3}\operatorname{arcsinh}\left(\frac{27\sqrt{87}}{80\sqrt{7}} \frac{\tilde{h}^{5/2}}{\tilde{h}_0^{3/2}}\right) \tag{D.11}$$

$$\Xi_5 = \sqrt{\frac{1792\tilde{h}_0^3}{783\tilde{h}^5} + \frac{81}{25}} \tag{D.12}$$

The maximum is found from the solution of $1 - \Xi_5\tanh\Xi_4 = 0$. No analytical solution is found. However, inspection of the expression shows that the solution must be of the form $c\tilde{h}_0^{3/5}$. Substitution and numerically solving for c yields:

$$\tilde{h} \approx 1.399257\,\tilde{h}_0^{3/5} \approx \frac{7}{5}\tilde{h}_0^{3/5} \tag{D.13}$$

Substitution in eq. (D.9) leads to:

$$\mathcal{P}|_{\max} \approx 6^{2/5}\tilde{h}_0^{-1/5} \tag{D.14}$$

Graphical representation of eq. (D.10) and eq. (D.13) as shown in Figure D.2 supports the results.

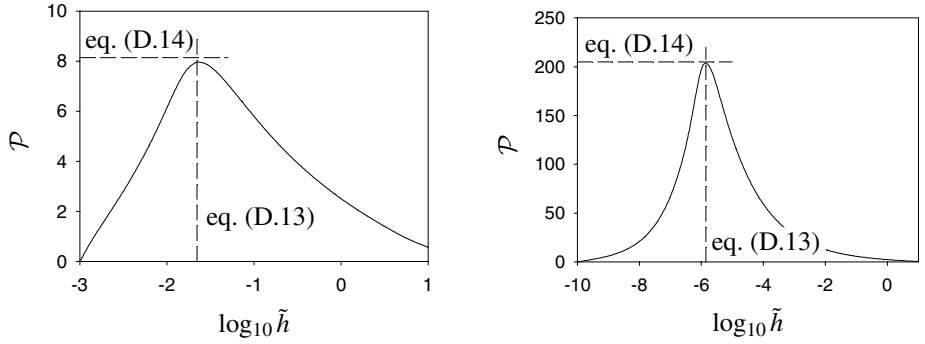

(a) $\tilde{h}_0 = 10^{-3}$ (b) $\tilde{h}_0 = 10^{-10}$

Figure D.2: $\mathcal{P}$ as given by eq. (D.1), the approximation of its maximum and the position of it as a function of $\tilde{h}$ for (a) $\tilde{h}_0 = 10^{-3}$ and (b) $\tilde{h}_0 = 10^{-10}$.

Acknowledgements

Since the beginning of my stay at the University of Twente in September 1991 I have spent more than ten years at the tribology group. First as a master student, later as a Ph.D. student. This very enjoyable time has now come to an end with finishing this thesis. Obviously, the work is not done by one person, many people made a contribution in one way or the other. Therefore I would like to thank them.

The research was sponsored by SKF Engineering & Research Centre, which is gratefully acknowledged.

In particular I wish to thank my mentor and promotor prof.dr.ir. Dik Schipper for his guidance and support during the work. When I tended to see things a little too black and white he got me back on track by showing me the gray side of the matter.

As I have been at the tribology group for quite some time I have seen many colleagues come and go. I would like to thank all of them for their cooperation, support and for creating a pleasant atmosphere. Special thanks go out to my roommates over the past years, Rob Cuperus, Marc Masen and Gerrit van der Linde.

Part of my work was performed at SKF Engineering & Research Centre. I would like to thank everyone for their interest and suggestions.

Above all I would like to thank Froukje for her love, care and encouragement. Without her, finishing this thesis would have been a much harder task. Finally, I wish to thank Tom. His smile helped me to put things into the right perspective.

Jan-Willem Sloetjes
Zwolle, November 2006

Publications

Sloetjes, J.W., Schipper, D.J., Lugt, P.M. and Tripp, J.H., 2000, The determination of changes in surface topography using image processing techniques, *in* 'Proceedings of the International Tribology Conference, Nagasaki'.

Pasaribu, H.R., Sloetjes, J.W. and Schipper, D.J., 2003, 'Friction reduction by adding copper oxide into alumina and zirconia ceramics.', *Wear* **255**, pp. 699–707.

Pasaribu, H.R., Sloetjes, J.W. and Schipper, D.J., 2004, 'The transition of mild to severe wear of ceramics.', *Wear* **256**, pp. 585–591.

Winnubst, A.J.A., Ran, S, Wiratha, K.W., Blank, D.H.A., Pasaribu, H.R., Sloetjes, J.W. and Schipper, D.J., 2004, 'A wear-resistant zirconia ceramic for low friction application.', *Key Engineering Materials* **264-268**, pp. 809–812.

Sloetjes, J.W., Tasan, Y.C., De Rooij, M.B. and Schipper, D.J., 2007, 'Algorithm for determining 3d changes in micro-geometry using image processing techniques.', *Submitted to Tribology Transactions.*